

# Synthesis of RE<sup>3+</sup> (RE<sup>3+</sup> = Ce<sup>3+</sup>, Dy<sup>3+</sup>, Eu<sup>3+</sup> and Tb<sup>3+</sup>) activated Gd<sub>2</sub>SiO<sub>5</sub> optoelectronics materials for lighting

V.V. Shinde <sup>a</sup>, Ashish Tiwari <sup>b</sup>, S.J. Dhoble <sup>a,\*</sup>

<sup>a</sup> Department of Physics, R.T.M. Nagpur University, Nagpur, 440033, India

<sup>b</sup> Department of Chemistry, Dr. Bhimrao Ambedkar Govt. College, Pamgarh, Janjgir-Champa, 495554, India

## ARTICLE INFO

### Article history:

Received 9 June 2019

Received in revised form

3 March 2020

Accepted 5 May 2020

Available online 10 May 2020

### Keywords:

Oxyorthosilicate

Photoluminescence

FT-IR

SSL

CIE

## ABSTRACT

RE<sup>3+</sup>(RE<sup>3+</sup> = Ce<sup>3+</sup>, Dy<sup>3+</sup>, Eu<sup>3+</sup> and Tb<sup>3+</sup>) doped Gd<sub>2</sub>SiO<sub>5</sub> optoelectronic materials were synthesised by solid state diffusion method and their down conversion spectral properties were reported in this paper as function of different RE<sup>3+</sup> concentrations. The solid state diffusion results in well crystallized phosphor particles. The prepared materials were characterized by XRD, FT-IR, photoluminescence (PL) and CIE color co-ordinates techniques. Spectroscopic investigation revealed that gadolinium oxyorthosilicate (GSO), Gd<sub>2</sub>SiO<sub>5</sub> phosphor doped with Ce<sup>3+</sup> shows broad band emission with peak at 390 nm and 440 nm when excited at 350 nm excitation. Gd<sub>2</sub>SiO<sub>5</sub>:Dy<sup>3+</sup> shows efficient blue and yellow band emissions at 481 nm and 576 nm Gd<sub>2</sub>SiO<sub>5</sub>:Eu<sup>3+</sup> phosphor shows an orange and red emission at 587 nm and 615 nm respectively. Whereas Gd<sub>2</sub>SiO<sub>5</sub>:Tb<sup>3+</sup> phosphor shows weak blue emission at 487 nm and strong green 545 nm. The excitation spectra used for the Gd<sub>2</sub>SiO<sub>5</sub>:RE<sup>3+</sup> (where RE<sup>3+</sup> = Ce<sup>3+</sup>, Dy<sup>3+</sup>, Eu<sup>3+</sup> and Tb<sup>3+</sup>) phosphor are in the near UV (nUV) region extending from 250 to 400 nm, which is characteristics of modern lighting and display fields applications. The effect of the RE<sup>3+</sup> (RE<sup>3+</sup> = Ce<sup>3+</sup>, Dy<sup>3+</sup>, Eu<sup>3+</sup> and Tb<sup>3+</sup>) concentration on the luminescence properties of Gd<sub>2</sub>SiO<sub>5</sub>:RE<sup>3+</sup> optoelectronics materials were also studied. The investigated prepared Gd<sub>2</sub>SiO<sub>5</sub> phosphors may be suitable for lighting based devices.

© 2020 Elsevier B.V. All rights reserved.

## 1. Introduction

Luminescent phosphors for technological applications have been widely used in lighting and displays. Global demand for phosphor materials as efficient sources of energy is an ever growing industry and therefore the development of effective luminescent materials is the subject of extensive research in the recent years. In particular, interest has been focused on inorganic luminescent materials, which have potential applications in almost all devices such as fluorescent lamps [1–3], cathode ray tubes [4,5] and X-ray detectors [6,7] etc.

A variety of oxides are known to have good luminescent properties when doped with rare-earth ions. Silica nanoparticles are good candidate materials for the host matrix in the rare-earth oxides, because SiO<sub>2</sub> is cost effective as well as transparent in the visible region and has almost no appreciable effect of its own on the photoluminescence (PL) intensity. The gadolinium oxyorthosilicate crystals (GSO) doped with rare earth ions are attractive materials

for spectroscopic measurements and many applications due to wide energy range of transparency, especially in nUV region. The rare earth ions can be conveniently incorporated into crystal lattice structure at gadolinium local sites since the differences of ionic radii are relatively low. On account of structural properties of Gd<sub>2</sub>SiO<sub>5</sub> crystal, the lanthanide ions may occupy the two distinct sites with C<sub>s</sub> and C<sub>3v</sub> point symmetry respectively. The former is coordinated by seven oxygen ions and in the latter higher point symmetry site is coordinated to the nine oxygen ions. Owing to the physicochemical and luminescence characteristics, GSO materials doped with RE<sup>3+</sup> ions are promising and very attractive candidate especially for nUV LED lighting and display field applications.

The luminescence properties of Gd<sup>3+</sup> compounds have been of considerable interest in recent years. This interest is based on the occurrence of a number of energy transfer (ET) processes which yield high luminescence efficiencies. Also these compounds can be used as efficient phosphors in a new generation of fluorescent lamps. Gd<sup>3+</sup> ion is isoelectronic with Eu<sup>2+</sup> ion, but its 4f→5d state lies at much higher energy, as a consequence, the luminescence of Gd<sup>3+</sup> ion consist of sharp lines 6 P→8 S transitions, mainly at 313 nm. Due to its high energetic position, this emission can only be

\* Corresponding author.

E-mail address: [sjdhoble@rediffmail.com](mailto:sjdhoble@rediffmail.com) (S.J. Dhoble).

observed in lattices with optical absorption at high energy.

Scintillators are materials, which emit light when exposed to ionizing radiation (X-rays,  $\gamma$ -rays etc.). A lot of attention has been paid during last two decades to Ce doped orthosilicate crystals in order to find their potential as scintillating materials. They are frequently used as radiation detectors in various medical imaging medicine (such as x-ray radiography, X-ray mammography computed tomography, gamma camera etc.). They are employed in powder, ceramic or single-crystal form, often coupled to optical photon detectors such as (photocathodes and photodiodes). Out of the various scintillators employed in medical imaging modalities, particular interest is being paid on gadolinium oxyorthosilicate ( $Gd_2SiO_5$  or GSO) often doped with cerium ( $Ce^{3+}$ ) ion activator. In single crystal form, GSO:Ce was firstly produced in 1983 by Takagi and Fukazawa [8]. Number of papers have been devoted to explain the scintillation mechanism and to assess the efficiency of scintillation in GSO:Ce [9]. Rare earth oxyorthosilicates ( $RE_2SiO_5$ ) doped with  $Eu^{3+}$  and  $Tb^{3+}$ , are well-known luminescent materials due to their cathodoluminescence, storage phosphor, scintillator and laser properties [10].

Research on down conversion phosphor materials is the key for

as sodium carbonate ( $Na_2CO_3$ ) are used to increase the powder reactivity reaction rate, matrix formation and activator incorporation. These flux materials, which have melting point below the temperature of phosphor formation and dissolving partially one or both of the reactants, take no part in the solid-state reaction and undergo no reaction with the final product [14]. All the chemicals used during the synthesis were of analytical grade (A.R.). Sodium carbonate ( $Na_2CO_3$ ) used was 30–50 wt % of the total weight of the as prepared phosphor. The dopants were ammonium hexanitratocerate ( $(NH_4)_2Ce(NO_3)_6$ ), dysprosium oxide ( $Dy_2O_3$ ), europium oxide ( $Eu_2O_3$ ) and terbium oxide ( $Tb_2O_3$ ) for Ce, Dy, Eu and Tb, respectively. The doping concentrations of four rare earth ions were varied from 0.2 to 10 mol%. The starting materials with dopants in stoichiometric ratio were thoroughly mixed using agate mortar and preheated at  $100^\circ C$  then fired at  $1150^\circ C$  for 6 h in a muffle furnace. When the furnace was cooled down to room temperature the samples were taken out and washed with distilled water 6 times and finally with a mild hydrochloric acid. The washed powder was subsequently dried and crushed to fine powder using agate mortar. The variation in the concentration of the RE dopants is indicated in Table 1.

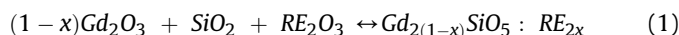
Dopant ion	$Ce^{3+}$	$Dy^{3+}$	$Tb^{3+}$	$Eu^{3+}$
Dopant Concentration	0.5–5 mol%	0.2–10 mol%	0.5–10 mol%	0.5–10 mol %

the development of solid-state lighting (SSL). The purpose of this work was to investigate the performance of gadolinium oxyorthosilicate (GSO),  $Gd_2SiO_5:RE^{3+}$  ( $RE^{3+} = Ce^{3+}, Dy^{3+}, Eu^{3+}$  and  $Tb^{3+}$ ) as an optoelectronic materials with improved photoluminescence properties for lighting applications that can be excited in the ultraviolet region. GSO can be an attractive LED phosphor due to its wide band gap. Moreover, the ground state and excited state of these RE doped ions lie within the band gap of GSO lattice. It also has high density, high effective atomic number, large light output and fast decay. The luminescence efficiency of GSO has been reported to be higher than that of other phosphors. Moreover it has low Stokes shift as compared to other phosphors due to the crystal structural differences [11,12]. The intense absorption at 300–500 nm indicates that the phosphor could be effectively excited by *n*-UV chips [13].

## 2. Experimental

Solid state method was used for synthesising gadolinium oxyorthosilicate phosphors (GSO)  $Gd_2SiO_5:RE^{3+}$  ( $RE^{3+} = Ce^{3+}, Dy^{3+}, Eu^{3+}$  and  $Tb^{3+}$ ) phosphor at high temperature. The starting materials are gadolinium oxide ( $Gd_2O_3$ ), silicon dioxide powder ( $SiO_2$ ) and flux sodium carbonate ( $Na_2CO_3$ ). Different flux materials such

The formation of  $Gd_2SiO_5$  phosphor particle follows the chemical formula:



(Where  $RE_2O_3 = Dy_2O_3, Eu_2O_3$  and  $Tb_2O_3$ . For Ce,  $(NH_4)_2Ce(NO_3)_6$  was used.)

The phase purity and structure of the final products of the gadolinium oxyorthosilicate phosphors  $Gd_2SiO_5$  was examined by x-ray powder diffraction using  $Cu K\alpha$  radiation on a BRUKER – analytical x-ray diffractometer. Infrared spectrum of the pure  $Gd_2SiO_5$  was recorded using a Bruker Fourier transform infrared spectrometer. The morphology of the as prepared phosphor was observed by a Geol-6380 A scanning electron microscope (SEM). For the measurement of spectroscopic properties, the excitation and emission spectra for all samples were recorded on Shimadzu RF-5301PC spectrophotofluorometer using solid sample holder. Emission and excitation spectra were obtained using a spectral slit width of 1.5 nm at room temperature. The co-ordinations in the xy-chromaticity diagram were directly calculated from the fluorescent spectra (CIE 1931). All measurements were made at room temperature.

**Table 1**  
CIE Co-ordinates of  $Gd_2SiO_5: RE^{3+}$  phosphor (Where  $RE^{3+} = Ce^{3+}, Dy^{3+}, Eu^{3+}$  and  $Tb^{3+}$ ).

PHOSPHOR	EXCITATION (nm)	STRONG EMISSION (nm)	(X,Y) COORDINATE	COLOR REGION
$Gd_2SiO_5: Ce^{3+}$	340	440	(0.164, 0.010)	Blue
$Gd_2SiO_5: Dy^{3+}$	275	481	(0.087, 0.144)	Blue
$Gd_2SiO_5: Eu^{3+}$	275	576	(0.485, 0.513)	Yellow
		587	(0.557, 0.442)	Orange
		615	(0.680, 0.319)	Red
$Gd_2SiO_5: Tb^{3+}$	275	487	(0.059, 0.235)	Blue
		545	(0.265, 0.724)	Green

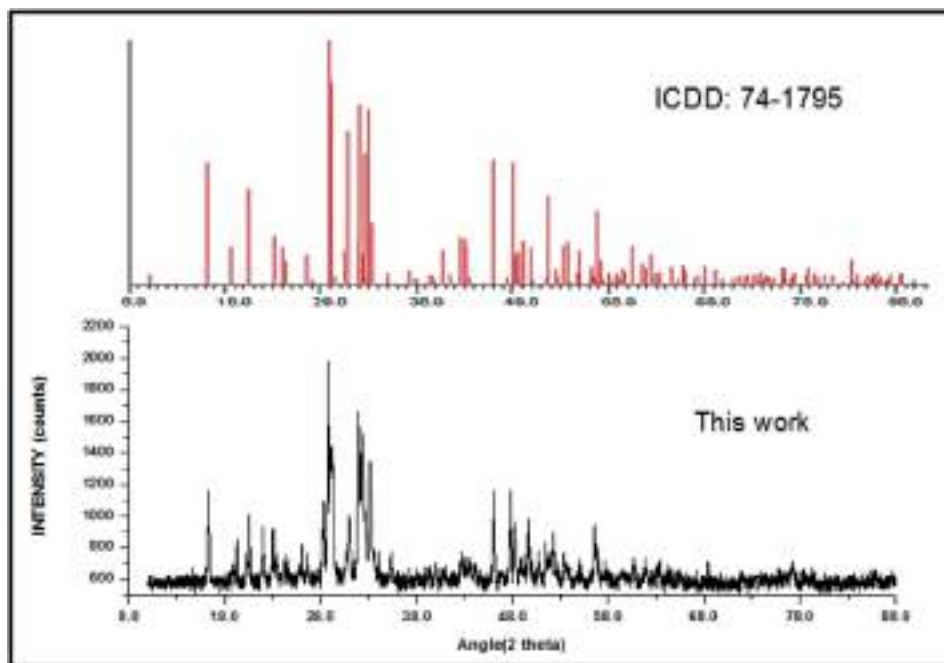


Fig. 1. XRD pattern of pure  $Gd_2SiO_5$ .

### 3. Results and discussion

#### 3.1. X-ray diffraction

The comprehensive analysis of phase verification, structural parameters and crystalline structure of  $Gd_2SiO_5$  phosphor was carried out by powder X-ray diffraction using diffractometer with  $CuK\alpha$  radiation ( $1.505 \text{ \AA}$ ) at operating voltage 40 kV, 30 mA and in the range  $2\theta$  of  $10\text{--}90^\circ$ , prepared by solid state diffusion method at room temperature. The XRD pattern of the synthesised phosphor material  $Gd_2SiO_5$  is as shown in Fig. 1. It was found that acquired diffraction peaks of the phosphor prepared at  $1150^\circ\text{C}$  are in well agreement with the standard ICDD Database file no.74–1795. The sample was visually ensured and found to be physically stable (non-hygroscopic) and milky white in appearance. The obtained pattern reveals that  $Gd_2SiO_5$  powder was formed with no contaminated phases, and implies the complete formation of the homogeneous phosphor material. Reasonably all the diffraction peaks can be indexed to the high crystallinity and high purity of  $Gd_2SiO_5$ . The XRD pattern did not indicate the existence of the constituents and

other likely phases which are direct authentication of the formation of the phosphor.

#### 3.2. Surface morphology

Fig. 2 shows a typical SEM micrograph of as synthesised oxy-orthosilicate  $Gd_2SiO_5$  phosphors. Morphology of powders was characterized by SEM. It is clearly seen that the sizes of the phosphor particles are not uniform, which may be due to agglomeration amongst the particles during the period of sample sintering. It is also known that the morphologies and the shapes of phosphor particles depend on the status of the starting materials, the reaction temperature, and the preparation process. Crystallization granules and agglomeration of particles are observed in the present phosphors. They are formed of agglomerated particles of a granule-like morphology and a size in the range  $1\text{--}5 \mu\text{m}$  long. It exhibited foamy agglomerated particles with homogeneous distribution and presence of random distribution of voids in their structure.

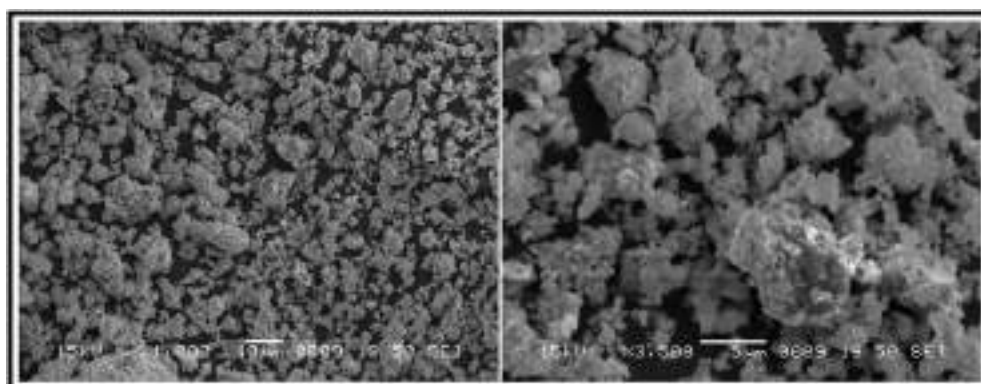


Fig. 2. SEM micrograph of synthesised  $Gd_2SiO_5$ .

### 3.3. Crystal structure

Crystal structure of  $Gd_2SiO_5$  is shown in Fig. 3. It demonstrates that symmetry of the GSO crystal still maintains the primitive monoclinic structure with space group of  $P_{21/c}$ . In GSO host lattice, there are two non-equivalent crystallographic sites of  $Gd^{3+}$  [15], labelled as  $C_5$  symmetry site ( $Gd_1$ ) and  $C_{3V}$  symmetry site ( $Gd_2$ ), which are coordinated with 7 and 9 oxygen atoms, respectively. The  $Gd_1$  coordinated with 7 oxygen is linked with three isolated oxygen ions and three  $[SiO_4^-]$  ions. The  $Gd_2$  coordinated with 9 oxygen is bonded with one isolated oxygen and six tetrahedral  $[SiO_4^-]$  ions. It has been shown that  $Ce^{3+}$ ,  $Eu^{3+}$ ,  $Er^{3+}$ ,  $Yb^{3+}$  and  $Dy^{3+}$  can substitute both  $Gd_1$  and  $Gd_2$  sites in the GSO crystal lattice [16] and hence the detailed investigations of RE doped GSO can provide fundamental processes of excitation and relaxation of excited states and to evaluate the potential of the GSO:RE system for application as a phosphor or laser active material.

The ionic radius of four dopants are listed in Table 2 and it can be seen that except  $Ce^{3+}$  the other three dopants are comparable in size to Gd ion and hence can be effectively doped and occupy the  $Gd_1$  and  $Gd_2$  sites in GSO lattice.

### 3.4. FT-IR analysis

Infrared spectroscopy exploits the fact that molecules have specific rotational and vibrational frequencies corresponding to discrete energy levels. FT-IR spectra shown in Fig. 4 were recorded in the range of  $500\text{--}4000\text{ cm}^{-1}$  to show the functional groups for pure  $Gd_2SiO_5$  sample. FTIR spectrum of the synthesised gadolinium oxyorthosilicate phosphors (GSO)  $Gd_2SiO_5$  obtained after heat treatment at  $11,00\text{ }^\circ\text{C}$  for 6 h shows absorption regions in the range  $500\text{--}1200\text{ cm}^{-1}$ . Inorganic silicates have a characteristic, strong band centred around  $1100\text{ cm}^{-1}$  that in some cases appear as multiple bands [17]. In our case, the bands noticed at  $1118, 998, 929$  and  $888\text{ cm}^{-1}$  was assigned to asymmetric stretching vibration modes of the Si–O–Si bonds, suggesting the formation of well-crystallized silicate. New absorption peaks at  $629$  and  $616\text{ cm}^{-1}$  is due to bonding vibrations of Si–O bonds. It is noticed that after heating the absorption peaks from –OH, and  $H_2O$  disappear completely as shown by the absence of peak in the  $3400\text{--}3600\text{ cm}^{-1}$  region. The FTIR spectrum of this phosphor emphasizes the beginning of the silicate host lattice formation due to the fact that the broadband between  $800$  and  $1200\text{ cm}^{-1}$  becomes more structured. The FTIR spectrum having new peaks other than those

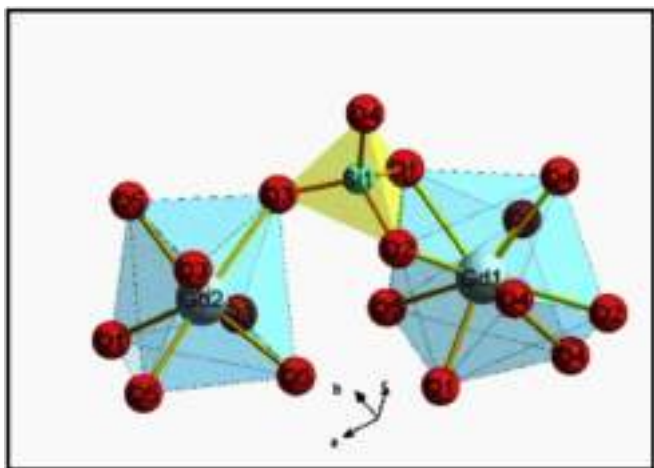


Fig. 3. Crystal structure of  $Gd_2SiO_5$ .

**Table 2**

The ionic radius of the RE dopants.

cation	$Gd^{3+}$	$Ce^{3+}$	$Dy^{3+}$	$Tb^{3+}$	$Eu^{3+}$
radius	94 pm	103 pm	91 pm	92 pm	95 pm

assigned above clearly indicates the presence of RE–O vibration. In the spectrum the absorption band of silicate groups are clearly evident [18–20].

The primitive monoclinic structure space group ( $P2_1/c$ ) can be established by the absence of Si–OH stretching frequency in the FTIR spectrum [21].

### 3.5. PL emission of $RE^{3+}$ in $Gd_2SiO_5$ ( $RE^{3+} = Ce^{3+}, Dy^{3+}, Eu^{3+}$ , and $Tb^{3+}$ )

Photoemission spectroscopy is a powerful tool for studying the broad electronic structure of rare-earth-activated optical materials that provides information about the relative energies of all the occupied rare earth and host crystal electronic states. Gd is situated between europium and terbium in the periodic table and does not have the same intense luminescence characteristics as compared to its neighbours. This is ascribed to the fact that it has more stable half-filled f shell making it very difficult to promote an electron to the excited state. It is known that  $Gd^{3+}$  ion has a half filled 4f shell with  $4f^7$  configuration. The ground term,  $^8S_{7/2}$  is located quite deeply far below the excited states. Consequently, the absorption spectrum of  $Gd^{3+}$  lies entirely in the ultraviolet region. Analysis of the intensities in the excitation and emission spectrum of the  $Gd^{3+}$  ion under UV excitation in gadolinium oxyorthosilicate,  $Gd_2SiO_5$ , are presented in this paper [22].

#### 3.5.1. PL emission of $Ce^{3+}$ in $Gd_2SiO_5$

Fig. 5 shows the excitation spectra in the  $300\text{--}400\text{ nm}$  range and the emission spectra in the  $370\text{--}600\text{ nm}$  range for samples  $Gd_{2(1-x)}SiO_5:Ce_{2x}$  (Where  $x = 0.5, 1, 2,$  and  $5\text{ mol } \%$ ) at room temperature. For the excitation spectra the emitted light was detected at  $450\text{ nm}$ . For the emission spectra the samples were excited at  $350\text{ nm}$ . The emission and excitation are explicitly explained by considering the transitions between the configurations of the  $4f^1$  and  $4f^05d^1$  states of  $Ce^{3+}$  [23–25].

The PL emission spectra of  $Ce^{3+}$  ions in  $Gd_2SiO_5$  phosphors displayed a double humped characteristics with a sharp weak peak at  $390\text{ nm}$  (emission of  $Ce^{3+}$  in  $CeO_6$  polyhedra) and a broad strong peak at  $440\text{ nm}$  which are assigned to the  $5d\text{--}4f$  transition of  $Ce^{3+}$  ions [26–28] and other emission peaks are related to  $CeO_7$  polyhedra arising at two crystallographic sites of different Ce–O coordinates [29–31].

The crystal field effects on the configuration levels of the  $4f^05d^1$  induces a strong dependence of the emission and excitation wavelength as a function of the cerium surroundings. It is also noticed that the peak positions of the emission bands for all  $Ce^{3+}$  doped  $Gd_2SiO_5$  have not changed [32].

The effect of activator concentration was examined on the fluorescent properties. With the increase of concentration of the  $Ce^{3+}$  ion, the distance between  $Ce^{3+}$  ions becomes less and this results in the migration of excitation energy among  $Ce^{3+}$  ions leading to quenching of the emission [33]. The highest luminescent intensity is obtained at  $1\text{ mol } \%$  and then declines with the increase in concentration of the  $Ce^{3+}$  activator ions as shown in inset of Fig. 5.

Various models have been proposed to explain the presence or absence of luminescence. Among them, one-dimensional configuration curve has been most widely used. To illustrate how radiative

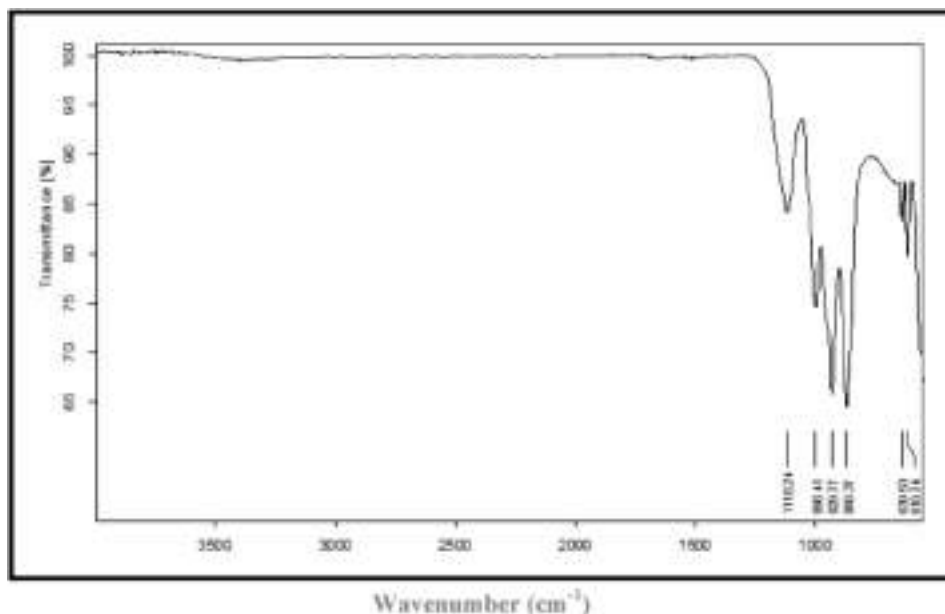


Fig. 4. FT-IR spectrum of synthesised  $Gd_2SiO_5$  phosphor.

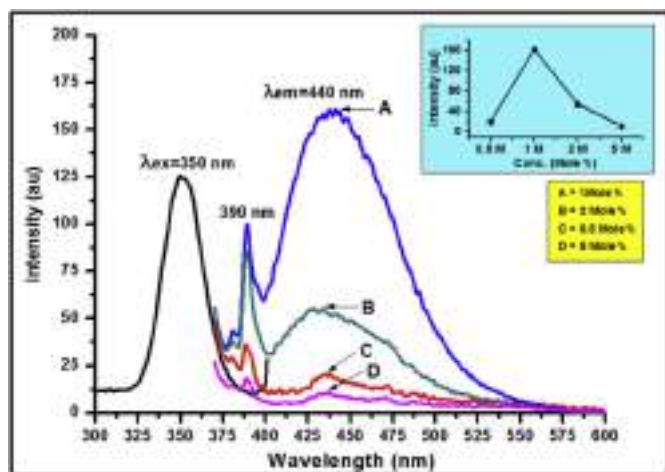


Fig. 5. Concentration dependence of excitation and emission spectra of synthesised  $Gd_2SiO_5:Ce^{3+}$  phosphor.

processes of  $Ce^{3+}$  in  $Gd_2SiO_5$  phosphor works, a partial electronic energy levels and energetic structure along with configuration coordinate diagram are shown in Fig. 6.

The emission from  $Ce^{3+}$  arises from a 5 d state in which the energy levels are highly influenced by the surrounding  $O^{2-}$  ligands. Since not all bonds between the  $Ce^{3+}$  and  $O^{2-}$  ligands are of the same length, the emission from these states becomes distorted towards the longer wavelengths [34].

In configuration co-ordinate diagram, the potential energy of the luminescent centre in the crystal lattice is plotted as functions of the configuration coordinate  $Q$ . The quantity  $Q$  represents the distance between rare earth ion and its surrounding ions. Optical transitions are represented vertically on the configuration coordinate diagrams, because they occur rapidly compared with nuclear motions. As we can see, ground and excited states take form of parabola potential wells. The two lowest parabolas represent the ground electronic configuration  $4f^1$  by spin-orbit interaction into  $^2F_{5/2}$  (the ground state) and  $^2F_{7/2}$  (the first excited state). The lowest

states of excited electronic configuration  $5d^1$  are represented by two higher parabolas. Electron-lattice interaction in the excited electronic manifold causes the shift of the respective parabolas in the configurational space. In this diagram, the potential energy of the luminescent centre  $Ce^{3+}$  is plotted on the vertical axis and the value of single parameter describing the effective displacement of the ion surrounding the activator,  $Q$ , is plotted on the horizontal axis. Promotion of the inner 4f electron to the outer 5 d states perturbs the surrounding ions, the lattice relaxes, and the potential energy curve changes as shown below in Fig. 6. The good adaptability of the position of the 4f–5d absorptions and the corresponding emissions make  $Ce^{3+}$  an important ingredient in light emitting materials. The respective excitation and emission pathways are indicated in Fig. 6 by arrows [35,36].

Thus Gadolinium silicate activated with  $Ce^{3+}$ ,  $(Gd_{1-x}Ce_x)_2SiO_5$ , has been found to be an efficient phosphor that can potentially be used as the blue-emitting component in field of lamp industry.

### 3.5.2. PL emission of $Dy^{3+}$ in $Gd_2SiO_5$

The photoluminescence excitation spectra of  $Gd_2SiO_5:Dy^{3+}$  optoelectronics phosphor at room temperature monitored at 576 nm for 0.5 mol % concentration is shown in Fig. 7. The excitation spectrum in the range 220–450 nm consists of various transitions of  $Gd^{3+}$  and  $Dy^{3+}$  ion. The excitation lines observed at 235 nm, 248 nm, 255 nm, 275 nm, 309 nm 315 and 326 nm are due to transitions from ground level,  $^8S_{7/2}$  to higher energy levels  $^6D_{7/2}$ ,  $^6D_{9/2}$ ,  $^6D_{11/2}$ ,  $^6I_{7/2}$ ,  $^6P_{3/2}$ ,  $^6P_{5/2}$ , and  $^6P_{7/2}$  of  $Gd^{3+}$  ion, respectively [37]. The excitation peaks observed at 351 nm, 365 nm, 426 nm and 455 nm are due to transitions from ground level,  $^6H_{15/2}$  to higher energy levels  $^6P_{7/2}$ ,  $^6P_{5/2}$ ,  $^4F_{7/2}$ ,  $^4G_{11/2}$  and  $^4I_{15/2}$  of  $Dy^{3+}$  ion, respectively [38,39]. Of these transitions  $^8S_{7/2} \rightarrow ^6I_7$  (275 nm) is more prominent; it is therefore used for the measurement of emission spectra of  $Dy^{3+}$ :  $Gd_2SiO_5$  phosphor. The presence of gadolinium transitions in the excitation spectra implies an energy transfer between  $Gd^{3+}$  and  $Dy^{3+}$  ions. This energy transfer may occur from  $^6I_7$  energy level of  $Gd^{3+}$  to the highest energy levels of  $Dy^{3+}$   $4f^85d$  or  $4f^9$  configuration.

$Dy^{3+}$  ions are excited to ( $4f^85d$ ) upper energy level under an excitation with 275 nm and from where these excited ions cascade

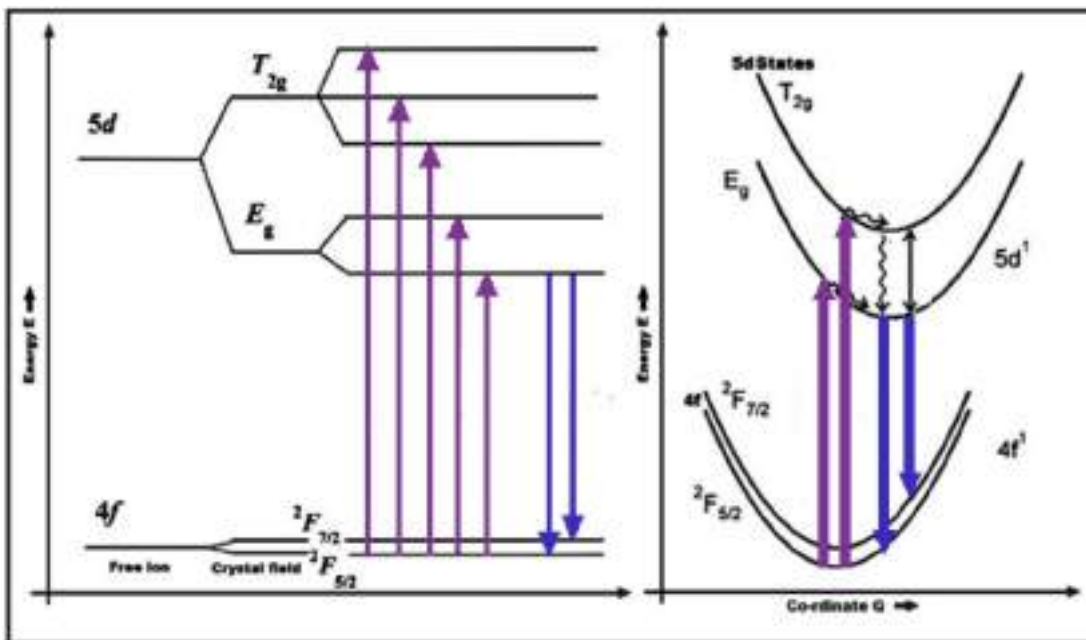


Fig. 6. Schematic illustration of partial energy levels and configurational coordinate diagram of  $\text{Ce}^{3+}$ .

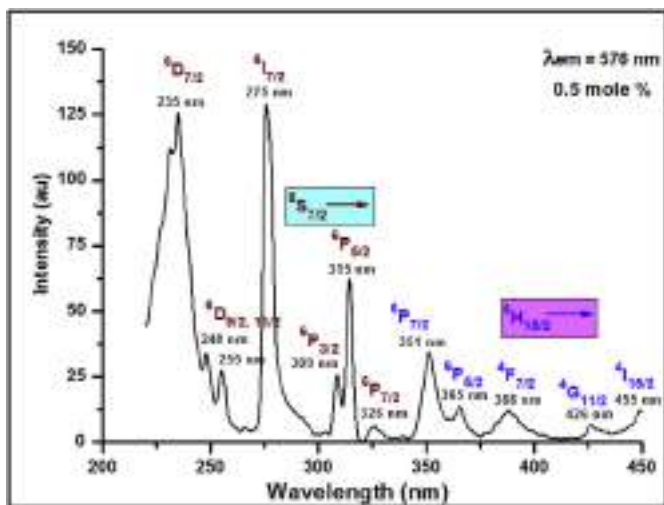


Fig. 7. Excitation spectrum of synthesised  $\text{Gd}_2\text{SiO}_5:\text{Dy}^{3+}$  phosphor.

rapidly towards  $^4\text{F}_{9/2}$  state through  $^4\text{G}_{11/2}$ ,  $^4\text{I}_{15/2}$  levels and then finally relaxes non-radiatively by populating  $^4\text{F}_{9/2}$  metastable state. The non-radiative decay is very fast because of closely spaced  $4\text{f}^9$  levels between  $^4\text{F}_{9/2}$  and  $4\text{f}^85\text{d}$  levels. On reaching  $^4\text{F}_{9/2}$  level these unstable ions relax radiatively by emitting fluorescence to the nearest lower lying multiplet  $^6\text{H}_j$  ( $J = 15/2, 13/2, 11/2$ ) energy level. The fluorescence spectrum exhibited two main peaks at 481 nm, 576 nm and with a weak band at 615 nm and 629 nm assigned to the transitions from  $^4\text{F}_{9/2}$  to  $^6\text{H}_{13/2}$ , and  $^6\text{H}_{11/2}$  as shown in the emission spectra of  $\text{Gd}_{2(1-x)}\text{SiO}_5:\text{Dy}_{2x}$  (Where  $x = 0.2, 0.5, 1$ , and 2 mol %) monitored at 275 nm excitation.

The intensity of 481 nm ( $^4\text{F}_{9/2} \rightarrow ^6\text{H}_{15/2}$ ) emission is almost same to that of 577 nm ( $^4\text{F}_{9/2} \rightarrow ^6\text{H}_{13/2}$ ) whereas intensity of 615 nm ( $^4\text{F}_{9/2} \rightarrow ^6\text{H}_{11/2}$ ) and 629 nm ( $^4\text{F}_{9/2} \rightarrow ^6\text{H}_{13/2}$ ) emissions are weakest. The blue emission at  $^4\text{F}_{9/2} \rightarrow ^6\text{H}_{15/2}$  is a magnetic dipole ( $\Delta J = 0, \pm 1$ ) transition which hardly varies with the host

environment around  $\text{Dy}^{3+}$  ion. The yellow emission due to  $^4\text{F}_{9/2} \rightarrow ^6\text{H}_{13/2}$  transition is a forced electric dipole transition (hyper-sensitive) with the selection rule  $\Delta J = \pm 2$  and it is strongly influenced by the crystal field strength around the rare earth ion. When  $\text{Dy}^{3+}$  occupies a non-inversion symmetry site (low local symmetry site; ED) yellow ( $^6\text{H}_{13/2}$ ) emission is more dominant and if it occupies an inversion symmetry site (high symmetry local site; MD) blue ( $^6\text{H}_{15/2}$ ) emission is more dominant in the emission spectrum [40]. In the present work, ED and MD transition has same intensity suggesting the symmetric nature of  $\text{Dy}^{3+}$  in the host  $\text{Gd}_2\text{SiO}_5$  phosphor.

From inset of Fig. 8, it is observed that variation of the dopant ions  $\text{Dy}^{3+}$  concentrations have affected the luminescence intensity in the host  $\text{Gd}_2\text{SiO}_5$ . Emission intensity increases in concentrations up to 0.5 mol % and thereafter intensity quenches further for higher concentration. This suggested that at lower concentrations the interaction between ions is negligible, and for higher concentration

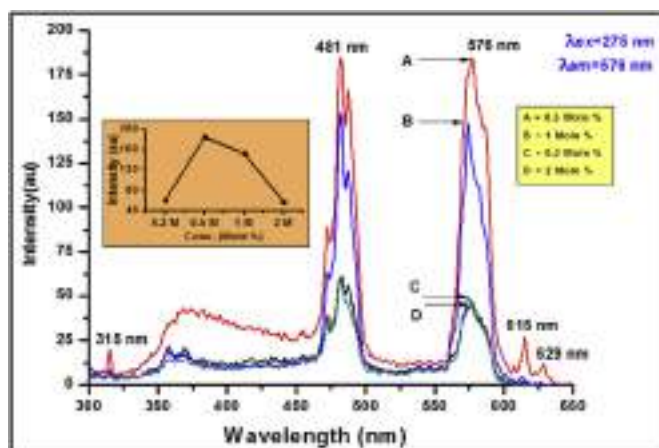


Fig. 8. Concentration dependence of emission spectra of synthesised  $\text{Gd}_2\text{SiO}_5:\text{Dy}^{3+}$  phosphor at  $\lambda_{\text{ex}} = 275$  nm.

the distance between ions decreases and they start interacting with each other due to enhanced non-radiative coupling between ions thus resulting in quenching of luminescence intensity. Migration of excitation energy takes place from one ion to another ion in a random style and finally transfers to acceptor ions leading to concentration quenching. Various interactions have also been reported to be responsible for the ion-ion relaxations that lead to quenching of fluorescence. Dipole-dipole interactions are considered to be more responsible for the self-quenching.

The intensity ratio of yellow/blue emission can be used to analyse the distortion around the  $Dy^{3+}$  ion in the  $Gd_2SiO_5$  phosphor. By carefully observing the emission spectra it is found that the emission intensity of yellow to blue (Y/B) ratio is almost 1, suggesting the symmetric nature of  $Dy^{3+}$  in the host  $Gd_2SiO_5$  phosphor [41].

Based on Dieke's energy level diagram, energy transfer could proceed from  $Gd^{3+}$  to  $Dy^{3+}$  as  $Gd^{3+}$  fluorescence state or excited state lies above the fluorescence state of  $Dy^{3+}$ . In the present study, based on the results obtained from the luminescence intensities of singly doped rare earth  $Dy^{3+}$  ions into  $Gd_2SiO_5$  phosphor, the role of host in energy transfer cannot be completely ruled out. As shown in Figs. 7 and 8, there were an excitation and emission peak at around 315 nm which could be assigned to the  $^8S_{7/2} - ^6P_{7/2}$  transitions of host  $Gd^{3+}$  [42]. The presence of  $Gd^{3+}$  excitation and emission peaks in the PL excitation spectrum indicated the existence of energy transfer from  $Gd^{3+}$  to  $Dy^{3+}$ . The schematic energy level diagram of  $Gd_2SiO_5: Dy^{3+}$  for possible excitation and emission processes were depicted in Fig. 9.

### 3.5.3. PL emission of $Eu^{3+}$ in $Gd_2SiO_5$

The photoluminescence excitation spectra of  $Gd_2SiO_5:Eu^{3+}$  optoelectronics phosphor at room temperature monitored at 615 nm for 5 mol % concentration is shown in Fig. 10. The excitation spectrum in the range 220–450 nm consists of strong absorption band with a maximum at 275 nm and several weak lines related to

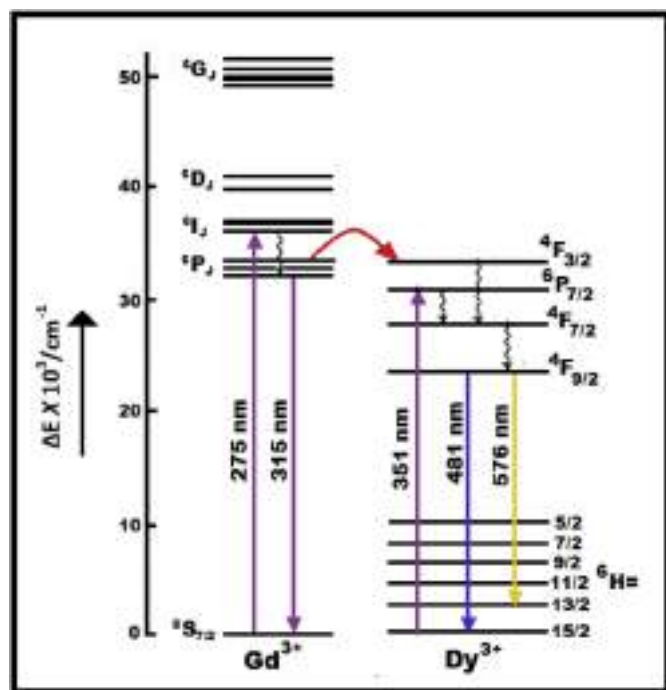


Fig. 9. Schematic illustration of partial energy level diagram showing energy transfer process in  $Gd_2SiO_5:Dy^{3+}$  phosphor at  $\lambda_{ex} = 275$  nm.

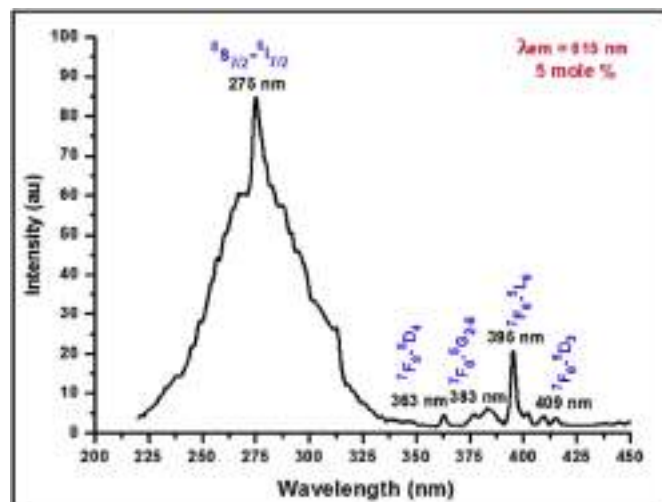


Fig. 10. Excitation spectrum of  $Gd_2SiO_5:Eu^{3+}$  phosphor.

various transitions of  $Gd^{3+}$  and  $Eu^{3+}$  ion. The sharp excitation line observed at 275 nm is due to transitions from ground level,  $^8S_{7/2}$  to higher energy levels  $^6P_{7/2}$  of  $Gd^{3+}$  ion.

The excitation peaks observed at 363 nm, 383 nm, 395 nm and 409 nm are due to transitions from ground level,  $^7F_0$  to higher energy levels  $^5D_4$ ,  $^5G_{2-6}$ ,  $^5L_6$ , and  $^5D_3$  of  $Eu^{3+}$  ion, respectively. Among them,  $^8S_{7/2} \rightarrow ^6P_7/2$  (275 nm) transition is more prominent; it is therefore used for the measurement of emission spectra of  $Eu^{3+}$ :  $Gd_2SiO_5$  phosphor. These weak lines are attributed to the f-f transitions within the  $4f^6$  configuration of the  $Eu^{3+}$  ions. The absorption intensity of the general f-f transitions of the  $Eu^{3+}$  ions in the longer wavelength region is very weak in comparison with  $Gd^{3+}$  ions. This indicates that the excitation of the  $Eu^{3+}$  ions is through the  $Gd^{3+}$  ions, i.e., by the energy transfer from the  $Gd^{3+}$  ions to  $Eu^{3+}$  ions [43,44].

The emission spectra of  $Gd_{2(1-x)}SiO_5:Eu_{2x}$  (Where  $x = 0.5, 1, 2, 5$  and 10 mol %) monitored at 275 nm excitation is shown in Fig. 11. Fluorescence spectra of  $Eu^{3+}$  doped  $Gd_2SiO_5$  were measured at room temperature. Upon ultraviolet (UV) excitation, the  $Gd_2SiO_5:Eu^{3+}$  phosphor exhibit a strong red luminescence.  $Eu^{3+}$  ions emit a characteristic red light with a number of narrow lines due to the  $4f \rightarrow 4f$  ( $^5D_0 \rightarrow ^7F_J = 0,1,2,3,4$ ) transitions [45]. After absorption of UV radiation and non-radiative relaxation to the lower 4f levels, luminescence occurs from the  $^5D_J$  (mainly  $^5D_0$ ) states of  $Eu^{3+}$ . The following emission transitions were observed at 579 nm ( $^3D_0 \rightarrow ^7F_0$ ), 587–594 nm ( $^5D_0 \rightarrow ^7F_1$ ), 615–628 nm ( $^5D_0 \rightarrow ^7F_2$ ), and very weak emission at 652 nm ( $^5D_0 \rightarrow ^7F_3$ ). Amongst them, the  $^5D_0 \rightarrow ^7F_2$  transitions at 615 nm are the strongest. The emission bands from 587 to 594 nm are less prominent and correspond to the magnetic dipole transition ( $^5D_0 \rightarrow ^7F_1$ ) of  $Eu^{3+}$  ion whereas the emission band at 615 nm is more prominent and is due to electric dipole transition ( $^5D_0 \rightarrow ^7F_2$ ) of  $Eu^{3+}$  ion. These two emission peaks are obtained due to crystal field splitting of  $^5D_0$  level to  $^7F_J$  ground state levels.

The luminescence spectra of  $Eu^{3+}$  ion is slightly influenced by surrounding ligands of the host material because the transition of  $Eu^{3+}$  involve only a redistribution of electrons within the inner 4f subshells. As shown in Fig. 11, the transition  $^5D_0 \rightarrow ^7F_2$  at 615 nm is much stronger than the transitions at  $^5D_0 \rightarrow ^7F_1$ , which suggests that the  $Eu^{3+}$  is located in a distorted (or asymmetric) cation environment. The sites for dopants in the host are determined by their ionic radii. The radius of  $Eu^{3+}$ , and  $Gd^{3+}$  are 95, and 94 pm, respectively which are almost same. Thus, the  $Eu^{3+}$  ions can readily occupy the

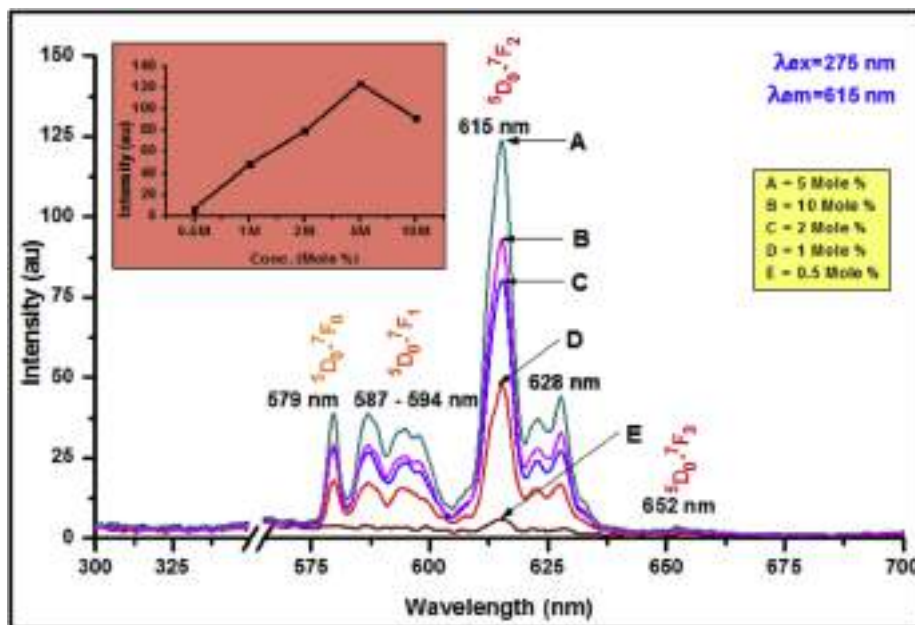


Fig. 11. Concentration dependence of emission spectra of  $Gd_2SiO_5:Eu^{3+}$  phosphor.

Gd sites in the lattice [46]. Although the emission bands are relatively broad (due to the high number of components of  $Eu^{3+}$  manifolds), the predominance of the  ${}^5D_0-{}^7F_2$  transition at 615 nm confers high red color purity for this compound.

The emission intensity is related to the concentration of the  $Eu^{3+}$  activator ions. With the increase of concentration of the  $Eu^{3+}$  ion, the distance between  $Eu^{3+}$  ions becomes less and this results in the migration of excitation energy amongst  $Eu^{3+}$  ions leading to quenching of the emission. The highest luminescent intensity is obtained at 5 mol % as shown in inset of Fig. 11 and then declines with the increase in concentration of the  $Eu^{3+}$  activator ions.

No characteristic emission in the range 310–315 nm from the  $Gd^{3+}$  ion was observed. It indicates that the energy transfer from the  $Gd^{3+}$  ion to  $Eu^{3+}$  ions is very efficient.

The partial energy levels, energetic structure, radiative processes and energy transfer in  $Gd^{3+} - Eu^{3+}$  are presented in Fig. 12. Upon UV excitation at  ${}^6I_7$  level of Gd, energy is transferred to  $Eu^{3+}$  through cross relaxation between  $Gd^{3+}$  in the  ${}^6I_7$  state and  $Eu^{3+}$  in the  ${}^7F_6$  ground state, resulting in  $Eu^{3+}$  in the  ${}^5D_0$  excited state and  $Gd^{3+}$  in the  ${}^6P_7/2$  state. A visible photon can be emitted from  $Eu^{3+}$  through the transitions of  ${}^5D_0 \rightarrow {}^7F_J$ . Thus visible photons can be produced through absorption of UV photon by  $Gd^{3+}$  ( ${}^8S_{7/2} \rightarrow {}^6I_7$ ). The respective emission and excitation pathways are indicated in figure by arrows [47].

#### 3.5.4. PL emission of $Tb^{3+}$ in $Gd_2SiO_5$

The photoluminescence excitation spectra of  $Gd_2SiO_5:Tb^{3+}$  optoelectronics phosphor at room temperature monitored at 545 nm for 0.5 mol % concentration is shown in Fig. 13. The overall excitation spectrum of  $Tb^{3+}$  can be divided into two parts. One, in the wavelength range 220 nm–320 nm comprising of  $4f^8 \rightarrow 4f^75d^1$  transitions and other part of the excitation spectrum, in the range 320 nm–450 nm which stands for  $4f^8 \rightarrow 4f^8$  transitions of the  $Tb^{3+}$  ions [48]. The excitation spectrum in the range 220–320 nm consists of various transitions of  $Gd^{3+}$  ion. The excitation transitions of  $Tb^{3+}$ , comprising  $4f^8 \rightarrow 4f^75d^1$  transitions are not observed. The excitation lines observed at 235 nm, 275 nm, 308 nm and 315 nm are due to transitions from ground level,  ${}^8S_{7/2}$  to higher energy levels  ${}^6D_{7/2}$ ,  ${}^6I_{7/2}$ ,  ${}^6P_{3/2}$ , and  ${}^6P_{5/2}$

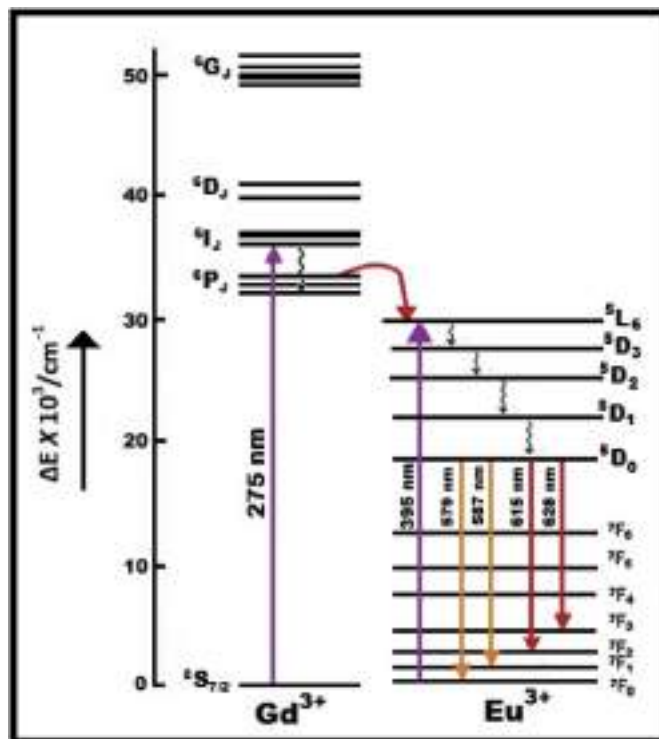


Fig. 12. Schematic illustration of partial energy level diagram showing energy transfer process in  $Gd_2SiO_5:Eu^{3+}$  phosphor at  $\lambda_{ex} = 275$  nm.

2, of  $Gd^{3+}$  ion, respectively. The excitation peaks in the region 320 to 450 nm have very low intensity and therefore were shown in the inset of Fig. 13.

There are two excitation peaks in the 320–450 nm region corresponding to transitions between  ${}^7F_6$  and the various excited states belonging to the  $4f^8$  electronic configuration of  $Tb^{3+}$  ions [49]. The excitation peaks at 354 nm ( ${}^7F_6 \rightarrow {}^5L_9$ ), and 381 nm ( ${}^7F_6 \rightarrow {}^5G_6$ ) due to forbidden 4f-4f transition of  $Tb^{3+}$  ion. As there

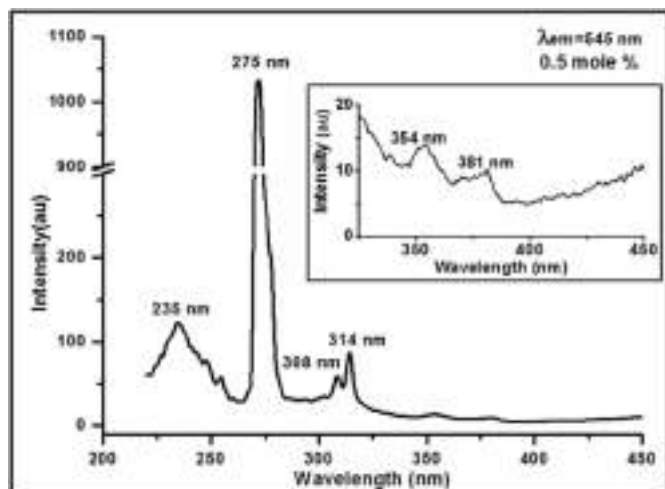


Fig. 13. Excitation spectrum of  $Gd_2SiO_5:Tb^{3+}$  phosphor.

were significant absorption in the UV region and the excitation at 275 nm has highest intensity, we have chosen  $\lambda_{ex} = 275$  nm to study the fluorescence properties of  $Gd_2SiO_5$  phosphor. Appearance of excitation bands of  $Gd^{3+}$  in the excitation spectra indicates that energy transfer from  $Gd^{3+}$  to  $Tb^{3+}$  takes place in  $Gd_2SiO_5:Tb^{3+}$  phosphor.

The emission of terbium doped phosphor is mainly in the green region due to  $^5D_4 \rightarrow ^7F_J$  transitions and the blue emission contributes to the emission from the higher level  $^5D_3 \rightarrow ^7F_J$  transitions. Fig. 14 shows the emission spectra of  $Gd_2SiO_5:Tb^{3+}$  phosphors under the excitation wavelength of 275 nm. The emission peaks at 381 nm, 417 nm, and 438 nm were due to  $^5D_3 \rightarrow ^7F_6$ ,  $^5D_3 \rightarrow ^7F_3$ , and  $^5D_3 \rightarrow ^7F_4$  transition of  $Tb^{3+}$  ions and the emission peaks at 487, 545 nm, 586 nm and 623 nm were assigned to the  $^5D_4 \rightarrow ^7F_J$  ( $J = 6, 5, 4$  and  $3$ ) transition of  $Tb^{3+}$  ions. As expected, the spectral shift was not observed because the  $4f$  shell of  $Tb^{3+}$  was well shielded by  $5s$  and  $5p$  shells. In addition to the emission peaks at longer

wavelength due to  $Tb^{3+}$  ions, emission peak due to the transmission of  $^6P_{5/2} \rightarrow ^8S_{7/2}$  transition of  $Gd^{3+}$  ions was also observed. The intensity of  $Gd^{3+}$  emission was found to be significantly very low.

From the emission spectra of  $Gd_2SiO_5:Tb^{3+}$  phosphors with different dopant concentrations it is noted that the  $Tb^{3+}$  emission spectrum in the  $Gd_2SiO_5$  lattice is dependent on its content due to cross-relaxation processes [50]. At low  $Tb^{3+}$  concentration, the blue emissions from  $^5D_3 \rightarrow ^7F_J$  transitions were prominent. When the activator concentration is increased, the blue emissions vanished and only the  $^5D_4 \rightarrow ^7F_J$  emissions appeared in the spectrum. The emission intensity of the green transitions increases linearly with the increase in concentration of  $Tb^{3+}$  up to 5 mol % as shown in inset of Fig. 14 [51].

Although the emission bands are relatively broad (due to the high number of components of  $Tb^{3+}$  manifolds), the predominance of the  $^5D_4 \rightarrow ^7F_5$  transition at 545 nm confers high green color purity for this compound.

The enhanced emission of  $Tb^{3+}$  ions following energy transfer process from  $Gd^{3+}$  to  $Tb^{3+}$  in  $Gd_2SiO_5$  lattice was due to energy migration among  $Gd^{3+}$  ions and which were trapped by  $Tb^{3+}$  ions, hence resulting in a decrease in  $Gd^{3+}$  emission and an increase in  $Tb^{3+}$  emission. The weak emission intensity at 315 nm indicates that the energy transfer between  $Gd^{3+}$  ions becomes more probable than the radiative decay of the  $Gd^{3+}$  ions.

Schematic illustration of partial energy level diagram showing energy transfer process of  $Gd^{3+} \rightarrow Tb^{3+}$  in  $Gd_2SiO_5:Tb^{3+}$  phosphor at  $\lambda_{ex} = 275$  nm is shown in following Fig. 15. It is clear that the energy level difference between  $^6P_J$  and  $^8S_{7/2}$  is about  $32,000 \text{ cm}^{-1}$  or the energy level difference between  $Gd^{3+}$  is similar to that in the range of  $36,000\text{--}34,000 \text{ cm}^{-1}$  of  $Tb^{3+}$ . The excitation energy of  $Gd^{3+}$  migrates in lattice  $Gd_2SiO_5$  until a  $Tb^{3+}$  ion is reached. After a fast nonradiative relaxation to  $^5D_{3,4}$  states, a visible photon is emitted [52].

The interesting result is that the highest emission intensity for  $Ce^{3+}$  and  $Dy^{3+}$  is below 1%, but it is about 5% for  $Eu^{3+}$  and  $Tb^{3+}$ . This is probably due to better and efficient energy transfer mechanism in  $Ce^{3+}$  and  $Dy^{3+}$  as compared to  $Eu^{3+}$  and  $Tb^{3+}$ . Moreover the distribution coefficient of  $RE^{3+}$  in  $RE:GSO$  crystals depend on the

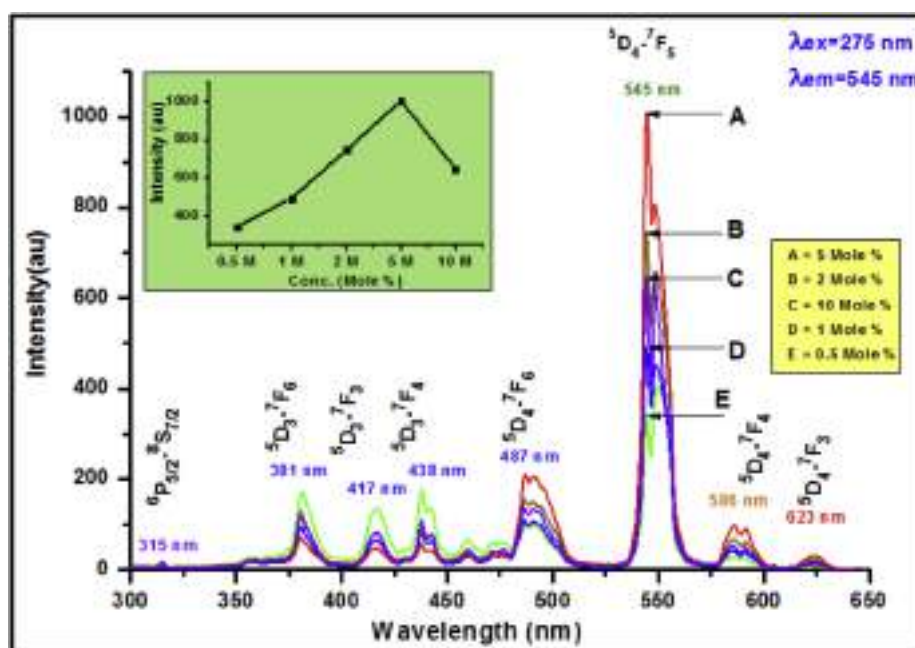


Fig. 14. Concentration dependence of emission spectra of  $Gd_2SiO_5:Tb^{3+}$  phosphor.

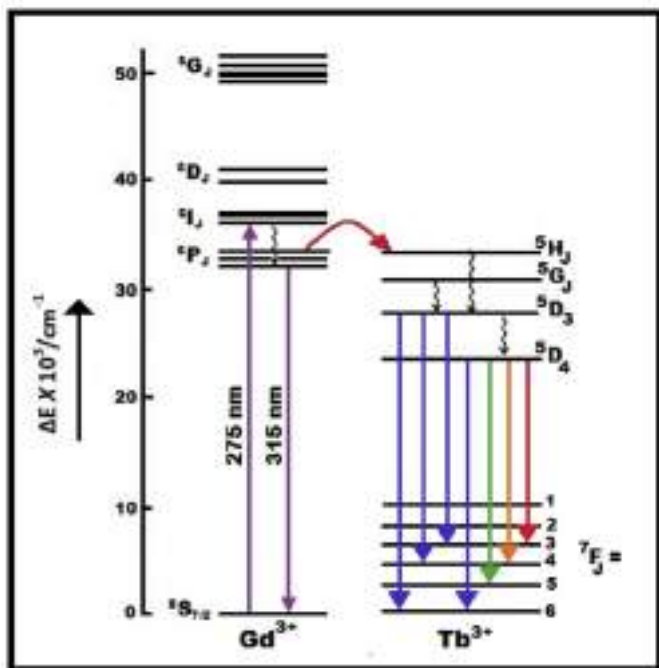


Fig. 15. Schematic illustration of partial energy level diagram showing energy transfer process in  $\text{Gd}_2\text{SiO}_5:\text{Tb}^{3+}$  phosphor at  $\lambda_{\text{ex}} = 275 \text{ nm}$ .

solubility of RE ion in the RE:GSO host lattice for  $\text{Eu}^{3+}$  and  $\text{Tb}^{3+}$  it is high hence doping level can be achieved [53].

### 3.6. Chromatic properties

Most lighting specifications refer to color in terms of the 1931 CIE chromatic color coordinates which recognizes that the human visual system uses three primary colors: red, green, and blue [54,55]. In general, the color of any light source can be represented on the (x, y) coordinate in this color space. Fig. 16 shows the Commission International de l'Eclairage (CIE) chromaticity coordinates of the prepared phosphor  $\text{Gd}_2\text{SiO}_5:\text{RE}^{3+}$  phosphor

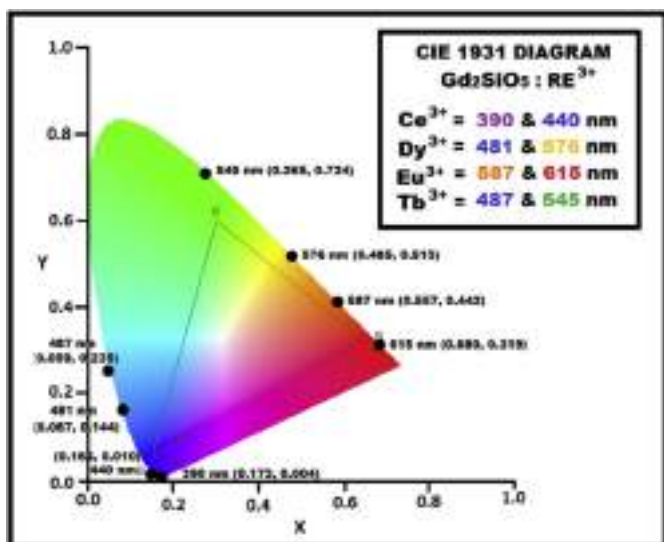


Fig. 16. CIE diagram of  $\text{Gd}_2\text{SiO}_5:\text{RE}^{3+}$  phosphor (Where  $\text{RE}^{3+} = \text{Ce}^{3+}, \text{Dy}^{3+}, \text{Eu}^{3+}$  and  $\text{Tb}^{3+}$ ).

( $\text{RE}^{3+} = \text{Ce}^{3+}, \text{Dy}^{3+}, \text{Eu}^{3+}$  and  $\text{Tb}^{3+}$ ). The chromatic co-ordinates (X, Y) are calculated using the color calculator radiant imaging software and are summarized in following Table 1.

## 4. Conclusion

The  $\text{Gd}_2\text{SiO}_5:\text{RE}^{3+}$  ( $\text{RE}^{3+} = \text{Ce}^{3+}, \text{Dy}^{3+}, \text{Eu}^{3+}$  and  $\text{Tb}^{3+}$ ) optoelectronics phosphor has been prepared by the solid state flux diffusion method. PL properties in the UV and visible region which are characteristics for optoelectronic devices were studied. XRD analysis was carried out to study phase purity of the prepared optoelectronics phosphor. FT-IR spectra were recorded to show the functional groups for pure  $\text{Gd}_2\text{SiO}_5$  sample. CIE study was carried out to study color quality. Cross relaxation process led to non-radiative quenching therefore the emission intensity of  $\text{RE}^{3+}$  ions decreased with increasing amount of doped  $\text{RE}^{3+}$  ions. It is confirmed that a  $\text{Gd}^{3+}$  ion which absorbs the energy of a UV photon can transfer part of its energy to radiative energy state of a  $\text{RE}^{3+}$  ion through cross relaxation resulting in the emission of visible photons from  $\text{RE}^{3+}$  ions. As oxysalts are easier to produce and cheaper than fluorides, investigation of  $\text{Gd}_2\text{SiO}_5:\text{RE}^{3+}$  will open a new way for oxysalts to serve as host materials for new phosphors suitable for a modern lighting applications.

## Author contributions section

All authors are equal contribution in this paper.

## Declaration of competing interest

The effect of the  $\text{RE}^{3+}$  ( $\text{RE}^{3+} = \text{Ce}^{3+}, \text{Dy}^{3+}, \text{Eu}^{3+}$  and  $\text{Tb}^{3+}$ ) concentration on the luminescence properties of  $\text{Gd}_2\text{SiO}_5:\text{RE}^{3+}$  optoelectronics materials were also studied. The investigated prepared  $\text{Gd}_2\text{SiO}_5$  phosphors may be suitable for lighting based devices.

## Appendix A. Supplementary data

Supplementary data to this article can be found online at <https://doi.org/10.1016/j.molstruc.2020.128397>.

## References

- [1] C.H. Huang, T.W. Kuo, T.M. Chen, Thermally stable green  $\text{Ba}_3\text{Y}(\text{PO}_4)_3:\text{Ce}^{3+}, \text{Tb}^{3+}$  and red  $\text{Ca}_3\text{Y}(\text{AlO}_3(\text{BO}_3)_4):\text{Eu}^{3+}$  phosphors for white-light fluorescent lamps, *Optic Express* 19 (2011) A1.
- [2] T.W. Kuo, T.M. Chen, A green-emitting phosphor  $\text{Sr}_3\text{La}(\text{PO}_4)_3:\text{Ce}^{3+}, \text{Tb}^{3+}$  with efficient energy transfer for fluorescent lamp, *J. Electrochem. Soc.* 157 (2010) J216.
- [3] T. Sakamoto, S. Kousaka, K. Uematsu, T. Ishigaki, K. Toda, M. Sato, Synthesis and properties of  $\text{Na}_3\text{YSi}_2\text{O}_7:\text{Eu}^{3+}$  phosphor for fluorescent lamp, *Phys. Status Solidi* 8 (2011) 2731.
- [4] X.H. Li, Y.Y. Wang, Q.Z. Shi, Influence of ball milling parameters on blue phosphor for cathode ray tube, *Displays* 29 (2008) 316.
- [5] L. Ozawa, M. Itoh, Cathode ray tube phosphors, *Chem. Rev.* 103 (2003) 3835.
- [6] S.Y. Kim, S.H. Cho, J.W. Shin, J.K. Park, S.S. Kang, S.H. Nam, Synthesis and characterization of  $\text{Gd}_2\text{O}_3:\text{Eu}$  nano phosphors for application as X-ray image detectors, *J. Kor. Phys. Soc.* 50 (2007) 1774.
- [7] I. Kandarakis, D. Cavouras, E. Kanellopoulos, C.D. Nomicos, G.S. Panayiotakis, Image quality evaluation of  $\text{YVO}_4:\text{Eu}$  phosphor screens for use in x-ray medical imaging detectors, *Radiat. Meas.* 29 (1998) 481.
- [8] K. Takagi, T. Fukazawa, Cerium-activated  $\text{Gd}_2\text{SiO}_5$  single crystal scintillator, *Appl. Phys. Lett.* 42 (1983) 43.
- [9] H. Loudyi, Y. Guyot, J.C. Gacon, C. Pedrini, M.F. Joubert, Understanding the scintillation efficiency of cerium-doped LSO, LYSO, YSO and LPS crystals from microwave study of photoconductivity and trapping, *Opt. Mater.* 30 (2007) 26.
- [10] T.E. Peters, Cathodoluminescent  $\text{Ln}_x(\text{SiO}_2)_x:\text{Tb}$  phosphors, *J. Electrochem. Soc.* 116 (1969) 985.
- [11] Cathodoluminescence of Ce-doped  $\text{Gd}_2\text{SiO}_5$  and  $\text{Gd}_9.33(\text{SiO}_4)_6\text{O}_2$  phosphor under continuous electron irradiation, *J. Alloys Compd.* 509 (2011) 800.
- [12] I.G. Valais, I.S. Kandarakis, D.N. Nikolopoulos, I.A. Sianoudis, G.K. Loudos,

- N.D. Giokaris, K.S. Nikita, D.A. Cavouras, N. Dimitropoulos, C.D. Nomicos, G.S. Panayiotakis, Luminescence properties of LuYSiO<sub>5</sub>: Ce, Gd<sub>2</sub>SiO<sub>5</sub>:Ce, and CsI: Tl single crystal scintillators under X-ray excitation, for use in medical imaging systems, IEEE Nuclear Science Symposium Conference Record 3 (2005) 1323.
- [13] Y. Zhang, J. Bin, L. Mei, Z. Huang, Synthesis and luminescence properties of reddish orthosilicate oxyapatite phosphor LiGd<sub>9</sub>(SiO<sub>4</sub>)<sub>6</sub>O<sub>2</sub>:Sm<sup>3+</sup>, J. Lumin. 206 (2018) 615.
- [14] R.C. Ropp, Studies in Inorganic Chemistry 21, Luminescence and the Solid State, second ed., Elsevier, Amsterdam, 1991, p. 139.
- [15] M. Jie, G. Zhao, X. Zheng, L. Su, H. Pang, X. He, J. Xu, Crystal growth and optical properties of Gd<sub>1.99-x</sub>YxCe<sub>0.01</sub>SiO<sub>5</sub> single crystals, J. Cryst. Growth 277 (2005) 175.
- [16] K. Takagi, Y. Chen, Li M.P. Damicanin, A.S. de Camargo, M.R. Davalos, L.A.O. Nunes, J. Phys. Condens. Matter 14 (2006) 3353.
- [17] G.X. Liu, G.Y. Hong, D.X. Sun, Synthesis and characterization of SiO<sub>2</sub>/Gd<sub>2</sub>O<sub>3</sub>:Eu core-shell luminescent materials, J. Colloid Interface Sci. 278 (2004) 133.
- [18] L.E. Muresan, B.F. Oprea, A.I. Cadis, I. Perhaita, O. Ponta, Studies on Y 2 SiO 5:Ce phosphors prepared by gel combustion using new fuels, J. Alloys Compd. 615 (2014) 795–803.
- [19] Y. Parganiha, J. Kaur, V. Dubey, R. Shrivastava, D. Chandrakar, Violet blue emission and thermoluminescence glow curve analysis of Gd<sub>2</sub>SiO<sub>5</sub>:Ce<sup>3+</sup> phosphor, Optik - International Journal for Light and Electron Optics 127 (15) (2016) 6243.
- [20] Y. Parganiha, J. Kaur, N. Dubey, V. Dubey, R. Shrivastava, S.J. Dhole, H.C. Swart, Luminescence and structural properties of Gd<sub>2</sub>SiO<sub>5</sub> Eu<sup>3+</sup> phosphors synthesized from the modified solid state method, Ceram. Int. 43 (12) (2017) 9084.
- [21] A. Kioul, L. Mascia, Compatibility of polyimide-silicate ceramics induced by alkoxysilane silane coupling agents, J. Non-Cryst. Solids 175 (1994) 169.
- [22] J.R. Smyth, Hydrogen in high pressure silicate and oxide mineral structures, Rev. Mineral. Geochem. 62 (2006) 85.
- [23] K. Takagi, T. Fukazawa, Cerium-activated Gd<sub>2</sub>SiO<sub>5</sub> single crystal scintillator, Appl. Phys. Lett. 42 (1983) 43.
- [24] M. Sekita, Y. Miyazawa, T. Akahane, T. Chiba, Optical studies of Ce-doped Gd<sub>2</sub>SiO<sub>5</sub> single crystals, J. Appl. Phys. 66 (1989) 373.
- [25] Y. Dong, J. Xu, G. Zhou, G. Zhao, M. Jie, L.Y. Yang, Blue upconversion luminescence generation in Ce<sup>3+</sup>: Gd<sub>2</sub>SiO<sub>5</sub> crystals by infrared femtosecond laser irradiation, Optic Express 14 (2006) 1899.
- [26] E.J. Bosse, G.A. Hirata, L.E. Shea-Rohwer, J. McKittrick, Improving the efficiency of a blue-emitting phosphor by an energy transfer from Gd<sup>3+</sup> to Ce<sup>3+</sup>, J. Lumin. 104 (2003) 47.
- [27] W. Mangesha, T.D. Taulbee, J.D. Valentine, B.D. Rooney, Gd<sub>2</sub>SiO<sub>5</sub>(Ce<sup>3+</sup>) and BaF<sub>2</sub> measured electron and photon responses, Nucl. Instrum. Methods Phys. Res. A. 486 (2002) 448.
- [28] V. Jarý, E. Mihóková, J.A. Mareš, A. Beitlerová, D. Kurtsev, O. Sidletskiy, M. Nikl, Comparison of the scintillation and luminescence properties of the (Lu<sub>1-x</sub>Gd<sub>x</sub>)<sub>2</sub>SiO<sub>5</sub>:Ce single crystal scintillators, J. Phys. D Appl. Phys. 47 (2014) 365304.
- [29] G. Wang, J. Li, K. Qian, J. Yu, R. Xu, A family of luminescent microporous lanthanide silicates, Stud. Surf. Sci. Catal. 170 (2007) 160.
- [30] D. Zhai, L. Ning, Y. Huang, G. Liu, Ce–O covalence in silicate oxyapatites and its influence on luminescence dynamics, J. Phys. Chem. C 118 (29) (2014) 16051.
- [31] Y. Parganiha, J. Kaur, V. Dubey, R. Shrivastava, D. Chandrakar, Violet blue emission and thermoluminescence glow curve analysis of Gd<sub>2</sub>SiO<sub>5</sub>:Ce<sup>3+</sup> phosphor, Optik 127 (2016) 6243.
- [32] C.W.E. van Eijk, J. Andriessen, P. Dorenbos, R. Visser, Ce<sup>3+</sup> doped inorganic scintillators, Nucl. Instrum. Methods Phys. Res. A. 348 (1994) 546.
- [33] S. Shimizu, H. Ishibashi, A. Ejiri, S. Kubota, Luminescence decay of Ce-doped GSO under excitation of VUV photons with energy less than 30 eV at room temperature, Nucl. Instrum. Methods Phys. Res. A. 486 (2002) 490.
- [34] R.Y. Lee, F.L. Zhang, J. Penczek, B.K. Wagner, P.N. Yocom, C.J. Summers, Investigation of Ce-doped silicates for low voltage field emission displays, J. Vac. Sci. Technol. B 16 (1998) 855.
- [35] H. Ishibashi, Mechanism of luminescence from a cerium-doped gadolinium orthosilicate (Gd<sub>2</sub>SiO<sub>5</sub>) scintillator, Nucl. Instrum. Methods Phys. Res. A. 294 (1990) 271.
- [36] M.V. Korzhik, W.P. Trower, Origin of scintillation in cerium-doped oxide crystals, Appl. Phys. Lett. 66 (1995) 2327.
- [37] L. Zhu, C. Zuo, Z. Luo, A. Lu, Photoluminescence of Dy<sup>3+</sup> and Sm<sup>3+</sup>: SiO<sub>2</sub>-Al<sub>2</sub>O<sub>3</sub>-LiF-CaF<sub>2</sub> glasses, Physica B 405 (2010) 4401.
- [38] B.R. Judd, Hypersensitive transitions in rare earth ions, J. Chem. Phys. 44 (1966) 839.
- [39] I. Pekgozlu, S. Cakar, Photoluminescence properties of Li<sub>6</sub>CaB<sub>3</sub>O<sub>8.5</sub>:M<sup>3+</sup> (M<sup>3+</sup>: Dy and Sm), J. Lumin. 132 (2012) 2312.
- [40] J. Suresh kumar, K. Pavani, A. Mohanbabu, Neeraj Kumar Giri, S.B. Rai, L. Rama Moorthy, Fluorescence characteristics of Dy<sup>3+</sup> ions in calcium fluoroborate glasses, J. Lumin. 130 (2010) 1916.
- [41] L. Zhang, H. Zhong, X. Li, L. Cheng, L. Yao, J. Sun, J. Zhang, R. Hua, B. Chen, Solid state reaction synthesis and luminescence properties of Dy<sup>3+</sup> doped Gd<sub>2</sub>Mo<sub>3</sub>O<sub>9</sub> Phosphor, Physica B 407 (2012) 68.
- [42] G.C. Han, Y.H. Wang, C.F. Wu, J.C. Zhang, Y.H. Lu, Hydrothermal synthesis and vacuum ultraviolet-excited luminescence properties of novel Dy<sup>3+</sup> doped GdPO<sub>4</sub> white light phosphors, Chin. Phys. Lett. 26 (2009), 067803.
- [43] R.T. Wegh, H. Donker, K.D. Oskam, et al., Visible quantum cutting in Eu<sup>3+</sup> doped gadolinium fluorides via down conversion, J. Lumin. 82 (1999) 93.
- [44] C.R. Ronda, Phosphors for lamps and displays: an application view, J. Alloys Compd. 225 (1995) 534.
- [45] Y. u Chen, B. Liu, C. Shi, M. Kirm, M. True, S. Vielhauer, G. Zimmerer, Luminescent properties of Gd<sub>2</sub>SiO<sub>5</sub> powder doped with Eu<sup>3+</sup> under VUV–UV excitation, J. Phys: Condens Matter 17 (2005) 1217.
- [46] M.D. Dramićanin, et al., Synthesis, structural and luminescent properties of Gd<sub>2</sub>O<sub>3</sub>-SiO<sub>2</sub>:Eu<sup>3+</sup> nanopowder composites, Mater. Sci. Forum 518 (2006) 455.
- [47] R. Krsmanovi, Z. Andri, M. Marinovi-Cincovi, I. Zekovi, M.D. Dramićanin, Optical and thermal investigation of sol-gel derived Eu<sup>3+</sup>:Y<sub>2</sub>SiO<sub>5</sub> nanoparticles, Proceedings of the International School and Conference on Optics and Optical Materials, ISCOM07, Belgrade, Serbia 112 (5) (2007) 975.
- [48] J. Fu, M. Kobayashi, Parker, Terbiu-activated heavy scintillating glasses, J. Lumin. 128 (2008) 99.
- [49] H.H. Huang, B. Yan, In-situ sol–gel synthesis of luminescent Gd<sub>2</sub>SiO<sub>5</sub>:Tb<sup>3+</sup> nanophosphors derived from assembling hybrid precursors, Inorg. Chem. Commun. 7 (4) (2004) 595.
- [50] Y.H. Zheng, et al., Ionic liquid-based luminescent Gd<sub>2</sub>SiO<sub>5</sub>: Tb submicro-meter phosphors, Adv. Mater. Res. 442 (2012) 8.
- [51] J. Shmulovich, G.W. Berkstresser, C.D. Brandle, A. Valentino, Single-crystal rare-earth-doped yttrium orthosilicate phosphors, J. Electrochem. Soc. 135 (12) (1988) 3141.
- [52] V. Babin, A. Krasnikov, J.A. Mareš, M. Nikl, K. Nitsch, N. Solovieva, S. Zazubovich, Luminescence spectroscopy of the Gd-rich Ce<sup>3+</sup>, Tb<sup>3+</sup> and Mn<sup>2+</sup>-doped phosphate glasses, Phys. Status Solidi (a) 196 (2003) 484.
- [53] C. Yan, G. Zhao, L. Su, X. Xu, L. hang, J. Xu, Growth and spectroscopic characteristics of Yb:GSO single crystal, J. Phys. Condens. Matter 18 (4) (2006) 1325.
- [54] G.B. Stringfellow, M.G. Craford, High Brightness Light Emitting Diodes, Semiconductors and Semimetals, Academic Press, 1997, p. 48.
- [55] S. Shionoya, W.M. Yen, Phosphor Handbook, Phosphor Research Society, CRC Press, 1998, p. 459.



# Eu<sup>3+</sup> and Dy<sup>3+</sup>-activated LaAlO<sub>3</sub> phosphor for solid-state lighting

S. K. Ramteke<sup>1</sup> · A. N. Yerpude<sup>1</sup> · N. S. Kokode<sup>2</sup> · V. V. Shinde<sup>3</sup> · S. J. Dhoble<sup>4</sup>

Received: 2 November 2019 / Accepted: 4 March 2020  
© Springer Science+Business Media, LLC, part of Springer Nature 2020

## Abstract

Rare earth Eu<sup>3+</sup> and Dy<sup>3+</sup>-activated LaAlO<sub>3</sub> phosphor were prepared by wet chemical method. The prepared phosphors were characterized by, X-ray diffraction (XRD) for phase purity, scanning electron microscopy (SEM) for morphology and photoluminescence (PL) emission and excitation spectra. SEM analysis does not reveal the crystal structure; however, it shows that the prepared phosphor has irregular morphology with particle size in micron range. Under both 395 nm and 466 nm excitation, LaAlO<sub>3</sub>:Eu<sup>3+</sup> phosphor shows emission at 593 nm and 614 nm. LaAlO<sub>3</sub>:Dy<sup>3+</sup> phosphor shows emission at 484 nm and 575 nm when excited by wavelength of 351 nm. The synthesized phosphors have mercury-free excitation, and therefore, prepared phosphor might be applicable in environmental-friendly solid-state lighting.

## 1 Introduction

Currently, phosphor-converted white light-emitting diodes (w-LEDs) have been attracted worldwide attention as a new source for the solid-state lighting to next generation due to their special advantages such as long lifetimes, luminous efficiency, absence of mercury, low energy consumption, weak environmental impact, excellent chemical as well as physical stability, availability of final products in different sizes, and so on [1, 2]. A lot of studies have been investigating different luminescent materials to help the growth of suitable phosphors. Phosphors are also useful for producing white light when they are excited by blue or near-ultraviolet (NUV) lights (300–420 nm). It is very important to choose the right compound materials and assure they have outstanding physical and chemical stability for obtaining phosphors with highly proficient emissions [3, 4]. Lanthanides elements such as Tb<sup>3+</sup>, Pr<sup>3+</sup>, Eu<sup>3+</sup>, Sm<sup>3+</sup>, Dy<sup>3+</sup>, La<sup>3+</sup> etc. have been broadly used as luminescent centres in phosphor materials due to their intense transitions in

d→f shell. Between these ions, dysprosium and europium is mostly used as a dopant and it has been used in phosphor materials for developing solid-state lighting [5–7]. Recently, there is developing interest in luminescence of trivalent rare earth ions such as tungstate, phosphates, borates, aluminates and molybdates; among which rare earth-doped aluminate are especially attractive due to their magnificent physical, chemical and thermal stability, high UV transparency and high-luminescence efficiency [8–14]. Research on the luminescence of a series of such compounds offers much valuable data for optical applications such as flat panel displays, high-density optical storage, temperature sensors, under sea communication, various fluorescent devices, colour display and visible solid-state lasers traffic signals, safety indicators on emergency appliances and less energy-consuming light sources. Oxide phosphors are non-toxic in nature due to this they are environmental friendly [15, 16]. Lanthanum aluminate is well known for its perovskite-like crystalline structure. Materials having these properties are applicable for various technological applications due to their special magnetic and electrical properties. Maczka et al. reported the LaAlO<sub>3</sub> phosphors doped with Eu<sup>3+</sup> and Er<sup>3+</sup> ions were synthesized by low temperature method and studied its optical properties [17]. Hernández et al. synthesized the LaAlO<sub>3</sub> phosphors doped with Eu<sup>3+</sup> prepared by Modified Pechini (MP) method and studied its photoluminescence, thermoluminescence properties for ionizing radiation dosimeter [18]. Mao et al. developed LaAlO<sub>3</sub>:Eu phosphor for white light emitting diode [19]. In addition, Eu<sup>3+</sup>-doped LaAlO<sub>3</sub> nano-systems reported by Quiang et al. which is synthesized by

✉ A. N. Yerpude  
atulyerpude@gmail.com

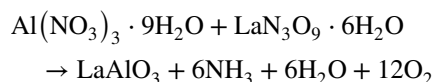
<sup>1</sup> Department of Physics, N.H.College, Bramhapuri, Chandrapur 441206, India  
<sup>2</sup> N.H.College, Bramhapuri, Chandrapur 441206, India  
<sup>3</sup> Department of Electronics, Bajaj College of Science, Wardha 442001, India  
<sup>4</sup> Department of Physics, RTM Nagpur University, Nagpur 440033, India

a simple hydrothermal method [20]. Jin et al. successfully synthesized the  $\text{LaAlO}_3\text{:Eu}^{3+}$  phosphors by coprecipitation molten salt synthesis and found phosphor may be good candidate in color display [21]. It was our main interest to synthesize  $\text{LaAlO}_3$  doped with rare earth ions prepared via low temperature initiated wet chemical process and investigating their photoluminescence properties for solid state lighting applications.

## 2 Experimental

The  $\text{LaAlO}_3\text{:Eu}^{3+}$  and  $\text{LaAlO}_3\text{:Dy}^{3+}$  phosphors were prepared using wet chemical method. For the synthesis of  $\text{LaAlO}_3\text{:Eu}^{3+}$ , analytical-grade reagents of Lanthanum nitrate ( $\text{LaN}_3\text{O}_9\cdot 6\text{H}_2\text{O}$ ), Aluminium nitrate ( $\text{Al}(\text{NO}_3)_3\cdot 9\text{H}_2\text{O}$ ) and Europium oxide (III) ( $\text{Eu}_2\text{O}_3$ ) were used as starting materials.

An appropriate amounts of Lanthanum nitrate, Aluminium nitrate powders were taken in beaker, dissolved in distilled water and stirred it until the solution becomes transparent. The Europium oxide was converted into nitrate by dissolving it in appropriate amount of dilute  $\text{HNO}_3$ , and then added this solution in beaker. The solution was then kept on magnetic stirrer maintained at  $80\text{ }^\circ\text{C}$  for 10 h. The final product was using funnel and filter paper, dried and grinded in mortar pestle to get fine powder. Finally, the fine powder was annealed at  $800\text{ }^\circ\text{C}$  for 3 h which was then used for further characterization. Similar procedure was applied for  $\text{LaAlO}_3\text{:Dy}^{3+}$  phosphor. The basic chemical reaction is given as follows



## 3 Results and discussion

### 3.1 X-ray diffraction pattern of $\text{LaAlO}_3$ phosphor

The XRD pattern of the  $\text{LaAlO}_3$  powder sample annealed at  $800\text{ }^\circ\text{C}$  is shown in Fig. 1. XRD is well matched with the standard JCPDS file no. 820478. All the peaks in the XRD pattern is in accordance with JCPDS file no. 820478, which indicates that the prepared phosphor has fully turned into  $\text{LaAlO}_3$  phase.

### 3.2 Morphology of $\text{LaAlO}_3$ phosphors

The surface morphology of pure  $\text{LaAlO}_3$  phosphors prepared via a wet chemical method is shown in Fig. 2. It is clearly evident that, the powders show highly porous structure, agglomeration of several crystals with an irregular

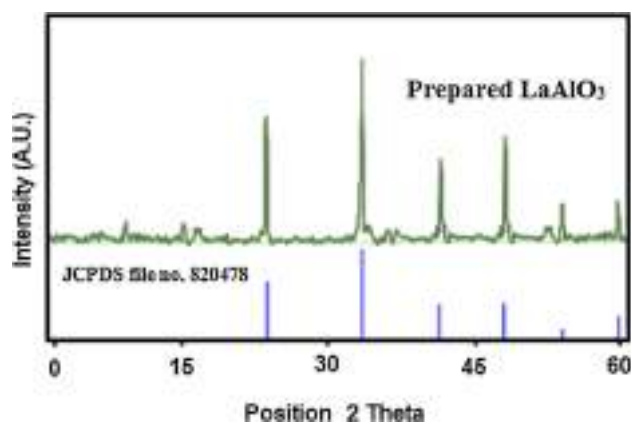


Fig. 1 XRD pattern of  $\text{LaAlO}_3$  phosphor

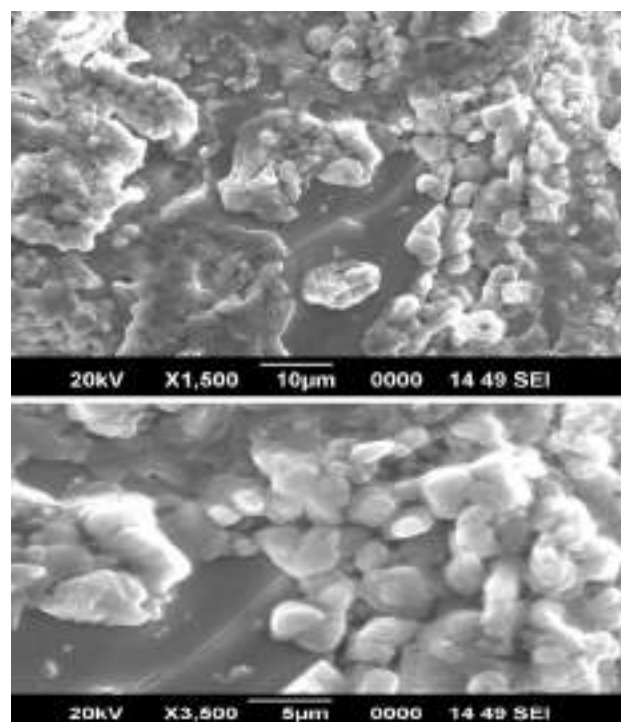


Fig. 2 SEM micrographs of  $\text{LaAlO}_3$  phosphor

morphology, large voids and shapes. The particle size can be seen in micro-meter range. This type of morphology is due to the escape of a large volume of gas during wet chemical process. The SEM image at two different magnifications shows that crystallites have no uniform shapes and sizes.

### 3.3 Photoluminescence properties of $\text{LaAlO}_3\text{:Eu}^{3+}$ phosphor

The luminescence emission shows the characteristic peaks associated with the trivalent Europium ion's inter-electronic energy level transitions. Figure 3 shows the excitation

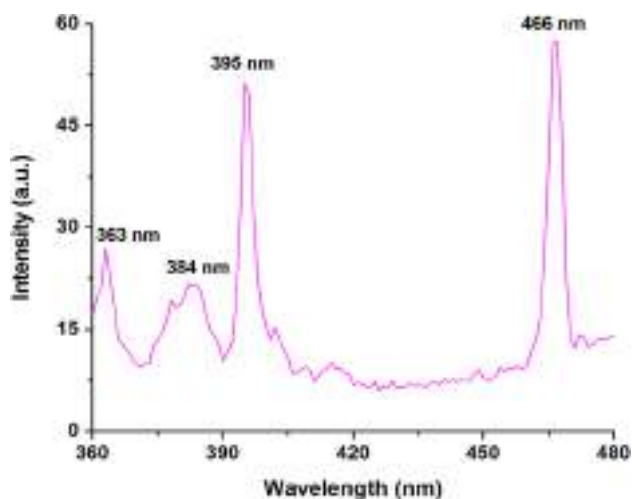


Fig. 3 Excitation spectrum of  $\text{LaAlO}_3:\text{Eu}^{3+}$  phosphor ( $\lambda_{\text{em.}}=614$  nm)

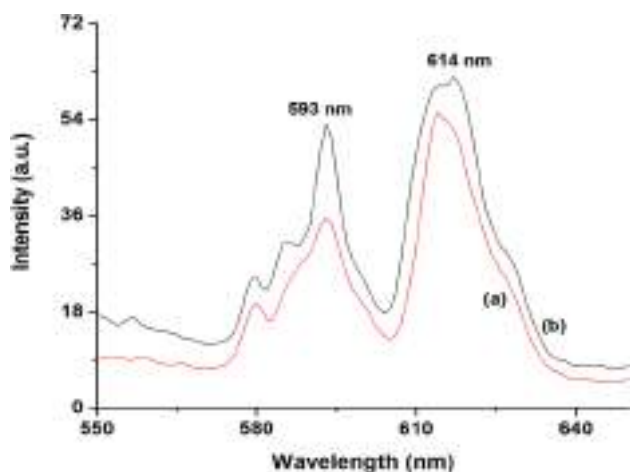


Fig. 4 Emission spectrum of  $\text{LaAlO}_3:\text{Eu}^{3+}$  phosphor, where a  $\lambda_{\text{ex.}}=395$  nm, b  $\lambda_{\text{ex.}}=466$  nm

spectra of  $\text{LaAlO}_3:\text{Eu}^{3+}$  phosphor. The excitation spectrum consists of series of peaks located at 363 nm, 384 nm, 395 nm and 466 nm. When  $\text{LaAlO}_3:\text{Eu}^{3+}$  phosphor is excited at 395 nm and 466 nm; corresponding emission spectrum is shown in Fig. 4. Emission spectrum consists of two characteristics peaks located at 593 nm and 614 nm. The emission band of  $\text{Eu}^{3+}$  ions in  $\text{LaAlO}_3$  shows the emission at 593 nm (orange) and 614 nm (red). The emission peaks observed at 593 nm and 614 nm corresponds to the magnetic dipole ( ${}^5\text{D}_0 \rightarrow {}^7\text{F}_1$ ) and electric dipole ( ${}^5\text{D}_0 \rightarrow {}^7\text{F}_2$ ) transitions, respectively [22, 23]. As it can be seen, the highest intensity was found to be stronger in magnetic dipole transition than that of the electric dipole transition. It implies that  $\text{Eu}^{3+}$  has a symmetric environment, which means that more  $\text{Eu}^{3+}$  ions seized the  $\text{La}^{3+}$  lattice sites and lesser  $\text{Eu}^{3+}$  ions seized

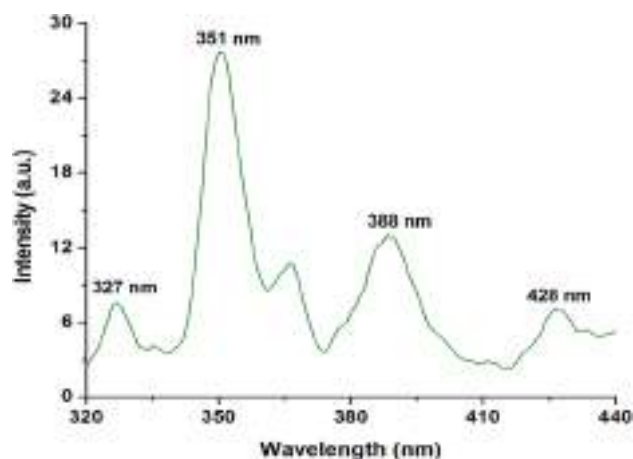


Fig. 5 Excitation spectrum of  $\text{LaAlO}_3:\text{Dy}^{3+}$  phosphor ( $\lambda_{\text{em.}}=484$  nm)

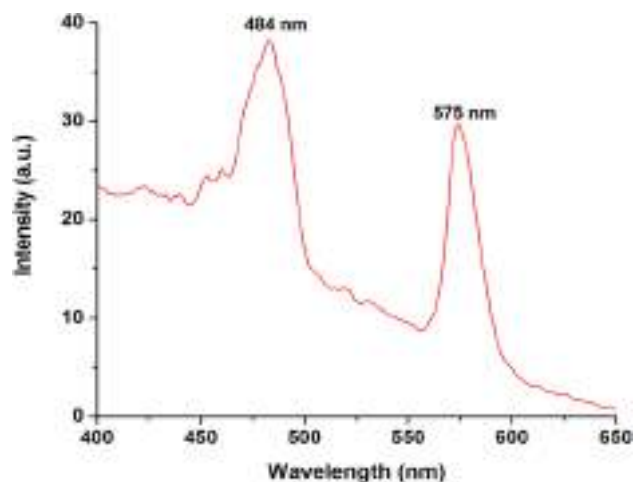
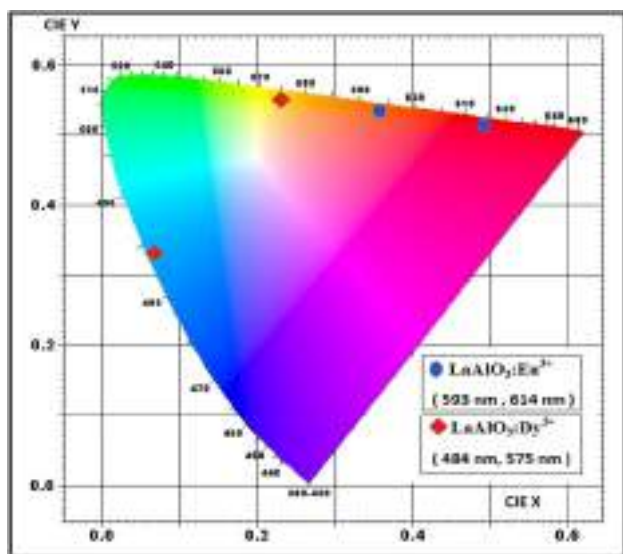


Fig. 6 Excitation spectrum of  $\text{LaAlO}_3:\text{Dy}^{3+}$  phosphor ( $\lambda_{\text{ex.}}=351$  nm)

the grain boundary or defect lattice. The larger excitation wavelength has no effect on the peak position, however, peak intensity found to be considerably increased.

### 3.4 Photoluminescence properties of $\text{LaAlO}_3:\text{Dy}^{3+}$ phosphor

Figure 5 shows the excitation spectra of  $\text{LaAlO}_3:\text{Dy}^{3+}$  phosphor monitored at 484 nm emission wavelength. Excitation spectrum consists of series of lines peaking at 327 nm, 351 nm, 388 nm and 428 nm. Strongest excitation peak observed at 351 nm. The luminescence emission shows the characteristic peaks associated with the trivalent Dy ion's inter-electronic energy-level transitions. Figure 6 shows the PL emission spectra of  $\text{LaAlO}_3:\text{Dy}^{3+}$  phosphor. The emission band of  $\text{Dy}^{3+}$  ions in  $\text{LaAlO}_3$  shows the emission at 484 nm (blue) and 575 nm (yellow). The peaks at 484 nm and 575 nm correspond to magnetic dipole transitions



**Fig. 7** CIE chromatic diagram of  $\text{LaAlO}_3:\text{Eu}^{3+}$  and  $\text{LaAlO}_3:\text{Dy}^{3+}$  phosphors

$^4\text{F}_{9/2} \rightarrow ^6\text{H}_{15/2}$  and electric dipole transitions  $^4\text{F}_{9/2} \rightarrow ^6\text{H}_{13/2}$  of  $\text{Dy}^{3+}$ , respectively [24–26].

### 3.5 Chromatic properties of $\text{LaAlO}_3:\text{Eu}^{3+}$ and $\text{LaAlO}_3:\text{Dy}^{3+}$ phosphors

Figure 7 shows CIE chromatic diagram of  $\text{LaAlO}_3:\text{Eu}^{3+}$  and  $\text{LaAlO}_3:\text{Dy}^{3+}$  phosphors. The CIE color coordinates of the  $\text{LaAlO}_3:\text{Eu}^{3+}$  phosphors of wavelength 593 nm is ( $X=0.592$ ,  $Y=0.407$ ) and of wavelength 614 nm is ( $X=0.677$ ,  $Y=0.322$ ). The CIE color coordinates of the  $\text{LaAlO}_3:\text{Dy}^{3+}$  phosphor of wavelength 484 nm is ( $X=0.073$ ,  $Y=0.185$ ) and of wavelength 575 nm is ( $X=0.478$ ,  $Y=0.520$ ). All the color co-ordinates are situated at the edge of chromaticity diagram indicating high color purity [5, 27].

## 4 Conclusions

Rare earth  $\text{Dy}^{3+}$  and  $\text{Eu}^{3+}$ -activated  $\text{LaAlO}_3$  phosphors were prepared by wet chemical method. X-ray diffraction pattern confirms the phase purity of  $\text{LaAlO}_3$  phosphor. SEM morphology shows porous irregular agglomerated structures with particle size in micro-meter range.  $\text{LaAlO}_3:\text{Eu}^{3+}$  phosphor gives emission at 593 nm and 614 nm upon excitation with 395 nm and 466 nm.  $\text{LaAlO}_3:\text{Dy}^{3+}$  phosphor exhibit emission at 484 nm and 575 nm under excitation of

351 nm. The calculated color coordinates are situated at the edge indicating high-color purity. Both the excitations are mercury-free excitation, therefore, prepared phosphor might be applicable in solid-state lighting.

## References

1. Y. Guo, B.K. Moon, B.C. Choi, J.H. Jeong, J.H. Kim, *Mater. Res. Bull.* **88**, 166 (2017)
2. D.N. Game, N.B. Ingale, S.K. Omanwar, *Optik* **127**, 6204 (2016)
3. C.Y. Lin, S.H. Yang, J.L. Lin, C.F. Yang, *Appl. Sci.* **7**, 30 (2017)
4. S. Ashwini, S.C. Prashantha, R. Naik, H. Nagabhushana, *J. Rare Earths* **18**, 278 (2018)
5. S.J. Dhoble, B.P. Kore, A.N. Yerpude, R.L. Kohale, P.W. Yawalkar, N.S. Dhoble, *Optik* **126**, 1527 (2015)
6. A.N. Yerpude, S.J. Dhoble, *J. Lumin.* **132**, 1781 (2012)
7. A.N. Yerpude, S.J. Dhoble, *Micro Nano Lett.* **7**, 268 (2012)
8. A.N. Yerpude, V.R. Panse, S.J. Dhoble, N.S. Kokode, M. Srinivas, *Luminescence* **32**, 1361 (2017)
9. A.N. Yerpude, G.N. Nikhare, S.J. Dhoble, N.S. Kokode, *Mater. Today Proc.* **15**, 511 (2019)
10. D.A. Hakeema, J.W. Pia, G.W. Junga, S.W. Kimb, K. Park, *Dyes Pigm.* **160**, 234 (2019)
11. X. Liu, Z. Song, Y. Kong, S. Wang, S. Zhang, Z. Xia, Q. Liu, *J. Alloys Compd.* **770**, 1069 (2019)
12. B.P. Kore, S. Tamboli, N.S. Dhoble, A.K. Sinh, M.N. Singh, S.J. Dhoble, H.C. Swart, *Mater. Chem. Phys.* **187**, 233 (2017)
13. K. Li, R.V. Deun, *Dyes Pigments* **155**, 258 (2018)
14. T. Fan, J. Lu, F. Lin, Z. Zhou, *IOP Publ. Mater. Res. Express* **3**, 045010 (2016)
15. L.T. Melato, O.M. Ntwaeaborwa, R.E. Kroon, T.E. Motaung, S.V. Motloung, *J. Mol. Struct.* **1176**, 217 (2019)
16. B.C. Jamalalah, M. Jayasimhadri, *J. Mol. Struct.* **1178**, 394 (2019)
17. M.A. Bednarkiewicz, E.M. Mendoza, A.F. Fuentes, L. Kepinski, *J. Solid State Chem.* **194**, 264 (2012)
18. A.M. Hernández, M.A. Alfaro, A.B. Villatoro, C. Falcony, T.R. Montalvo, J.Z. Medina, *Open J. Synth. Theory Appl.* **6**, 1 (2017)
19. Z. Mao, D. Wang, Q. Lu, W. Yu, Z. Yuan, *Chem. Commun.* **3**, 346 (2009)
20. W. Qiang, H.Y. Ping, D. Ning, Z.B. Suo, *Sci China B* **52**, 1104 (2009)
21. X. Jin, L. Zhang, H. Luo, X. Fan, L. Jin, B. Liu, D. Li, Z. Qiu, Y. Gan, *Integr. Ferroelectr.* **188**, 1 (2018)
22. Y. Jiao, X. Wu, Q. Ren, O. Hai, F. Lin, W. Bai, *Opt. Laser Technol.* **109**, 470 (2019)
23. D. Xiang, Y. Chua, X. Xiaoc, J. Xua, Z. Zhanga, Z. Liua, Y. Zhanga, B. Yanga, *J. Solid State Chem.* **268**, 130 (2018)
24. A.N. Yerpude, S.J. Dhoble, N.S. Kokode, *Optik* **179**, 774 (2019)
25. N. Baig, N.S. Dhoble, A.N. Yerpude, V. Singh, S.J. Dhoble, *Optik* **127**, 6574 (2016)
26. A.N. Yerpude, S.J. Dhoble, *J. Lumin.* **132**, 2975 (2012)
27. R.L. Kohale, S.J. Dhoble, *J. Lumin.* **138**, 153 (2013)

**Publisher's Note** Springer Nature remains neutral with regard to jurisdictional claims in published maps and institutional affiliations.

# Synthesis of Dy<sup>3+</sup>, Eu<sup>3+</sup> and Tb<sup>3+</sup> Activated Y<sub>2</sub>O<sub>2</sub>S Optoelectronic Phosphors for N-UV LED Applications



V. V. Shinde, S. J. Dhoble

**Abstract:** In this, a series of iso-structural Y<sub>2</sub>O<sub>2</sub>S (RE<sup>3+</sup> = Dy<sup>3+</sup>, Eu<sup>3+</sup> and Tb<sup>3+</sup>) phosphors were synthesized by high temperature solid state reaction method. All the phosphors exhibit strong line and broad excitation in the near ultraviolet (n-UV) region. Bright color emission in blue, green and red color region of electromagnetic hue cycle was noticed. The concentration of activator doped was optimized from the photoluminescence (PL) study. The quenching in luminescence intensity after particular concentration of dopant is discussed here. Y<sub>2</sub>O<sub>2</sub>S phosphor doped with Dy<sup>3+</sup> displays useful blue and yellow emission bands at 487nm and 574nm, when stimulated by 388nm excitation wavelength. Y<sub>2</sub>O<sub>2</sub>S:Eu<sup>3+</sup> phosphor displays an orange and red emission at 594nm and 620nm, when stimulated at 396 nm. Whereas, Y<sub>2</sub>O<sub>2</sub>S:Tb<sup>3+</sup> phosphor displays weak blue radiation in the range 485nm and strong green radiation at 545nm, when stimulated at 305 nm.

The excitation spectra used for the Y<sub>2</sub>O<sub>2</sub>S:RE<sup>3+</sup> (RE<sup>3+</sup> = Dy<sup>3+</sup>, Eu<sup>3+</sup> and Tb<sup>3+</sup>) phosphor is in the near ultraviolet (n-UV) region spanning from 300 nm to 400 nm, which is a peculiarity of near ultraviolet stimulated LED. The outcome of the RE<sup>3+</sup> (RE<sup>3+</sup> = Dy<sup>3+</sup>, Eu<sup>3+</sup> and Tb<sup>3+</sup>) absorption on the luminescence properties of Y<sub>2</sub>O<sub>2</sub>S:RE<sup>3+</sup> phosphors was also studied.

**Keywords:** Oxy-sulphide, phosphor, lamp phosphor, light emitting diode, Rare earth.

## I. INTRODUCTION

Light emitting diode (LED) industrial science is reaching towards fully developed stage by replacing the old technology of fluorescent lamps. During the last 20 years, improvements in phosphors have opened the new gateways for white LEDs, in which numerous wavelengths mix together to simulate the solar chromatic spectrum. There are two major approaches for achieving white light from LEDs. The first approach is to blend the light from particular electrically driven LEDs that radiate the primary colors, i.e., red, green and blue. The inadequacy of getting highly efficient green LEDs restricts the use of this approach to the generation of white light.

**Revised Manuscript Received on February 28, 2020.**

\* Correspondence Author

V. V. Shinde, Department of Electronics, Bajaj College of Science, Wardha, India, +91 9423118599, (email:vvshinde.wda@gmail.com)

S. J. Dhoble\*, Department of Physics, RTM Nagpur University, Nagpur-440033, India, +91 9822710204, (email:sjdhoble@rediffmail.com)

© The Authors. Published by Blue Eyes Intelligence Engineering and Sciences Publication (BEIESP). This is an [open access](http://creativecommons.org/licenses/by-nc-nd/4.0/) article under the CC-BY-NC-ND license <http://creativecommons.org/licenses/by-nc-nd/4.0/>

In second approach the blue or UV emitting LEDs coated with a color converting phosphors which leads to the emission of white light. Majority of the research efforts on solid-state lighting (SSL) has focused on the development of light emitter and light extraction mechanisms to meet general illumination application requirements [1, 2].

The Y<sub>2</sub>O<sub>2</sub>S host is a prominent large band-gap (4.6-4.8eV) semiconductor [3]. The Y<sub>2</sub>O<sub>2</sub>S do not exist as usual mineral but was devised, firstly, as a host matrix for RE<sup>3+</sup> ions by Royce [4] and Yocom [5] in 1968. Since then this lattice has been subject of intensive research interest and utilized as a potential luminescence material for various application in lighting technology and display as a host. Y<sub>2</sub>O<sub>2</sub>S:Tb is known to be a X-ray phosphor used in practical X-ray display screens as well as a green phosphor for CRT displays. Y<sub>2</sub>O<sub>2</sub>S:Eu is one of the most crucial red-emitting phosphors used in industry. Some of the important applications of Y<sub>2</sub>O<sub>2</sub>S:Eu phosphor are in cathode-ray tubes (CRTs) and field emission displays (FEDs) [6-9]. The present investigations of rare earth doped Y<sub>2</sub>O<sub>2</sub>S phosphors into the visible emissions under near ultraviolet stimulation (excitation) were undertaken to examine the mechanism of emission process. The main aim of this study is to develop this phosphor and improve the PL properties for lighting applications when excited in the n-UV (near ultraviolet) region. In the present study we have used near ultraviolet excitation wavelength, as this range of excitation wavelength comes in the same region for the white LED excitation.

## II. EXPERIMENTAL METHOD

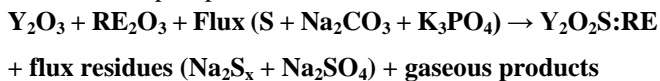
In the present work, Y<sub>2</sub>O<sub>2</sub>S:RE<sup>3+</sup> (RE<sup>3+</sup> =, Dy<sup>3+</sup>, Eu<sup>3+</sup> and Tb<sup>3+</sup>) phosphors were synthesized by solid flux fusion reaction method. The starting materials used were yttrium oxide (Y<sub>2</sub>O<sub>3</sub>), sulphur powder (S), Sodium carbonate (Na<sub>2</sub>CO<sub>3</sub>), tri-potassium Phosphate (K<sub>3</sub>PO<sub>4</sub>) as fluxes. Different flux materials such as sodium carbonate (Na<sub>2</sub>CO<sub>3</sub>) and tri-potassium phosphate (K<sub>3</sub>PO<sub>4</sub>) are used to increase the rate of reaction and lower down the reaction temperature. These raw materials have melting point below the melting temperature of Y<sub>2</sub>O<sub>2</sub>S material. These fluxes dissolve partially and remain inactive in the solid state reaction. During synthesis, the quantity of flux used was 20 weight % for K<sub>3</sub>PO<sub>4</sub> and 30 to 50 weight % for both sulphur powder and Na<sub>2</sub>CO<sub>3</sub>, of the total weight.



# Synthesis of Dy<sup>3+</sup>, Eu<sup>3+</sup> and Tb<sup>3+</sup> Activated Y<sub>2</sub>O<sub>2</sub>S Optoelectronic Phosphors for N-UV LED Applications

The rare earth dopants used were ammonium hexanitratocerate (NH<sub>4</sub>)<sub>2</sub>Ce(NO<sub>3</sub>)<sub>6</sub>, dysprosium oxide (Dy<sub>2</sub>O<sub>3</sub>), Europium oxide (Eu<sub>2</sub>O<sub>3</sub>) and terbium oxide (Tb<sub>2</sub>O<sub>3</sub>).

In this synthesis the stoichiometric quantities of raw materials were weighted and mixed in homogeneous form by crushing mechanically for 1 hour in mortar pastel. These crushed powders were preheated in a muffle furnace at around 100<sup>o</sup>C and then again crushed all these samples and placed in muffle furnace for annealing at 1150<sup>o</sup>C for 10 hours. After that prepared samples were taken out from the furnace and washed with distilled water several times then finally washed with diluted HCl acid. The prepared samples were again placed in for drying then crushed in mortar pastel [10]. The preparation of Y<sub>2</sub>O<sub>2</sub>S:RE phosphor follows the chemical reaction:



The phase purity and crystallinity of prepared host lattice Y<sub>2</sub>O<sub>2</sub>S was characterized by X-ray powder diffraction method using Cu K $\alpha$  radiation. The particle size and morphological behaviour of synthesized powder were analyzed by scanning electron microscope (SEM). Bruker Fourier transform infrared spectrometer was used to record infrared spectra. The spectroscopic properties of synthesized phosphors were measured at room temperature by using Shimadzu make RF5301PC spectro-fluorometer. At measurement time slit width of the instrument was fixed at 1.5nm. The co-ordinations in the xy-chromaticity diagram are directly calculated from the fluorescent spectra (CIE 1931) [11].

## III. RESULTS AND DISCUSSION

### A. X-ray Diffraction (XRD)

Figure 1 shows XRD pattern of synthesized Y<sub>2</sub>O<sub>2</sub>S phosphor. It is found that diffraction peaks of the phosphor are in well accordance with the standard ICDD File No. 24-1424. The XRD diffraction pattern of prepared Y<sub>2</sub>O<sub>2</sub>S host did not indicate presence of any constituent and other likely phases. All the diffraction peaks were evidence of the high purity and crystallinity of Y<sub>2</sub>O<sub>2</sub>S.

The sample was found to be non-hygroscopic, stable and whitish in nature. The diffraction pattern acknowledges that the Y<sub>2</sub>O<sub>2</sub>S phosphor was prepared without any impurity and it confirms Y<sub>2</sub>O<sub>2</sub>S phosphor were successfully prepared in the homogeneous form.

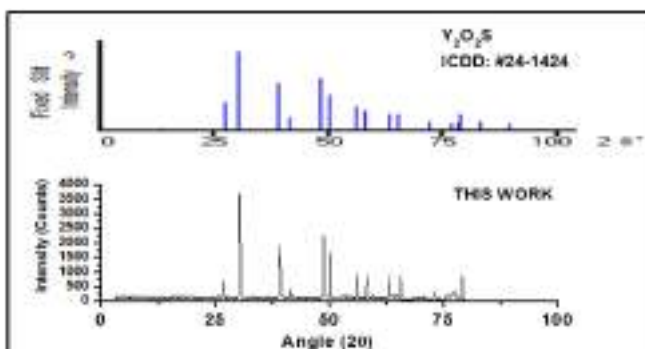


Figure 1: XRD pattern of pure Y<sub>2</sub>O<sub>2</sub>S.

### B. Surface Morphology

Figure 2 shows the SEM micrograph of Y<sub>2</sub>O<sub>2</sub>S powders. During annealing at high temperature, the crystallites come closer and form an agglomerated structure which is consist of small sintered clusters. The morphology of the Y<sub>2</sub>O<sub>2</sub>S powders found to be irregular in shape and the grain size is significantly varying. The approximate particle size ranges from 1 to 5  $\mu$ m. The particle size strongly depends on the type of synthesis method and synthesis conditions. Phosphors synthesized by solid state method generally have particle size within this range.

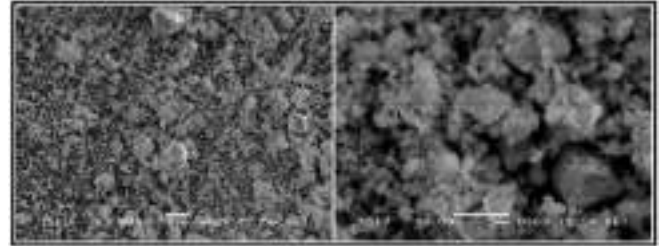


Figure 2: SEM image of synthesized Y<sub>2</sub>O<sub>2</sub>S.

### C. Crystal Structure

Schematic crystal structure of Y<sub>2</sub>O<sub>2</sub>S is shown in figure 3. The Y<sub>2</sub>O<sub>2</sub>S lattice has trigonal crystal symmetry with P3m1 space group. The Y<sub>2</sub>O<sub>2</sub>S lattice found to be A-type rare-earth oxide structure, and analyzed that the one of the three oxygen sites is occupied by a sulphur atom. Figure clearly illustrate that the every metal ions bonded with four oxygen atoms and three sulphur atoms. In presented crystal structure investigation found to form a seven coordinated geometry with the oxygen and the metal in the same plane. The Y<sub>2</sub>O<sub>2</sub>S crystal structure shows Ln and oxygen atoms have the same site symmetry of C<sub>3v</sub> and the S site has symmetry of D<sub>3d</sub>[10].

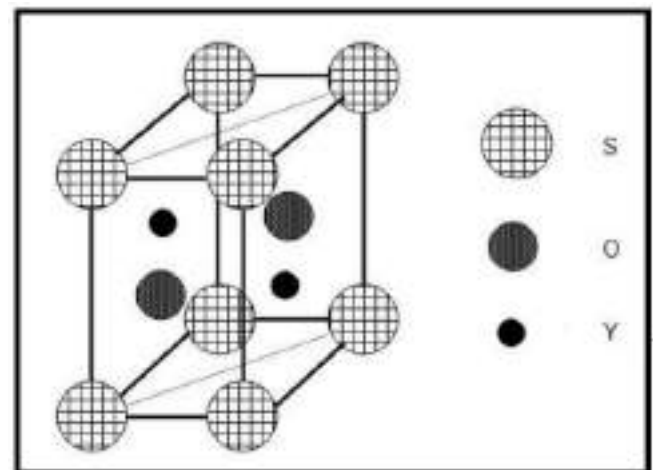


Figure 3: Schematic crystal structure of Y<sub>2</sub>O<sub>2</sub>S.

### D. FT-IR Analysis

FT-IR is the characterization tool which gives information about the vibrations of bonds present in prepared host. FT-IR spectroscopy gives the information about molecules frequencies, their vibrations and stretching corresponding to distinct energy levels.

An obtained spectrogram provides valuable knowledge about type of bonding present in the sample, the strength of the bonding and bonding percentage present in the sample. Fourier transform infrared spectrometer was used for measurement of FT-IR spectra of the pure  $Y_2O_2S$  phosphor. The spectrum was measured in the range of 500 to 4000  $cm^{-1}$ . Figure 4 shows the FTIR spectrum of  $Y_2O_2S$ .

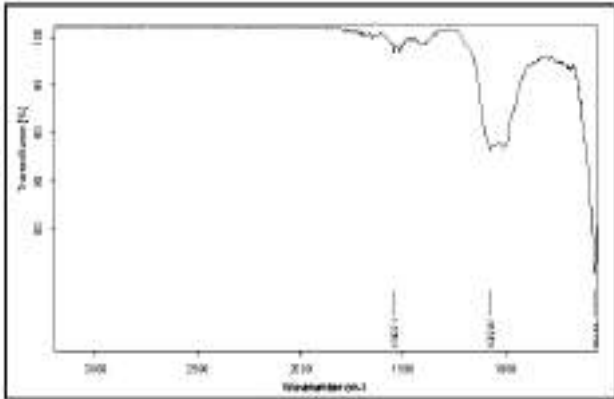


Figure 4: FT-IR spectrum of  $Y_2O_2S$  phosphor.

In this no absorption deep was observed around 3500  $cm^{-1}$  which suggest complete removal of O-H molecules from the sample after annealing. The absorption deep of cubic phase of  $Y_2O_2S$  appears at 561  $cm^{-1}$ . Strong deeps at 1540 and 1072  $cm^{-1}$  were due to Y-O symmetric stretching mode. The stretching modes due Y-S and S-O bonding were not witnessed in the FTIR spectrum [10, 11].

#### E. PL Emission Of $RE^{3+}$ In $Y_2O_2S$ ( $RE^{3+} = Dy^{3+}, Eu^{3+}$ and $Tb^{3+}$ )

Photoluminescence studies of  $RE^{3+}$  ( $RE^{3+} = Dy^{3+}, Eu^{3+}$  or  $Tb^{3+}$ ) doped  $Y_2O_2S$  oxy-sulphides phosphors are investigated here. This work gives the optimum quantity of activator required for getting maximum lighting efficiency and light emission of dopant in particular region.

##### i) PL Emission Of $Dy^{3+}$ In $Y_2O_2S$

The excitation spectra of  $Y_2O_2S:2mol\%Dy^{3+}$  phosphor was recorded under 574 nm emission wavelengths as shown in figure 5. The excitation spectrum consists of several peaks varying from 220 nm to 450 nm. The excitation peaks in the range 275 to 450nm, which are ascribed due to f-f transition of the  $Dy^{3+}$  ion. The prominent excitation peaks recorded at 351 nm, 368 nm and 388 nm, which are due observed due to the  ${}^6H_{15/2} \rightarrow {}^6P_{7/2}$ ,  ${}^6H_{15/2} \rightarrow {}^6P_{5/2}$ , and  ${}^6H_{15/2} \rightarrow {}^6I_{13/2}$  transitions  $Dy^{3+}$  ion, respectively[12,13].

The excitation spectra for  $Y_2O_2S:Dy^{3+}$  phosphor has three prominent peaks in the near UV region at 351nm, 368nm and 388nm. The PL emission of  $Y_2O_2S:Dy^{3+}$  phosphor for all these excitations is shown in figure 6. The excitation peak shows highest intensity at 351nm compared to other peaks. The excitation spectra shows highest intensity at 351nm wavelength but 388nm excitation peak is more promising for solid state lighting because it is well matched with UV excitation range [14].

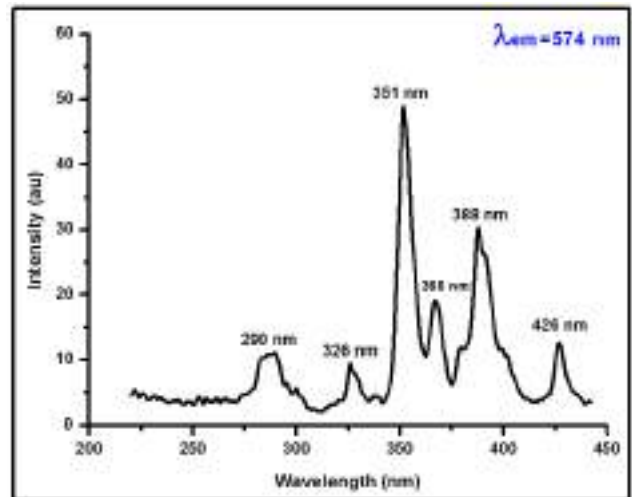


Figure 5: Excitation spectrum of  $Y_2O_2S:Dy^{3+}$  phosphor.

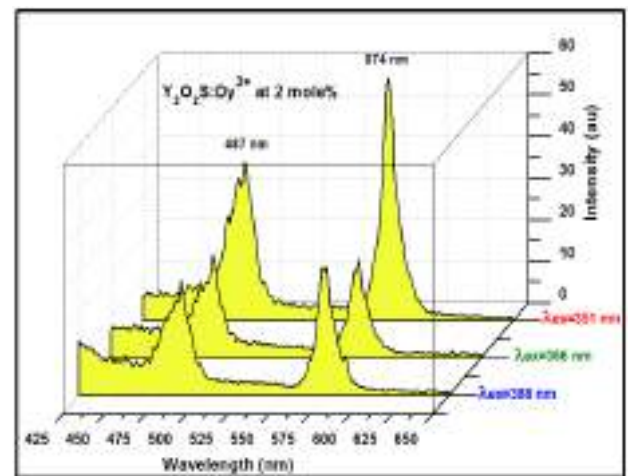


Figure 6: Emission spectra of  $Y_2O_2S:Dy^{3+}$  phosphor at 2 mole% for various excitation wavelengths.

Under 388nm excitation, the emission spectrum was recorded for  $Y_2O_2S:Dy^{3+}$ , phosphors as shown in the figure 7. The PL emission spectrum shows two prominent emission peaks at blue (487nm) and yellow (574nm) regions, which are ascribed due to the  ${}^4F_{9/2} \rightarrow {}^6H_{15/2}$  and  ${}^4F_{9/2} \rightarrow {}^6H_{13/2}$  electronic transitions of  $Dy^{3+}$  ions, respectively [15]. According to available literature,  ${}^4F_{9/2} \rightarrow {}^6H_{15/2}$  (487nm) and  ${}^4F_{9/2} \rightarrow {}^6H_{13/2}$  (574nm) transition occurred due to magnetic dipole transition and hypersensitive (forced dipole) transition, respectively.

The optical properties of the material are often affected by the structure of the matrix and synthesis technique [16]. According to literature it is well known that  ${}^4F_{9/2} \rightarrow {}^6H_{15/2}$  (magnetic dipole transition) occurred because of insensitivity to the crystal field around the  $Dy^{3+}$  ions and  ${}^4F_{9/2} \rightarrow {}^6H_{13/2}$  (hyper sensitive transition) occurred because of strongly influenced by the outside environment surrounding of  $Dy^{3+}$ . When the  ${}^4F_{9/2} \rightarrow {}^6H_{15/2}$  transition is stronger than the  ${}^4F_{9/2} \rightarrow {}^6H_{13/2}$  transition then  $Dy^{3+}$  is located at a low symmetry site (without inversion symmetry) [10, 17]. Thus, from emission spectra shown in figure 7, it can be concluded that  $Dy^{3+}$  has occupied low symmetry site that too without inversion symmetry.

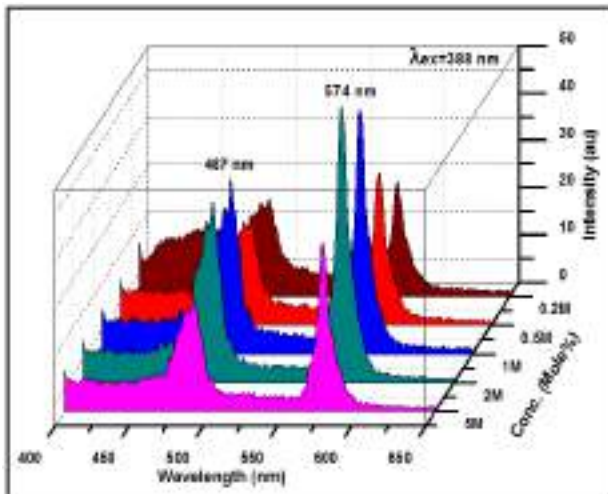


Figure 7: Emission spectra of Y<sub>2</sub>O<sub>2</sub>S:Dy<sup>3+</sup> phosphor.

Photoluminescence properties of a phosphor is fully depends on the concentration of dopants [18]. It is well known that the pattern of emission peak does not change with doping of rare earth ions, only the emission intensity vary with increasing the concentration of rare earth ions [19]. Fig. 7 shows that when concentration of Dy<sup>3+</sup> increases then PL emission intensity increased up to 2mol%. PL emission spectrum shows maximum value of intensity at 2mole % and then decreases with an increase of dopant concentration due to concentration quenching. This happens when the concentration of Dy<sup>3+</sup> increases continuously which increases the interaction among Dy<sup>3+</sup> ions. The interaction between Dy<sup>3+</sup> ions is such that they transfer energy to nearest Dy<sup>3+</sup> ion through non-radiative transfer. With increase in Dy concentration the probability of non-radiative energy transfer increases which leads to further decrease in emission intensity. In the process of cross relaxation among two dopants, the excitation energy from an ion decaying from an excited state stimulates a nearby ion from the ground state to the metastable level. In case of Dy<sup>3+</sup> the energy of the (<sup>4</sup>F<sub>9/2</sub> → <sup>6</sup>H<sub>11/2</sub> + <sup>6</sup>H<sub>9/2</sub>) transition matches that of the (<sup>6</sup>H<sub>15/2</sub> → <sup>6</sup>F<sub>11/2</sub> + <sup>6</sup>H<sub>9/2</sub>) transition. In the present work, concentration quenching occurred due to cross relaxation process i.e. energy transfers from one Dy<sup>3+</sup> to another neighboring Dy<sup>3+</sup> [20]. The 300 to 400 nm is Hg free excitation and it is very important for solid state lighting phosphors. All these outcomes shows our synthesized Y<sub>2</sub>O<sub>2</sub>S:Dy<sup>3+</sup> phosphors have potential application in field of solid state lighting devices as well as in white LED.

ii) PL Emission Of Eu<sup>3+</sup> In Y<sub>2</sub>O<sub>2</sub>S

The excitation spectra of Y<sub>2</sub>O<sub>2</sub>S:Eu<sup>3+</sup> phosphor monitored at 594 nm emission wavelength is shown in figure 8. The excitation spectra observed in the range of 200nm to 500nm. In this range we have observed charge transfer band at 255nm and several narrow excitation peaks in the range of 350nm and 400nm are due to the typical f-f transition of Eu<sup>3+</sup>. The strongest excitation peaks observed at 396 nm and 468nm, which are ascribed due to <sup>7</sup>F<sub>0</sub>→<sup>5</sup>L<sub>6</sub> and <sup>7</sup>F<sub>0</sub>→<sup>5</sup>D<sub>2</sub> transitions of Eu<sup>3+</sup> ions, respectively [21]. Besides this, due to the charge transfer band (Eu<sup>3+</sup>→O<sup>2-</sup>) broad excitation peak at 255 nm is also observed.

Figure 9 and 10 show the emission spectra of Y<sub>2</sub>O<sub>2</sub>S:Eu<sup>3+</sup> phosphors excited by 396 nm and 468 nm wavelengths, respectively. The Y<sub>2</sub>O<sub>2</sub>S:Eu<sup>3+</sup> phosphor when excited by λ<sub>ex</sub>=396 nm and λ<sub>ex</sub>=468 nm shows prominent emission peaks at 594 nm, 620 nm 589 nm and 613 nm respectively. The characteristic emission peaks in region of Eu<sup>3+</sup>. A strong red emission of Eu<sup>3+</sup> in the region 610 to 620 nm was due to the <sup>5</sup>D<sub>0</sub>→<sup>7</sup>F<sub>2</sub> transition and emission in the region 589 to 596 nm was due to <sup>5</sup>D<sub>0</sub>→<sup>7</sup>F<sub>1</sub> transition. It is observed that at λ<sub>ex</sub>=396, 594 nm (<sup>5</sup>D<sub>0</sub>→<sup>7</sup>F<sub>1</sub>) emission is dominant compared to 620 nm (<sup>5</sup>D<sub>0</sub>→<sup>7</sup>F<sub>2</sub>) whereas at λ<sub>ex</sub>=468 nm, 613 nm (<sup>5</sup>D<sub>0</sub>→<sup>7</sup>F<sub>2</sub>) emission is dominant compared to 589 nm (<sup>5</sup>D<sub>0</sub>→<sup>7</sup>F<sub>1</sub>) emission [22, 23].

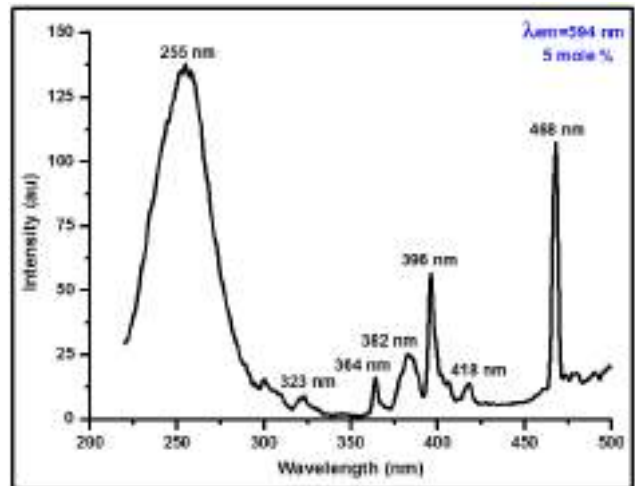


Figure 8: Excitation spectrum of Y<sub>2</sub>O<sub>2</sub>S:Eu<sup>3+</sup> phosphor.

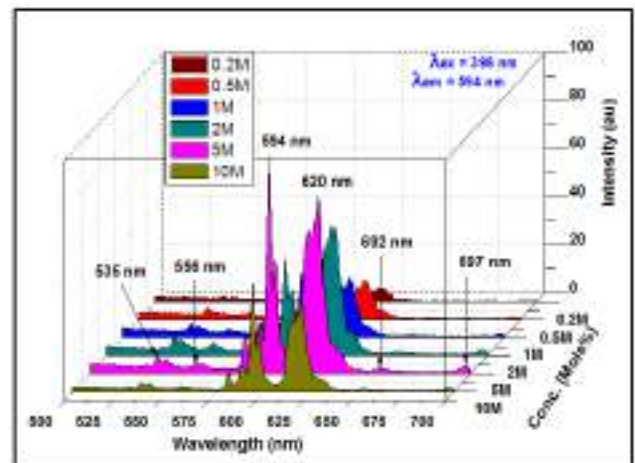


Figure 9: Emission spectra of Y<sub>2</sub>O<sub>2</sub>S:Eu<sup>3+</sup> phosphor at λ<sub>ex</sub>=396 nm.

580 to 640 nm corresponds to intra 4f shell transitions of <sup>5</sup>D<sub>0</sub>→<sup>7</sup>F<sub>J</sub> (J=0, 1, 2, 3, 4) of The emission spectra of Eu<sup>3+</sup> particle is marginally impacted by encompassing ligands of the host material because the transition of Eu<sup>3+</sup> include just a redistribution of electrons inside the internal 4f subshells. A less transitions are delicate to the environment and turn out to be increasingly extreme and such advances are known as hypersensitive transitions. For Y<sub>2</sub>O<sub>2</sub>S:Eu<sup>3+</sup> phosphor the emission in the range 610 - 620 nm is because of <sup>5</sup>D<sub>0</sub>→<sup>7</sup>F<sub>2</sub> is electric dipole transition and considered as hypersensitive transition.



In the present work, prepared material gives bright emission because its transition obey the selection rule  $\Delta J=2$ . The orange emission observed in the range of 590 to 596 nm is because of  ${}^5D_0 \rightarrow {}^7F_1$  transition, with the selection rule  $\Delta J=1$  is a magnetic-dipole transition. According to literature, inversion symmetry occurred in  $\text{Eu}^{3+}$  when  ${}^5D_0 \rightarrow {}^7F_1$  transition is dominant. On the contrary, if  $\text{Eu}^{3+}$  does not occupy the inversion symmetry site, the  ${}^5D_0 \rightarrow {}^7F_2$  transition is dominant. The luminescence property of material depends on the concentration of the dopants. In the present study, when concentration of  $\text{Eu}^{3+}$  ions increased then the distance between  $\text{Eu}^{3+}$  ions becomes less and this results in the migration of excitation energy among  $\text{Eu}^{3+}$  ions leading to quenching of the emission. The maximum emission intensity is observed at 5mol% of  $\text{Eu}^{3+}$  concentration and decreases with further increase in concentration of  $\text{Eu}^{3+}$  ions [10].

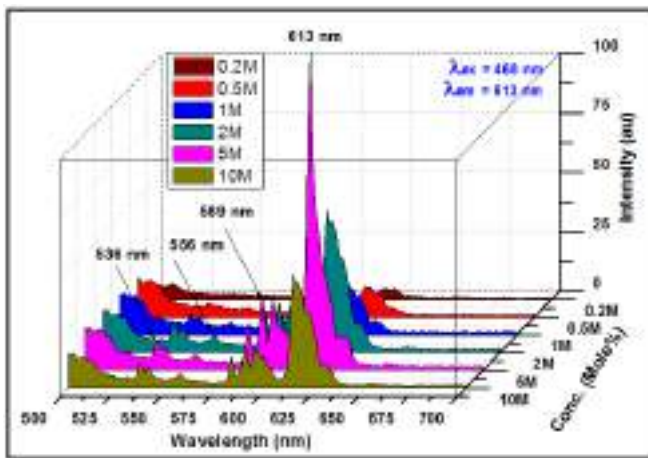


Figure 10: Emission spectra of  $\text{Y}_2\text{O}_2\text{S}:\text{Eu}^{3+}$  phosphor at  $\lambda_{\text{ex}}=468$  nm.

### iii) PL Emission Of $\text{Tb}^{3+}$ In $\text{Y}_2\text{O}_2\text{S}$

Figure 11 show the excitation spectra of  $\text{Y}_2\text{O}_2\text{S}:\text{Tb}^{3+}$  phosphor in the 220–500 nm range, monitored at 545 nm emission wavelength. The overall excitation spectrum of  $\text{Tb}^{3+}$  can be divided into two parts. First part is in the wavelength range from 220-320 nm comprising of  $4f^8 \rightarrow 4f^7 5d^1$  transitions and other part of the excitation spectrum in the wavelength range 320–500 nm which is due to  $4f^8 \rightarrow 4f^8$  transitions of the  $\text{Tb}^{3+}$  ions [24].

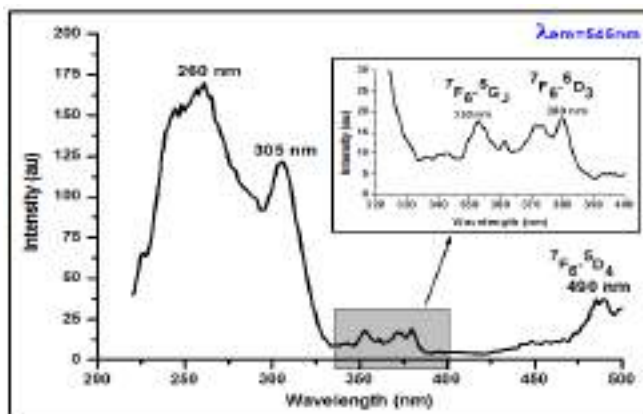


Figure 11: Excitation spectrum of  $\text{Y}_2\text{O}_2\text{S}:\text{Tb}^{3+}$  phosphor.

There are several excitation peaks in the 320 to 400 nm region corresponding to transitions between  ${}^7F_6$  and the

various excited states belonging to the  $4f^8$  electronic configuration of  $\text{Tb}^{3+}$  ions. The excitation peaks at 352 nm ( ${}^7F_6 \rightarrow {}^5L_6$ ) and 380 nm ( ${}^7F_6 \rightarrow {}^5G_6$ ) were due to forbidden  $4f-4f$  transition of  $\text{Tb}^{3+}$  ions. Though there were significant absorption at 260 nm for  $\text{Y}_2\text{O}_2\text{S}:\text{Tb}^{3+}$  we have chosen  $\lambda_{\text{ex}}=305$  nm as excitation for  $\text{Y}_2\text{O}_2\text{S}:\text{Tb}^{3+}$ , as it is more suitable for near UV excitation in white LED and therefore,  $\text{Y}_2\text{O}_2\text{S}:\text{Tb}^{3+}$  has potential to be used as near-UV LED phosphor. The emission spectra of  $\text{Y}_2\text{O}_2\text{S}:\text{Tb}^{3+}$  is determined by the transitions of electrons from an upper ( ${}^5D_3$ ) and a lower ( ${}^5D_4$ ) excited level to the multiple levels  ${}^7F_J$  ( $J = 0, 1, 2, 3, 4, 5, 6$ ) of the  $4f^8$  configuration. The emission of terbium doped phosphor is mainly in the green region due to the  ${}^5D_4 \rightarrow {}^7F_1$  transitions and the blue emission contributes to the emission from the higher level transitions  ${}^5D_3 \rightarrow {}^7F_J$  [25].

Figure 12 shows the emission spectra of  $\text{Y}_2\text{O}_2\text{S}:\text{Tb}^{3+}$  phosphors under the excitation wavelength of 305 nm. The emission peaks were found in the region 485-495, 545 and 580-600 nm, which were assigned to the  ${}^5D_4 \rightarrow {}^7F_J$  ( $J = 6, 5, 4$ ) transition of  $\text{Tb}^{3+}$  ions.

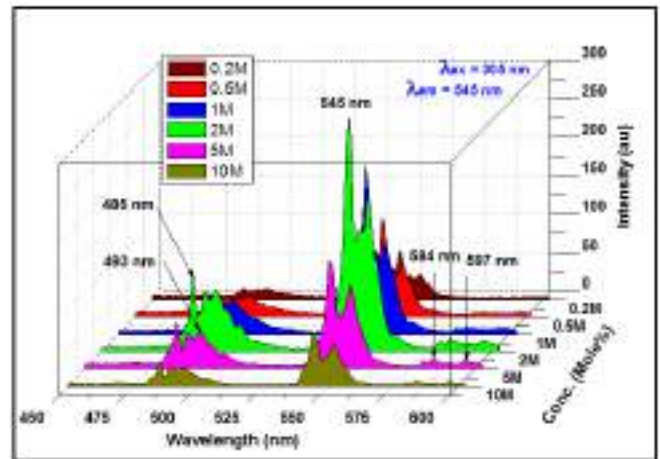


Figure 12: Emission spectra of  $\text{Y}_2\text{O}_2\text{S}:\text{Tb}^{3+}$  phosphor at  $\lambda_{\text{ex}}=305$  nm.

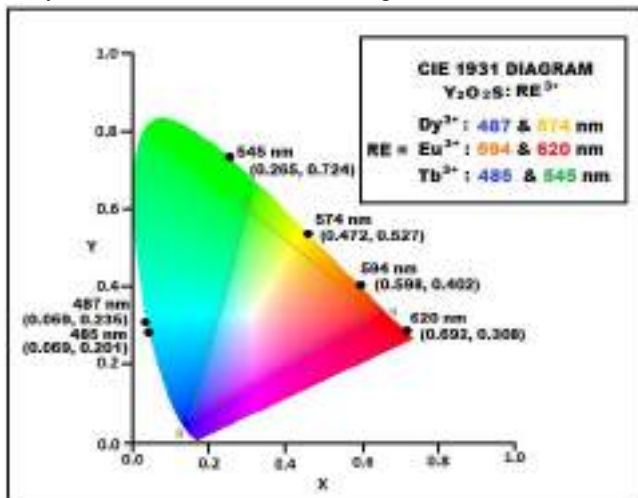
As expected, the spectral shift was not observed because the  $4f$  shell of  $\text{Tb}^{3+}$  was well shielded by  $5s$  and  $5p$  shells. Moreover, the emission from  ${}^5D_3 \rightarrow {}^7F_J$  level are quenched by the cross relaxation [ $\text{Tb}^{3+}({}^5D_3) + \text{Tb}^{3+}({}^7F_6) \rightarrow \text{Tb}^{3+}({}^5D_4) + \text{Tb}^{3+}({}^7F_1)$ ]. The cross relaxation process produces the rapid population of the  ${}^5D_4$  level at the expense of  ${}^5D_3$ , resulting in a strong emission from the  ${}^5D_4$  to the  ${}^7F_J$  level [26–27]. Generally, the cross relaxation is observed at higher  $\text{Tb}^{3+}$  concentration. The occurrence of PL emission quenching at higher concentration of  $\text{Tb}^{3+}$  was witnessed, which is due to the cross relaxation. This is in good agreement with the results reported in literature. The luminescent mechanism of phosphor is due to competition between the optical activation of  $\text{Tb}^{3+}$  ions which results in increase of PL intensity and the clustering of  $\text{Tb}^{3+}$  causes concentration quenching. At lower concentration of  $\text{Tb}^{3+}$ , the first mechanism is dominant in the luminescence process and the PL intensity increases with the increase in concentration of  $\text{Tb}^{3+}$  [28].

# Synthesis of Dy<sup>3+</sup>, Eu<sup>3+</sup> and Tb<sup>3+</sup> Activated Y<sub>2</sub>O<sub>2</sub>S Optoelectronic Phosphors for N-UV LED Applications

Figure 12 also shows the relative PL intensities of 545 nm under 305nm excitation for Y<sub>2</sub>O<sub>2</sub>S:Tb<sup>3+</sup> phosphors. Up to 2mol% concentration of Tb<sup>3+</sup> ion the PL intensity of 545 nm emission peak increases with increase of Tb<sup>3+</sup> ion concentration after that the PL intensity of 545 nm emissions decreases. As the concentration of Tb<sup>3+</sup> exceed the critical concentration, distance between Tb<sup>3+</sup> ions become shorter, which cause activator to form pairs and thus results in concentration quenching. The emission intensity reached its maximum value at about 2 mole% doping concentration in the Y<sub>2</sub>O<sub>2</sub>S:Tb<sup>3+</sup> phosphor [24].

## F. Chromatic Properties

The Commission International de l'Eclairage (CIE) 1931 diagram of the prepared Y<sub>2</sub>O<sub>2</sub>S:RE<sup>3+</sup> phosphor (Where RE<sup>3+</sup> = Dy<sup>3+</sup>, Eu<sup>3+</sup> or Tb<sup>3+</sup>) is shown in figure 13.



The chromatic co-ordinates (X, Y) are calculated using the color calculator radiant imaging software and are summarized  
**Figure 13: Chromatic graph of Y<sub>2</sub>O<sub>2</sub>S: RE<sup>3+</sup> phosphor (RE<sup>3+</sup> = Dy<sup>3+</sup>, Eu<sup>3+</sup> and Tb<sup>3+</sup>).**

**Table I: The (X, Y) chromatic co-ordinates for Y<sub>2</sub>O<sub>2</sub>S: RE<sup>3+</sup> phosphor (RE<sup>3+</sup> = Dy<sup>3+</sup>, Eu<sup>3+</sup> and Tb<sup>3+</sup>).**

Name of sample	Excitation (nm)	Emission (nm)	(X,Y) Coordinates	Color region
Y <sub>2</sub> O <sub>2</sub> S: Dy <sup>3+</sup>	388	487	(0.059, 0.235)	Blue
		574	(0.472, 0.527)	Yellow
Y <sub>2</sub> O <sub>2</sub> S: Eu <sup>3+</sup>	396	594	(0.598, 0.402)	Orange
		620	(0.692, 0.308)	Red
Y <sub>2</sub> O <sub>2</sub> S: Tb <sup>3+</sup>	305	485	(0.069, 0.201)	Blue
		545	(0.265, 0.724)	Green

## REFERENCES

- P. F.S. Pereira, M.G. Matos, L.R. Avila, E.C.O. Nassor, A. Cestari, K.J. Ciuffi, P.S. Calefi, E.J. Nassar, Journal of Luminescence, 130 (2010) 488-493.
- S. Nakamura, T. Mukai, M. Senoh, Appl. Phys. Lett., 64 (1994) 1687.
- M. Mikami, A. Oshiyama, Phys. Rev., B, 60 (1999) 1707.
- M. R. Royce, P. Lancaster, U.P. 3418246 (1968).
- P. N. Yocom, U.S.P. Office, (1968).
- M. Kottaisamy, H. Horikawa, H. Kominami, T. Aoki, N. Azuma, T. Nakamura, Y. Nakanishi, Y. J. Hatanaka, Electrochem. Soc., 147 (2000) 1612.
- C. L. Lo, J. G. Duh, B. S. Chiou, J. Electrochem. Soc., 149 (2002) 129.
- S. I. Mho, S. Y. Chang, C. I. Jeon, C. H. Pyun, Q. W. Choi, C. H. Kim, Bull. Kor. Chem.Soc., 11(1990) 386.

(<sup>5</sup>D<sub>4</sub>→<sup>7</sup>F<sub>5</sub>) emission in table 1 given on page 10. The emitting color of the phosphor can be tuned in the respective color region either by changing the concentration of dopant or by changing the excitation wavelength [29, 30].

## IV. CONCLUSION

In summary, we have successfully synthesized and investigated the luminescent properties of the Y<sub>2</sub>O<sub>2</sub>S:RE<sup>3+</sup> (RE<sup>3+</sup> = Dy<sup>3+</sup>, Eu<sup>3+</sup> or Tb<sup>3+</sup>) phosphors. The use of flux reduces the reaction temperature and enhances the reaction rate, finally results in single phase Y<sub>2</sub>O<sub>2</sub>S compound. The emission color of the obtained phosphors can be modulated either by controlling the doping content of the rare earth ions or by fixing the doping content and varying the excitation wavelength. The developed Y<sub>2</sub>O<sub>2</sub>S:RE<sup>3+</sup> (RE<sup>3+</sup> = Dy<sup>3+</sup>, Eu<sup>3+</sup> or Tb<sup>3+</sup>) phosphor can be stimulated (excited) in n-UV domain which is most desired requirement for commercially producing white light emitting diodes. The synthesized phosphor emits bright color in the blue, yellow, green and red region. Hence, it has likely potential to be used in phosphor converted light emitting diodes as a primary color emitter in 3 band pc-LEDs or red spectrum enhancer in yellow phosphor converted white light emitting diodes and therefore results indicate that these phosphors may be a promising candidates for white LEDs.

- S. H. Park, S. I. Mho, K. W. Lee, Bull. Kor. Chem. Soc., 17 (1996) 487.
- V. V. Shinde, S. J. Dhoble, Advanced Materials Letters 2014, 5(12), 706-711.
- V. V. Shinde, R. G. Kunghatkar, and S. J. Dhoble, wileyonlinelibrary.com /journal/luminescence (2015), DOI 10.1002/bio.2889.
- K. N. Shinde, et al., Phosphate phosphors for solid-state lighting, Springer Science & Business Media, 2012.
- Monali R. Kadukar, S. J. Dhoble, A. K. Sahu, V. Nayar, S. Sailaja, B. Sudhakar Reddy, Luminescence, 32(2) (2017) 159-170. https://doi.org/10.1002/bio.3161.
- B. Yuan, et al. Journal of Alloys and Compounds 644 (2015) 82-90.

15. L. Jing, X. Liu, Y. Li, Y Wang, Journal of Luminescence 162 (2015) 185-190.
16. K. N. Shinde , S. J. Dhoble, and A. Kumar, Journal of Luminescence 131.5 (2011) 931-937.
17. Y.Tian,B. Chen,B. Tian,R.Hua,J. Sun,L. Cheng,H. Zhong,X. Li,J. Zhang,Y. Zheng,T. Yu,L. Huang,Q. Meng,Journal of Alloys and Compounds, 509 (2011) 6096-6101
18. F. G. Meng, X. M. Zhang, H. J. Seo, Optics & Laser Technology, 44 (2012) 185-189
19. A. N. Yerpude, S. J. Dhoble, and B. Sudhakar Reddy, Physica B: Condensed Matter 454 (2014) 126-130.
20. Y. N. Xue, F. Xiao, and Q. Y. Zhang, Spectrochimica Acta Part A: Molecular and Biomolecular Spectroscopy 78.2 (2011) 607-611.
21. Z. Sun, M. Zhihua, et al. Journal of Alloys and Compounds 658 (2016)453-458.
22. K. N. Shinde, S. J. Dhoble, Journal of Fluorescence, 21, (2011) 2053 doi:10.1007/s10895-011-0920-5
23. S.J. Dhoble, V.B. Pawade, and K.N. Shinde, The European Physical Journal Applied Physics, (2010) doi: 10.1051/epjap/2010122.
24. A. D. Sontakke, K. Biswas, and K. Annapurna. Journal of Luminescence 129.11 (2009) 1347-1355.
25. S. V. Yap, R. M. Ranson, W. M. Cranton, , D. C. Koutsogeorgis, and G. B. Hix, Journal of Luminescence 129.5 (2009) 416-422.
26. H. Lai, A. Bao, Y. Yang, Y. Tao, H. Yang, Y. Zhang and L. Han, The Journal of Physical Chemistry C, 112.1 (2008) 282-286.
27. P. Y.Jia, J. Lin, and M. Yu, Journal of Luminescence 122 (2007) 134-136.
28. L. Wang, et al. Materials Chemistry and Physics 119.3 (2010) 490-494.
29. K. N. Shinde and S. J. Dhoble, Advanced Materials Letters, 1(3) (2010) 254-258.
30. V. V. Shinde, S. V. Shinde, N. S. Dhoble, S. J. Dhoble. Journal of Inorganic and Organometallic Polymers and Materials, 25.3 (2015) 593-600.

## AUTHORS PROFILE



**V. V. Shinde**, is presently working as Associate Professor & Head, Department of Electronics in Bajaj College of Science, Wardha, Maharashtra. He obtained his Ph. D. from R.T.M. Nagpur University, Nagpur. He has 33 years of teaching experience. He has 7 national and international research papers to his credit.



**Prof. Sanjay J. Dhoble**, is presently working as Professor in Department of Physics, RTM Nagpur university, Nagpur. He obtained his Ph.D. degree in 1992 in Solid State Physics from RTM Nagpur university, Nagpur.. He has 28 years of teaching and 27 Years of Research Experience. He worked on the

synthesis and characterization of solid-state lighting materials, development of radiation dosimetry phosphors using thermo luminescence technique and utilization of fly ash. Dr. Dhoble published/filed 16 patents and more than 552 research papers published in Scopus indexing journals. His h-index is 30 and 5209 citations on Scopus. Dr. Dhoble successfully guided 53 students for Ph.D. degree. He authored following books:

1. Principles and applications of organic light emitting diode (Publisher: Elsevier)
2. Nanomaterials for Green Energy (Publisher: Elsevier)
3. Spectroscopy of Lanthanide Doped Oxide Materials (Publisher: Elsevier)
4. Phosphate phosphors for solid state lighting (Publisher: Springer)
5. Phosphors for energy saving and conversion technology (Publisher: Taylor & Francis Group)
6. Phosphors: Synthesis and Applications (Publisher: Pan Stanford).

Dr. Dhoble is Editor of Luminescence: The Journal of Biological and Chemical Luminescence, John Wiley & Sons Ltd. Publication (Impact Factor: 1.691). He is also recipient of India's Top Faculty Research Award-2018 by Careers 360, for the top ten researchers in India in Physics on the basis of research papers published in Scopus research database in session 2017-2018, on 20th March 2018. His ORCID Id: 0000-0002-4249-8228.

# A promising $\text{Sr}_5(\text{PO}_4)_3\text{Br}:\text{RE}^{3+}$ ( $\text{RE}^{3+} = \text{Dy}^{3+}$ , $\text{Eu}^{3+}$ , and $\text{Tb}^{3+}$ ) Phosphors for Near UV Excited White LED and Display Devices



V. V. Shinde, S. J. Dhoble

**Abstract** Single phase  $\text{Sr}_5(\text{PO}_4)_3\text{Br}:\text{RE}^{3+}$  ( $\text{RE}^{3+} = \text{Dy}^{3+}$ ,  $\text{Eu}^{3+}$  or  $\text{Tb}^{3+}$ ) phosphors were prepared by solid state reaction method and optical properties were investigated for the possible applications in white light emitting diodes (LED) and display devices. Prepared phosphors are characterized by X-ray diffraction, scanning electron microscopy, photoluminescence (PL) and FT-IR spectroscopy. The PL properties of  $\text{Sr}_5(\text{PO}_4)_3\text{Br}:\text{Dy}^{3+}$  phosphor shows the characteristic emission of blue (479 nm) and yellow (575 nm) light under near UV excitation of 387nm,  $\text{Sr}_5(\text{PO}_4)_3\text{Br}:\text{Eu}^{3+}$  shows characteristic orange (590 nm) and red (613 nm) under near UV excitation of 396 nm and  $\text{Sr}_5(\text{PO}_4)_3\text{Br}:\text{Tb}^{3+}$  shows green (545 nm) emission under 379 nm excitation. The results indicate that the  $\text{RE}^{3+}$  activated bromoapatite phosphor could be promising candidate for near UV-based white LEDs and display devices.

**Keywords:** Bromoapatite, FT-IR, Photoluminescence, Rare earth, SEM, XRD.

## I. INTRODUCTION

A phosphor is a luminescent material that absorbs radiation energy in a UV portion of the electromagnetic spectrum and emits energy in another visible portion of the electromagnetic spectrum. Phosphors are crystalline inorganic compounds in which small quantities of other elements, called “activators” are added to convert them into efficient fluorescent materials. With proper combination of activators and inorganic compounds, the color of the emission can be controlled. Most useful and well-known phosphors emit radiation in the visible portion of the electromagnetic spectrum in response to excitation by electromagnetic radiation outside the visible range. A light-emitting phosphor consists of a host lattice into which activator ions such as rare earths are doped at a few mol% [1]. White light-emitting diodes offer several advantages in terms of energy saving, reliability, and safety and therefore have become important in recent years. Nowadays, one of the most important part of optoelectronic devices are light emitting diodes (LEDs) because several factors are driving their development.

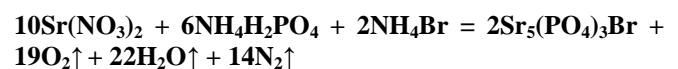
The most important ones are brightness, efficiency flexibility, lifetime, rugged construction, low power consumption and suitable driving voltage. These properties are contributing to growth in markets such as traffic lights, automotive brake signals displays, decorative signs and the many uses of the new white LED-based products [2].

To increase the efficiency of white LEDs, special attention has recently been paid to the development of new phosphors with good luminescence properties that can be excited in the near UV range (350–420 nm) for display devices [3]. Apatite phosphors also known as alkaline-earth-metal halo phosphates, which are naturally occurring materials, have recently been used for field-emission displays (FEDs) and would be suitable for white LEDs in the near future because of their low price, environmental friendliness, thermal stability and good photoluminescence properties.

Apatites have the generic molecular formula  $\text{M}_5(\text{PO}_4)_3\text{X}$  ( $\text{M}=\text{Ca}$ ,  $\text{Sr}$ ,  $\text{Ba}$ ;  $\text{X}=\text{F}$ ,  $\text{Cl}$ ,  $\text{Br}$ ,  $\text{OH}$ ). Apatite is one of the most interesting types of new inorganic materials due to the ability of the tetrahedral  $\text{PO}_4^{3-}$  group to bond with other structural units. Apatites are well known phosphor materials for their applications as laser hosts, and biocompatible materials. Among these,  $\text{Ba}_5(\text{PO}_4)_3\text{Cl}:\text{Eu}^{2+}$  is a promising material for X-ray imaging.  $\text{Sr}_5(\text{PO}_4)_3\text{Cl}:\text{Eu}^{2+}$  is an efficient photo luminescent material, used in high efficiency compact fluorescent lamp. To the best of our knowledge the reports on optical properties of rare earth doped  $\text{Sr}_5(\text{PO}_4)_3\text{Br}$  phosphors has not reported yet. Hence, in this work the PL study of  $\text{Dy}^{3+}$ ,  $\text{Eu}^{3+}$  and  $\text{Tb}^{3+}$  doped  $\text{Sr}_5(\text{PO}_4)_3\text{Br}$  phosphors are undertaken [3].

## II. EXPERIMENTAL METHOD

Bromoapatite phosphors  $\text{Sr}_5(\text{PO}_4)_3\text{Br}$  reported here were prepared by the solid state reaction method. The pure starting materials were  $\text{Sr}(\text{NO}_3)_2$ ,  $\text{NH}_4\text{H}_2\text{PO}_4$ ,  $\text{NH}_4\text{Br}$ ,  $\text{Dy}_2\text{O}_3$ ,  $\text{Eu}_2\text{O}_3$  and  $\text{Tb}_2\text{O}_3$  were used for preparation of  $\text{Sr}_5(\text{PO}_4)_3\text{Br}$  materials. The formation of  $\text{Sr}_5(\text{PO}_4)_3\text{Br}$  (pure) and  $\text{Sr}_5(\text{PO}_4)_3\text{Br}:\text{RE}^{3+}$  are shown by following chemical reaction:



In this synthesis the stoichiometric quantities of raw materials were weighted and mixed thoroughly by crushing mechanically for 1hr in agate mortar. These dry powders were then heated in a muffle furnace, at around  $150^\circ\text{C}$  for 2hrs.

Revised Manuscript Received on February 28, 2020.

\* Correspondence Author

V. V. Shinde, Department of Electronics, Bajaj College of Science, Wardha, India. E-mail: vvshinde.wda@gmail.com

S. J. Dhoble\*, Department of Physics, RTM Nagpur University, Nagpur, India. E-mail: sjdoble@rediffmail.com

© The Authors. Published by Blue Eyes Intelligence Engineering and Sciences Publication (BEIESP). This is an open access article under the CC-BY-NC-ND license <http://creativecommons.org/licenses/by-nc-nd/4.0/>

The powders were again crushed and heated at  $400^\circ\text{C}$  for 2hrs to remove all gases. The powders were crushed and finally annealed at about  $900^\circ\text{C}$  for 6 hours in air by slowly increasing the temperature of muffle furnace, and then cooled down slowly to room temperature. The powder were crushed again in agate mortar as done previously. Finally the samples were quenched at  $1100^\circ\text{C}$  after heating 1hour to observe the effect of raising the temperature on intensity of PL emission. Same method were utilized for the preparation of the rare earth ( $\text{Dy}^{3+}, \text{Eu}^{3+}$  and  $\text{Tb}^{3+}$ ) doped phosphors in various molar concentration (0.1-2mol%).

The X-ray powder diffraction method using  $\text{Cu K}\alpha$  radiation was used for the prepared host lattice  $\text{Sr}_5(\text{PO}_4)_3\text{Br}$  to characterized it for phase purity and crystallinity. Phosphors morphology was checked by a scanning electron microscope (SEM). Bruker Fourier transform infrared spectrometer was used to record infrared spectra. It was taken in the range of  $500$  to  $4000\text{cm}^{-1}$ . The excitation and emission spectra, for the measurement of spectroscopic properties, were recorded at room temperature on Shimadzu make RF5301PC spectro-fluorometer using a spectral slit width of  $1.5\text{nm}$ . for all samples [4]-[6].

### III. RESULTS AND DISCUSSION

#### A. X-ray Diffraction (XRD)

X-ray diffraction analysis was carried out to confirm the forming of prepared host by solid state method. Figure 1 shows the diffraction data pattern for the prepared pure  $\text{Sr}_5(\text{PO}_4)_3\text{Br}$  phosphor host. The sharp diffraction peaks of XRD patterns of strontium bromoapatite confirms the forming of a crystalline  $\text{Sr}_5(\text{PO}_4)_3\text{Br}$  host. It shows good similarity with ICDD data file 89-5876 of  $\text{Sr}_5(\text{PO}_4)_3\text{Br}$ .

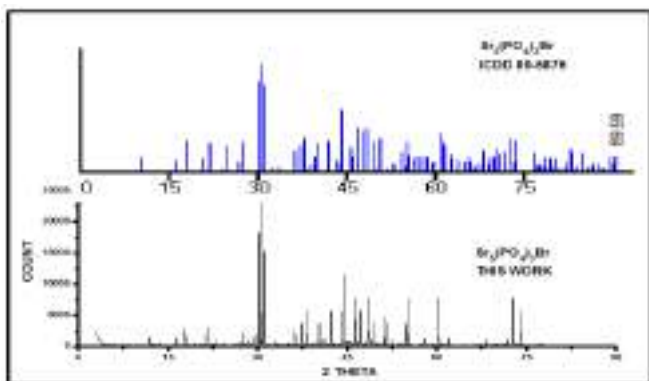


Figure 1: XRD pattern of synthesized Bromoapatite  $\text{Sr}_5(\text{PO}_4)_3\text{Br}$  Phosphors.

The XRD diffraction pattern of prepared  $\text{Sr}_5(\text{PO}_4)_3\text{Br}$  host did not indicate existence of the nitrate component and the remains of ammonia. This shows an indirect evidence for the homogeneous formation of the prepared  $\text{Sr}_5(\text{PO}_4)_3\text{Br}$  host.

The crystal structure of prepared  $\text{Sr}_5(\text{PO}_4)_3\text{Br}$  host was refined precisely using the single crystal structure model of  $\text{Sr}_5(\text{PO}_4)_3\text{Br}$  from XRD data, earlier by the Rietveld method [7]. The prepared  $\text{Sr}_5(\text{PO}_4)_3\text{Br}$  host has same structure with  $\text{Sr}_5(\text{PO}_4)_3\text{Br}$  and belongs to  $\text{P63/m}$  space group with cell parameters are  $a_0 = 9.9641(1)\text{\AA}$ ,  $c_0 = 7.2070(1)\text{\AA}$ ,  $\alpha = \beta = 90^\circ$ ,  $\gamma = 120^\circ$ ,  $Z = 2$  [8] [8]-[10].

#### B. Surface Morphology

The surface morphology and crystallite sizes were investigated by scanning electron microscope analysis for the prepared  $\text{Sr}_5(\text{PO}_4)_3\text{Br}$  host. It is shown in figure 2. The SEM observations of the sample shows highly agglomerated crystallite morphology. Estimation of particle size is uncertain as the particles are highly amassed together. At higher magnification, SEM analysis shows the presence of particles in the submicron range in some regions of the SEM micrographs with irregular spherical morphology [11].

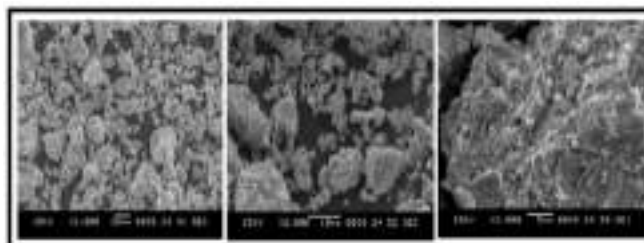


Figure 2: Scanning electron microscope (SEM) micrographs of synthesized Bromoapatite  $\text{Sr}_5(\text{PO}_4)_3\text{Br}$ .

#### C. FT-IR Analysis

The infrared spectrum for bromoapatite  $\text{Sr}_5(\text{PO}_4)_3\text{Br}$  phosphors is as shown in figure 3. The phosphate group is the only and essential polyatomic ion in bromoapatite  $\text{Sr}_5(\text{PO}_4)_3\text{Br}$  phosphors. A unit cell of phosphate group  $\text{PO}_4^{3-}$  contains three phosphorous atoms. Each phosphorous atom is surrounded by a tetrahedron of oxygen atoms. The most characteristic chemical group in the FTIR spectrum of synthesized bromoapatite is  $\text{PO}_4^{3-}$ .

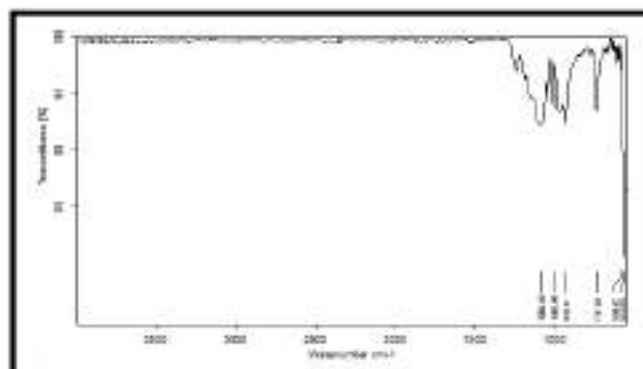


Figure 3: FT-IR spectrum of synthesised Bromoapatite  $\text{Sr}_5(\text{PO}_4)_3\text{Br}$  phosphors.

The infrared spectra of bromoapatite show characteristic bands originating from P-O or O-P-O vibrations present in  $[\text{PO}_4]$  tetrahedral. These are the bands due to the symmetric stretching vibration  $\nu_1$  ( $933\text{ cm}^{-1}$ ) and  $\nu_3$  asymmetric stretching modes ( $1084\text{ cm}^{-1}$  and  $1008\text{ cm}^{-1}$ ) vibrations as well as bands originating from the asymmetric vibrations  $\nu_4$  ( $590\text{ cm}^{-1}$ ,  $561\text{ cm}^{-1}$ ) occurring within these tetrahedral. In addition, the peak at  $737\text{ cm}^{-1}$ , implies the presence of  $\text{P}_2\text{O}_7^{4-}$  group which is a characteristic to strontium bromo phosphate phase. It is further inferred that the prepared host is free from nitrate group ( $2213\text{-}2034\text{ cm}^{-1}$ ).



It is also observed that OH- bands completely evaporated in a prepared bromoapatite host, implying that bromine ions have been substituted effectively and therefore the characteristic bands of the  $(\text{PO}_4)^{3-}$  groups are observed [4].

#### D. PL Emission Of $\text{RE}^{3+}$ In $\text{Sr}_5(\text{PO}_4)_3\text{Br}$

##### i) Luminescence Studies Of $\text{Sr}_5(\text{PO}_4)_3\text{Br}:\text{Dy}^{3+}$

The PL excitation and emission spectra of the as prepared  $\text{Dy}^{3+}$  activated  $\text{Sr}_5(\text{PO}_4)_3\text{Br}$  phosphor are shown in figure 4. The excitation spectrum for all the  $\text{Sr}_5(\text{PO}_4)_3\text{Br}$  phosphors with various  $\text{Dy}^{3+}$  concentrations was observed at 375nm emission corresponding to the  $^4\text{F}_{9/2} \rightarrow ^6\text{H}_{13/2}$  transition of  $\text{Dy}^{3+}$ . The excitation peaks observed at 350nm ( $^6\text{H}_{15/2} \rightarrow ^6\text{P}_{7/2}$ ), 365nm ( $^6\text{H}_{15/2} \rightarrow ^6\text{P}_{5/2}$ ) and 387nm ( $^6\text{H}_{15/2} \rightarrow ^4\text{I}_{13/2}$ ) were due to f-f transition [12]. We chose 387nm as excitation wavelength amongst all these three near UV excitation peaks, because it is more intense and suitable for solid state lighting for display devices [13].

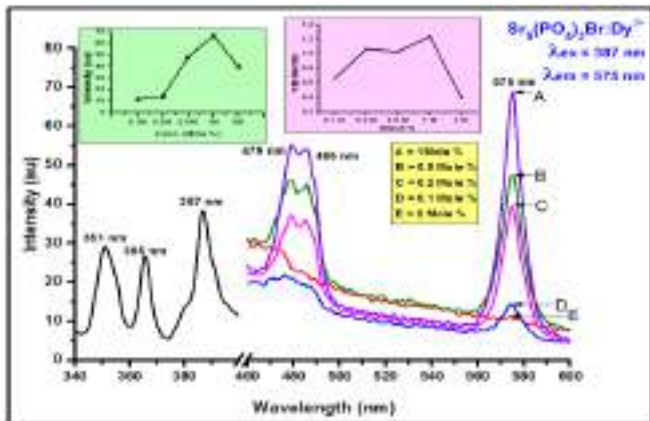


Figure 4: Excitation and emission spectra of  $\text{Sr}_5(\text{PO}_4)_3\text{Br}:\text{Dy}^{3+}$  phosphors.

The emission spectra of  $\text{Sr}_5(\text{PO}_4)_3\text{Br}:\text{Dy}^{3+}$  ( $\text{Dy}^{3+}$  mol% = 0.1, 0.2, 0.5, 1 and 2) phosphors excited at 387nm range display two predominant peaks at 479nm (blue,  $^4\text{F}_{9/2} \rightarrow ^6\text{H}_{15/2}$ ) and 575 nm (yellow,  $^4\text{F}_{9/2} \rightarrow ^6\text{H}_{13/2}$ ) zone[11]. The blue emission is due to magnetic dipole transition, and the yellow emission belongs to the hypersensitive (forced electric dipole) transition following the selection rule,  $\Delta J = 2$  [4]. The magnetic dipole transition gives blue emission and the yellow emission is due to hypersensitive forced electric dipole hypersensitive transition. It follows  $\Delta J = 2$  selection rule. It is known that the blue emission ( $^4\text{F}_{9/2} \rightarrow ^6\text{H}_{15/2}$ ) at 479nm is insensitive to the crystal field around the  $\text{Dy}^{3+}$  ions and the yellow emission ( $^4\text{F}_{9/2} \rightarrow ^6\text{H}_{13/2}$ ) at 575nm is hypersensitive transition and it is strongly influenced by the surrounding environment around  $\text{Dy}^{3+}$  [12]-[14]. In this prepared host, the stronger yellow emission implies that low symmetry sites (without inversion symmetry) have been occupied by  $\text{Dy}^{3+}$  ions. Due to the porosity of spinal structure, the  $\text{Dy}^{3+}$  ion may enter into the host lattice to substitute  $\text{Sr}^{2+}$  ions as the ionic radii of  $\text{Dy}^{3+}$  ions (912 pm) are much smaller than that of  $\text{Sr}^{2+}$  ions(118pm)[15].

Dependence of luminescence intensity on concentration of  $\text{Dy}^{3+}$  ions for  $\text{Sr}_5(\text{PO}_4)_3\text{Br}:\text{Dy}^{3+}$  prepared phosphor is shown in inset of figure 4. The optimum concentration is 1mol% and

decreases for higher concentration due to concentration quenching.

The yellow to blue (Y/B) emission intensity ratio is depicted in inset of figure 4. By carefully observing the emission spectra it is found that the yellow to blue (Y/B) emission intensity ratio is greater than 1. This confirms that  $\text{Dy}^{3+}$  ions occupy low symmetry site with no inversion symmetry in  $\text{Sr}_5(\text{PO}_4)_3\text{Br}$  prepared host [16].

##### ii) Luminescence Studies Of $\text{Sr}_5(\text{PO}_4)_3\text{Br}:\text{Eu}^{3+}$

The PL excitation and emission spectra of the prepared  $\text{Sr}_5(\text{PO}_4)_3\text{Br}:\text{Eu}^{3+}$  phosphors are shown in figure 5. It is obtained by tracking the red emission at 613nm and near UV excitation at 396nm, respectively. The excitation band observed at 396nm ( $^7\text{F}_0 \rightarrow ^5\text{L}_6$ ) was sharp and caused by f-f transition.

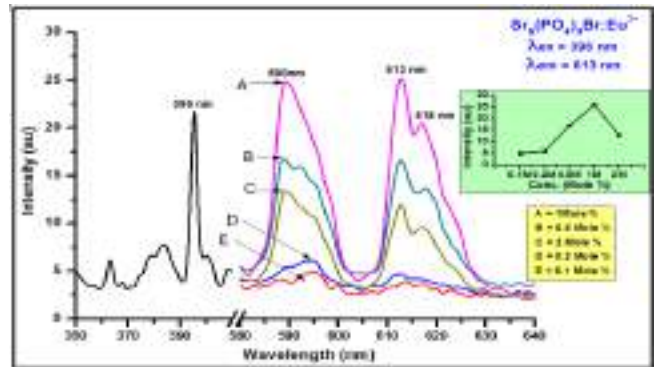


Figure 5: Excitation and emission spectra of  $\text{Sr}_5(\text{PO}_4)_3\text{Br}:\text{Eu}^{3+}$  phosphors.

The characteristic emission bands of  $\text{Sr}_5(\text{PO}_4)_3\text{Br}:\text{Eu}^{3+}$  phosphor are in the region of 580 to 640nm corresponding to intra 4f-shell transitions of  $^5\text{D}_0 \rightarrow ^7\text{F}_J$  ( $J=0, 1, 2, 3, 4$ ) of  $\text{Eu}^{3+}$ . With  $\lambda_{\text{ex}} = 396\text{nm}$ , the emissions at 590nm (Orange,  $^5\text{D}_0 \rightarrow ^7\text{F}_1$ , magnetic dipole) and 613 nm (Red,  $^5\text{D}_0 \rightarrow ^7\text{F}_2$ , electric dipole which is hyper sensitive) were found with emission peaks differing only in their relative intensity values. The intensity of emission at 590nm and 613nm was found to be almost equal.

Dependence of luminescence intensity on concentration of  $\text{Eu}^{3+}$  ions for  $\text{Sr}_5(\text{PO}_4)_3\text{Br}:\text{Eu}^{3+}$  prepared phosphor is shown in inset of figure 5. The highest luminescent intensity is observed at 1 mol% and then decreases with the increase in concentration of the  $\text{Eu}^{3+}$  activator ions due to concentration quenching effect [4][17].

##### iii) Luminescence Studies Of $\text{Sr}_5(\text{PO}_4)_3\text{Br}:\text{Tb}^{3+}$

The PL excitation and emission spectra of the prepared  $\text{Tb}^{3+}$  activated  $\text{Sr}_5(\text{PO}_4)_3\text{Br}$  phosphors are shown in figure 6. The excitation peaks associated with f-f transitions were observed at 351nm ( $^7\text{F}_6 \rightarrow ^5\text{L}_9$ ), 371nm ( $^7\text{F}_6 \rightarrow ^5\text{G}_5$ ) and 379nm ( $^7\text{F}_6 \rightarrow ^5\text{G}_6$ ). Amongst these, excitation wavelength above 379nm is taken which is more suitable for solid state lighting and display devices [7][18].

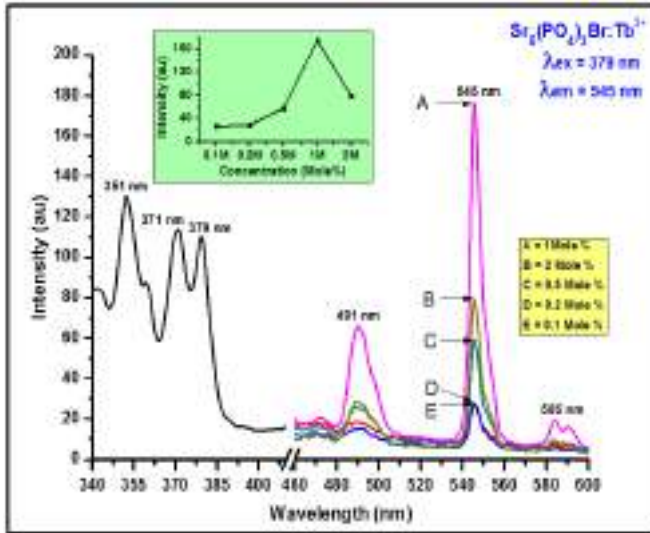


**Figure 6: Excitation and emission spectra of  $\text{Sr}_5(\text{PO}_4)_3\text{Br}:\text{Tb}^{3+}$  phosphors.**

$\text{Sr}_5(\text{PO}_4)_3\text{Br}:\text{Tb}^{3+}$  phosphor shows sharp and intense narrow green emission ( $^5\text{D}_4 \rightarrow ^7\text{F}_5$ , magnetic dipole transition ( $\Delta J = \pm 1$ )) at 545nm with other weak blue emission ( $^5\text{D}_4 \rightarrow ^7\text{F}_6$ ) at 491nm, and very weak yellow emission ( $^5\text{D}_4 \rightarrow ^7\text{F}_4$ ) at 585nm due to 4f-4f transitions of  $\text{Tb}^{3+}$  ions. The PL emission peaks differs only in their relative intensity. The emission from the higher energy level ( $^5\text{D}_3 \rightarrow ^7\text{F}_J$  ( $J = 3, 4, 5, 6$ )) in the blue spectral region is not observed. The reason for this may be the formation of terbium ions pairs ( $\text{Tb}-\text{Tb}$ ) and because of this the excitation energy of the  $^5\text{D}_3$  level relaxes to the  $^5\text{D}_4$  level by cross relaxation. Another possible reason for this may be due to fast relaxation from  $^5\text{D}_3$  level since its lifetime is very small [19]-[21].

Dependence of luminescence intensity on concentration of  $\text{Tb}^{3+}$  ions for  $\text{Sr}_5(\text{PO}_4)_3\text{Br}:\text{Tb}^{3+}$  prepared phosphor is shown in inset of figure 6. Up to 1 mol%, the PL intensity rises with increase of  $\text{Tb}^{3+}$  ion concentration and thereafter falls at higher concentrations due to concentration quenching [22].

**iv) Effect Of Temperature On PL Intensity Of  $\text{Sr}_5(\text{PO}_4)_3\text{Br}:\text{RE}^{3+}$  (Where  $\text{RE}^{3+} = \text{Dy}^{3+}$ ,  $\text{Eu}^{3+}$ ,  $\text{Tb}^{3+}$ )**

The prepared samples of  $\text{Sr}_5(\text{PO}_4)_3\text{Br}:\text{RE}^{3+}$  were quenched at  $1100^\circ\text{C}$  for 1 hour and their excitation and emission spectra were compared with the samples annealed at  $900^\circ\text{C}$  for 6 hours. The two spectra i.e. one annealed at  $900^\circ\text{C}$  for 6 hours and the as-quenched one are identical but with a large difference in intensity. It implies that the local environment for the  $\text{RE}^{3+}$  ( $\text{RE}^{3+} = \text{Dy}^{3+}$ ,  $\text{Eu}^{3+}$ ,  $\text{Tb}^{3+}$ ) ions remains same in both. A rise in emission intensity in as quenched sample is due to the better crystallinity of  $\text{Sr}_5(\text{PO}_4)_3\text{Br}$ , which further could be attributed to the reduced surface area due to the reduction of the concentration of inherent defective states or adsorbed species [23][24].

**a) Effect Of Temperature On PL Intensity Of  $\text{Sr}_5(\text{PO}_4)_3\text{Br}:\text{Dy}^{3+}$**

In figure 7, excitation and emission spectra of a quenched sample of  $\text{Sr}_5(\text{PO}_4)_3\text{Br}:\text{Dy}^{3+}$  is shown which indicates the radical change in the yellow to blue (Y/B) ratio. The yellow to blue (Y/B) ratio for  $\text{Sr}_5(\text{PO}_4)_3\text{Br}:\text{Dy}^{3+}$  as quenched sample is found to be less than one indicating that magnetic dipole

transition (Blue emission,  $^4\text{F}_{9/2} \rightarrow ^6\text{H}_{15/2}$ ) of  $\text{Dy}^{3+}$  take up high symmetry site (with an inversion centre), prominently [25]-[27].

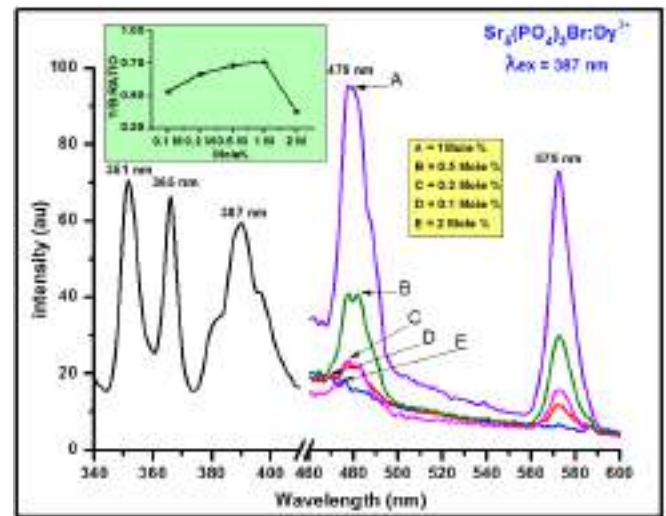


**Figure 7: Excitation and emission spectra of quenched  $\text{Sr}_5(\text{PO}_4)_3\text{Br}:\text{Dy}^{3+}$  phosphors.**

**b) Effect Of Temperature On PL Intensity Of  $\text{Sr}_5(\text{PO}_4)_3\text{Br}:\text{Eu}^{3+}$**

In figure 8, excitation and emission spectra of a quenched sample of  $\text{Sr}_5(\text{PO}_4)_3\text{Br}:\text{Eu}^{3+}$  is shown which indicates the drastic change in the red to orange colour emission. It suggests that the local environment for the  $\text{Eu}^{3+}$  ion is same in both. The ration of red to orange colour emission for annealed and as quenched sample is found to be greater than one and hence we can infer that  $\text{Eu}^{3+}$  ions did not take up inversion symmetry site in  $\text{Sr}_5(\text{PO}_4)_3\text{Br}$  [4].

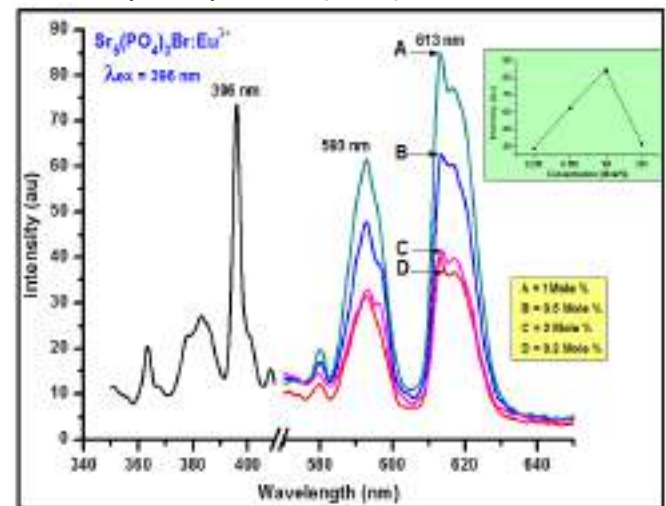


**Figure 8: Excitation and emission spectra of quenched  $\text{Sr}_5(\text{PO}_4)_3\text{Br}:\text{Eu}^{3+}$  phosphors.**

**c) Effect Of Temperature On PL Intensity Of  $\text{Sr}_5(\text{PO}_4)_3\text{Br}:\text{Tb}^{3+}$**

Figure 9 shows the excitation and emission spectra of a quenched sample of  $\text{Sr}_5(\text{PO}_4)_3\text{Br}:\text{Tb}^{3+}$ . The change in the intensity of excitation and emission spectra implies that the local environment for the  $\text{Tb}^{3+}$  ion is same in both.



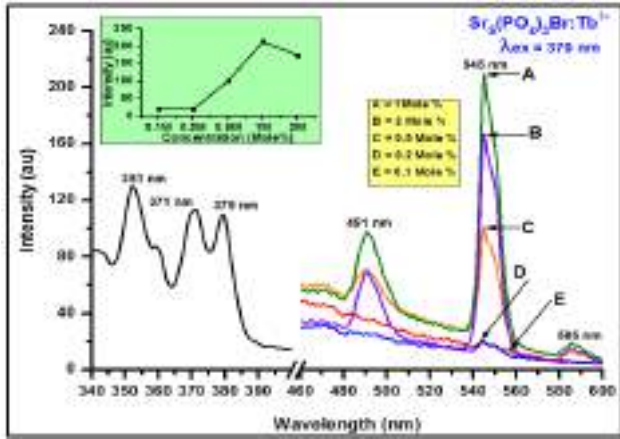


Figure 9: Excitation and emission spectra of quenched Sr<sub>5</sub>(PO<sub>4</sub>)<sub>3</sub>Br:Tb<sup>3+</sup> phosphors.

E. Chromatic Properties

The figure 10 shows the CIE (Commission International de l'Eclairage) chromaticity co-ordinates of the prepared phosphor Sr<sub>5</sub>(PO<sub>4</sub>)<sub>3</sub>Br:RE<sup>3+</sup> (RE= Dy<sup>3+</sup>, Eu<sup>3+</sup>, Tb<sup>3+</sup>). The (X, Y) chromatic co-ordinates are calculated using the colour calculator radiant imaging software for Sr<sub>5</sub>(PO<sub>4</sub>)<sub>3</sub>Br:RE are summarized in table III [4][13].

The comparison of percentage change in excitation and emission intensity of PL spectra is summarized in table I and table II, respectively.

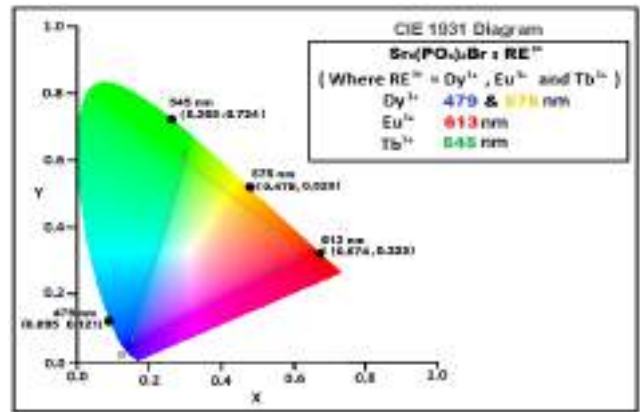


Figure 10: Chromatic graph of Sr<sub>5</sub>(PO<sub>4</sub>)<sub>3</sub>Br:RE<sup>3+</sup> (RE<sup>3+</sup> = Dy<sup>3+</sup>, Eu<sup>3+</sup>, Tb<sup>3+</sup>) phosphor excited near UV excitation.

Table I: % increase in intensity of excitation spectra of Sr<sub>5</sub>(PO<sub>4</sub>)<sub>3</sub>Br:RE<sup>3+</sup> phosphors.

PHOSPHOR	Conc. (Mol%)	Excitation Spectrum (900°C, 6 Hours.)		Excitation spectrum (1100°C, 1 Hours.)		Increase in intensity (%)
		λ <sub>ex</sub> (nm)	Intensity (au)	λ <sub>ex</sub> (nm)	Intensity (au)	
Sr <sub>5</sub> (PO <sub>4</sub> ) <sub>3</sub> Br:Dy <sup>3+</sup>	1	387	38	387	59	55.26
Sr <sub>5</sub> (PO <sub>4</sub> ) <sub>3</sub> Br:Eu <sup>3+</sup>	1	396	22	396	74	236.36
Sr <sub>5</sub> (PO <sub>4</sub> ) <sub>3</sub> Br:Tb <sup>3+</sup>	1	379	110	379	110	00.00

Table II: % increase in intensity of emission spectra of Sr<sub>5</sub>(PO<sub>4</sub>)<sub>3</sub>Br:RE<sup>3+</sup> phosphors.

PHOSPHOR	Conc. (Mol%)	Emission Spectra (900°C, 6 Hours)		Emission spectra (1100°C, 1 Hours)		Increase in intensity (%)
		λ <sub>em</sub> (nm)	Intensity (au)	λ <sub>em</sub> (nm)	Intensity (au)	
Sr <sub>5</sub> (PO <sub>4</sub> ) <sub>3</sub> Br:Dy <sup>3+</sup>	1	479	85	479	95	11.76
		575	69	575	73	5.79
Sr <sub>5</sub> (PO <sub>4</sub> ) <sub>3</sub> Br:Eu <sup>3+</sup>	1	613	25	613	85	240.00
Sr <sub>5</sub> (PO <sub>4</sub> ) <sub>3</sub> Br:Tb <sup>3+</sup>	1	545	177	545	210	18.64

Table III: The (X, Y) chromatic co-ordinates for synthesised Sr<sub>5</sub>(PO<sub>4</sub>)<sub>3</sub>Br:RE<sup>3+</sup> phosphors.

PHOSPHOR	Excitation (nm)	Strong Emission (nm)	(X,Y) Coordinate	Colour Region
Sr <sub>5</sub> (PO <sub>4</sub> ) <sub>3</sub> Br: Dy <sup>3+</sup>	387	479	(0.095, 0.121)	Blue
		575	(0.478, 0.520)	Yellow
Sr <sub>5</sub> (PO <sub>4</sub> ) <sub>3</sub> Br: Eu <sup>3+</sup>	396	613	(0.674, 0.325)	Red
Sr <sub>5</sub> (PO <sub>4</sub> ) <sub>3</sub> Br: Tb <sup>3+</sup>	379	545	(0.265, 0.724)	Green

#### IV. CONCLUSION

The bromoapatite  $\text{Sr}_5(\text{PO}_4)_3\text{Br}$  doped with different concentrations of  $\text{RE}^{3+}$  ( $\text{RE}^{3+} = \text{Dy}^{3+}, \text{Eu}^{3+}, \text{Tb}^{3+}$ ) ions have been synthesized by solid state diffusion method and are characterized for their physical properties through XRD, SEM, FT-IR, absorption and luminescence spectra measurements. Solid state lighting phosphors uses Hg free excitation in the 300 to 400 nm range. The excitation spectra of  $\text{Sr}_5(\text{PO}_4)_3\text{Br}:\text{RE}^{3+}$  has shown good absorption in near UV region. The emissions of prepared  $\text{Sr}_5(\text{PO}_4)_3\text{Br}:\text{RE}^{3+}$  ( $\text{RE} = \text{Dy}^{3+}, \text{Eu}^{3+}, \text{Tb}^{3+}$ ) phosphors are observed at 479 nm (Yellow), 575nm (Blue) for  $\text{Dy}^{3+}$  ions, 593nm (Orange), 613 nm (Red) for  $\text{Eu}^{3+}$  ions and 545 nm (Green) for  $\text{Tb}^{3+}$  ions, when excited by near UV excitation source. Based on the results obtained in the present work, we propose that, these optoelectronic luminescent phosphors have possible applications as a near UV convertible phosphor for white light emitting diodes and display devices.

#### REFERENCES

1. A. A., Setlur, A. M. Srivastava, H. A. Comanzo, D. Hancu, and L. J. V. Briel, (2009). U.S. Patent No. 7,573,072. Washington, DC: U.S. Patent and Trademark Office.
2. J. Kovac, L. Peternai, and O. Lengyel, Thin Solid Films 433.1-2 (2003): 22-26.
3. X Zhang, J Zhang, J Huang, X Tang and M Gong, Journal of Luminescence 130.4 (2010): 554-559.
4. V. V. Shinde and S. J. Dhoble, Advanced Materials Letters 2014, 5(12), 706-711.
5. R. L. Kohale, and S. J. Dhoble, Journal of Alloys and Compounds 753 (2018) 111-118.
6. B. P. Kore, N. S. Dhoble, S. P. Lochab and S. J. Dhoble, Journal of Luminescence 145 (2014): 299-306.
7. D. Kim, S. C. Kim, J. S. Bae, S. Kim, S. J. Kim and J. C. Park, Inorganic chemistry 55.17 (2016): 8359-8370.
8. C. D. Mungmode, D. H. Gahane and S. V. Moharil, Journal of Optics 48.1 (2019): 49-53.
9. I. M. Nagpure, S. S. Pitale, E. Coetsee, O. M. Ntwaeaborwa, J. J. Terblans, and H. C. Swart, Physica B: Condensed Matter 407.10 (2012): 1505-1508.
10. P. P. Mokoena, H.C. Swart and O. M. Ntwaeaborwa, Physica B: Condensed Matter 535 (2018): 57-62.
11. B. P. Kore, N. S. Dhoble, K. Park and S. J. Dhoble, Journal of Luminescence 143 (2013): 337-342.
12. S.N. Ogugua, H. C. Swart, and O. M. Ntwaeaborwa, Physica B: Condensed Matter 480 (2016): 131-136.
13. V. V. Shinde, S. V. Shinde, N. S. Dhoble and S. J. Dhoble. Journal of Inorganic and Organometallic Polymers and Materials, 25.3 (2015) 593-600.
14. X. Sun, S. Zhao, Y. Fei, L. Huang and S. Xu, Optical Materials 38 (2014): 92-96.
15. I. M. Nagpure, S. Saha, and S. J. Dhoble. Journal of luminescence 129.9 (2009): 898-905.
16. T. Wang, Y. Hu, L. Chen, X. Wang and M. He, Journal of Luminescence 181 (2017): 189-195.
17. I. M. Nagpure, K. N. Shinde, V. Kumar, O. M. Ntwaeaborwa, S. J. Dhoble, and H. C. Swart, Journal of Alloys and Compounds 492.1-2 (2010): 384-388.
18. K.N. Shinde, S.J. Dhoble and A. Kumar, Physica B: Condensed Matter 406.1 (2011): 94-99.
19. I. M. Nagpure, K. N. Shinde, S. J. Dhoble and A. Kumar, Journal of Alloys and Compounds 481.1-2 (2009): 632-638.
20. A. J. Fernández - Carrión, M. Ocaña, J. García-Sevillano, E. Cantelar, and A. I. Becerro, The Journal of Physical Chemistry C 118.31 (2014): 18035-18043.
21. P. Nimishe, and S. J. Dhoble. Bulletin of Materials Science 34.5 (2011) 1119-1125.
22. P. B. Devaraja, D. N. Avadhani, H. Nagabhushana, S. C. Prashantha, S. C. Sharma, B. M. Nagabhushana, and B.D. Prasad, Materials Characterization 97 (2014): 27-36.
23. F. Gu, S. F. Wang, M. K. Lü, G. J. Zhou, S. W. Liu and D. Xu, Chemical physics letters 380.1-2 (2003): 185-189.

24. L. Zhou, J. Huang, F. Gong, Y. Lan, Z. Tong and J. Sun, Journal of Alloys and Compounds, 495(1), 268-271.
25. G.S.R. Raju, J.Y. Park, H.C. Jung, H.K. Yang, B.K. Moon, J. H. Jeong, and J. H. Kim, Optical Materials 31.8 (2009): 1210-1214.
26. L. M. Fu, B. Z. Lin, Y. L. Chan, O. Zhang, B. Li, H. Qu, Journal of Alloys and Compounds 525 (2012) 14-21.
27. K. Mondal and J. Manam, Journal of Molecular Structure 1125 (2016) 503-513.

#### AUTHORS PROFILE



**V. V. Shinde**, is presently working as Associate Professor & Head, Department of Electronics in Bajaj College of Science, Wardha, Maharashtra. He obtained his Ph. D. from R.T.M. Nagpur University, Nagpur. He has 33 years of teaching experience. He has 7 national and international research papers to his credit.



**Prof. Sanjay J. Dhoble**, is presently working as Professor in Department of Physics, RTM Nagpur university, Nagpur. He obtained his Ph.D. degree in 1992 in Solid State Physics from RTM Nagpur university, Nagpur. He has 28 years of teaching and 27 Years of Research Experience. He worked on the synthesis and characterization of solid-state lighting materials, development of radiation dosimetry phosphors using thermo luminescence technique and utilization of fly ash. Dr. Dhoble published/filed 16 patents and more than 552 research papers published in Scopus indexing journals. His h-index is 30 and 5209 citations on Scopus. Dr. Dhoble successfully guided 53 students for Ph.D. degree. He authored following books:

1. Principles and applications of organic light emitting diode (Publisher: Elsevier)
2. Nanomaterials for Green Energy (Publisher: Elsevier)
3. Spectroscopy of Lanthanide Doped Oxide Materials (Publisher: Elsevier)
4. Phosphate phosphors for solid state lighting (Publisher: Springer)
5. Phosphors for energy saving and conversion technology (Publisher: Taylor & Francis Group)
6. Phosphors: Synthesis and Applications (Publisher: Pan Stanford).

**Dr. Dhoble**, is Editor of Luminescence: The Journal of Biological and Chemical Luminescence, John Wiley & Sons Ltd. Publication (Impact Factor: 1.691). He is also recipient of India's Top Faculty Research Award-2018 by Careers 360, for the top ten researchers in India in Physics on the basis of research papers published in Scopus research database in session 2017-2018, on 20th March 2018. His ORCID Id: 0000-0002-4249-8228.



# Synthesis and Luminescence Properties of $\text{La}_2\text{O}_2\text{S}:\text{RE}^{3+}$ ( $\text{RE}^{3+} = \text{Ce}^{3+}, \text{Dy}^{3+}, \text{Eu}^{3+}$ and $\text{Tb}^{3+}$ ) Submicron Size Phosphors for Lamp Industry

V. V. Shinde, S. J. Dhoble



**Abstract:**  $\text{RE}^{3+}$  ( $\text{RE}^{3+} = \text{Ce}^{3+}, \text{Dy}^{3+}, \text{Eu}^{3+}$  and  $\text{Tb}^{3+}$ ) doped  $\text{La}_2\text{O}_2\text{S}$  phosphors was synthesized by solid state flux fusion method and their down conversion spectral properties were studied as a function different  $\text{RE}^{3+}$  concentrations and reported in this paper. The solid state flux fusion results in well crystallized hexagonal shaped phosphor particles. The samples were characterized by XRD, SEM, FT-IR photoluminescence (PL) and CIE colour co-ordinates techniques. The lanthanum oxysulphide ( $\text{La}_2\text{O}_2\text{S}$ ) phosphor doped with  $\text{Ce}^{3+}$  shows broad band emission with peak at 390 nm and 415 nm when excited at 340 nm excitation.  $\text{La}_2\text{O}_2\text{S}:\text{Dy}^{3+}$  shows efficient blue and yellow band emissions at 480 nm and 572 nm.  $\text{La}_2\text{O}_2\text{S}:\text{Eu}^{3+}$  phosphor shows an orange and red emission at 590 nm and 615 nm. Whereas  $\text{La}_2\text{O}_2\text{S}:\text{Tb}^{3+}$  phosphor shows weak blue emission at 488 nm and strong green 545 nm. The excitation spectra used for the  $\text{La}_2\text{O}_2\text{S}:\text{RE}^{3+}$  (where  $\text{RE}^{3+} = \text{Ce}^{3+}, \text{Dy}^{3+}, \text{Eu}^{3+}$  and  $\text{Tb}^{3+}$ ) phosphors is in the near UV region extending from 350 to 400 nm, which is characteristics of near UV excited LED. The effect of the  $\text{RE}^{3+}$  ( $\text{RE}^{3+} = \text{Ce}^{3+}, \text{Dy}^{3+}, \text{Eu}^{3+}$  and  $\text{Tb}^{3+}$ ) concentration on the luminescence properties of  $\text{La}_2\text{O}_2\text{S}:\text{RE}^{3+}$  phosphors were also studied. The investigated prepared  $\text{La}_2\text{O}_2\text{S}$  phosphors may be suitable for a near UV excited W-LED. **Keywords:** Oxysulphide, SEM, FT-IR, PL, SSL, CIE.

## I. INTRODUCTION

Global demand for phosphor materials as efficient sources of energy is growing day by day and therefore the development of luminescent materials is the subject of extensive research in the recent years. Particular interest has been focused on inorganic luminescent materials, which have practical applications in almost all devices involving the artificial production of light [1]. In the last decade, there has been a dramatic increase in the number of research on solid-state lighting (SSL) and phosphor materials to generate white light using light emitting diodes (LEDs) as a new light source for general lighting and displays [2].

**Revised Manuscript Received on February 28, 2020.**

\* Correspondence Author

V. V. Shinde, Department of Electronics, Bajaj College of Science, Wardha, India, (email: [vvshinde.wda@gmail.com](mailto:vvshinde.wda@gmail.com))

S. J. Dhoble\*, Department of Physics, RTM Nagpur University, Nagpur-440033, India, (email: [sjdhoble@rediffmail.com](mailto:sjdhoble@rediffmail.com))

© The Authors. Published by Blue Eyes Intelligence Engineering and Sciences Publication (BEIESP). This is an [open access](https://creativecommons.org/licenses/by-nc-nd/4.0/) article under the CC-BY-NC-ND license <http://creativecommons.org/licenses/by-nc-nd/4.0/>

SSL technology has several advantages over conventional fluorescent lamps such as reduced power consumption, compactness, efficient light output, and longer lifetime.

The conventional white light illumination are mostly composed of blue-emitting InGaN chip and yellow phosphor, typically  $\text{Y}_3\text{Al}_5\text{O}_{12}:\text{Ce}^{3+}$  (YAG) [3, 4], which exhibits high luminescence efficiency and chemical stability. The combination of blue chip and YAG, however, show a lower colour rendering index ( $R_a$ ) of  $\sim 80$  due to the lack of red colour contribution. In the second approach, combination of blue LED with two other phosphors emitting red and green light are used. In third approach, three different phosphors which emit red, green and blue light are developed to cover nUV LEDs. The advantage of these LEDs is that they provide large colour area in the CIE diagram and thus enabling the light source more like sunlight. There are only a limited number of phosphor materials that are suitable for this this type of W-LEDs mentioned in third approach.

Lanthanide oxysulphides are known as wide gap (4.6 – 4.8 eV) semiconductors and widely used as efficient phosphorent material host for variety of applications in lighting and display.  $\text{La}_2\text{O}_2\text{S}:\text{RE}^{3+}$  (Where  $\text{RE}^{3+} = \text{Ce}^{3+}, \text{Dy}^{3+}, \text{Eu}^{3+}$  and  $\text{Tb}^{3+}$ ) is excellent material of current interest owing to their interesting opto-electronic properties. The aim of this work is to investigate and examine the luminescence properties of a  $\text{La}_2\text{O}_2\text{S}:\text{RE}^{3+}$  (Where  $\text{RE}^{3+} = \text{Ce}^{3+}, \text{Dy}^{3+}, \text{Eu}^{3+}$  and  $\text{Tb}^{3+}$ ) phosphor material with improved photo luminescent properties for lighting applications that can be excited in the near ultraviolet region. The improvement of luminescence intensity through energy transfer from co-doped  $\text{Ce}^{3+}$  to  $\text{Dy}^{3+}, \text{Eu}^{3+}$  and  $\text{Tb}^{3+}$  in  $\text{La}_2\text{O}_2\text{S}$  host is also discussed in this work.

## II. EXPERIMENTAL METHOD

A high temperature solid state flux fusion method was used for synthesising  $\text{La}_2\text{O}_2\text{S}:\text{RE}^{3+}$  (Where  $\text{RE}^{3+} = \text{Ce}^{3+}, \text{Dy}^{3+}, \text{Eu}^{3+}$  and  $\text{Tb}^{3+}$ ) phosphor. The starting materials are Lanthanum oxide ( $\text{La}_2\text{O}_3$ ), Sulphur powder (S) and flux Sodium carbonate ( $\text{Na}_2\text{CO}_3$ ), Tri potassium Phosphate ( $\text{K}_3\text{PO}_4$ ). Different flux materials such as Sodium carbonate ( $\text{Na}_2\text{CO}_3$ ) and Tripotassium Phosphate ( $\text{K}_3\text{PO}_4$ ) are used to increase the powder reactivity reaction rate, matrix formation and activator incorporation.

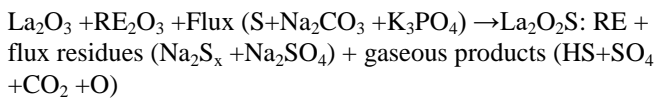


# Synthesis and Luminescence Properties of $\text{La}_2\text{O}_2\text{S}:\text{RE}^{3+}$ ( $\text{RE}^{3+} = \text{Ce}^{3+}, \text{Dy}^{3+}, \text{Eu}^{3+}$ and $\text{Tb}^{3+}$ ) Submicron Size Phosphors for Lamp Industry

These flux materials, which have melting point below the temperature of phosphor formation and dissolving partially one or both of the reactants, take no part in the solid-state reaction and undergo no reaction with the product [5,6]. Both S and  $\text{Na}_2\text{CO}_3$  were 30 to 50 weight % and  $\text{K}_3\text{PO}_4$  was 20 weight % of the total weight.

The dopants were Ammonium Hexanitratocerate ( $(\text{NH}_4)_2\text{Ce}(\text{NO}_3)_6$ ) for Ce, Dysprosium oxide ( $\text{Dy}_2\text{O}_3$ ) for Dy, Europium oxide ( $\text{Eu}_2\text{O}_3$ ) for Eu and Terbium Oxide ( $\text{Tb}_2\text{O}_3$ ) for Tb. The starting materials with dopants in stoichiometric ratio were thoroughly mixed using agate mortar and preheated at  $100^\circ\text{C}$  then fired at  $1150^\circ\text{C}$  for 90 min in a muffle furnace. When the furnace was cooled down to room temperature the samples were taken out and washed with distilled water 6 times and finally with a mild hydrochloric acid. The washed powder was subsequently dried and crushed to fine powder using agate mortar.

The formation of  $\text{La}_2\text{O}_2\text{S}$  phosphor particle follows the chemical formula:



The phase purity and structure of the final products of the oxysulphide phosphors  $\text{La}_2\text{O}_2\text{S}$  was examined by x-ray powder diffraction using  $\text{Cu K}\alpha$  radiation on a BRUKER – analytical x-ray diffractometer. Phosphor morphology was observed by a Geol-6380A scanning electron microscope (SEM). Infrared spectra of the pure  $\text{La}_2\text{O}_2\text{S}$  was recorded using a Bruker Fourier transform infrared spectrometer. For the measurement of spectroscopic properties, the excitation and emission spectra for all samples were recorded on Shimadzu make RF-5301PC spectrophotofluorometer using solid sample holder. Emission and excitation spectra were recorded using a spectral slit width of 1.5 nm at room temperature. The co ordinations in the xy-chromaticity diagram are directly calculated from the fluorescent spectra (CIE 1931). All measurements were made at room temperature.

## III. RESULTS AND DISCUSSION

### A. X-ray Diffraction (XRD)

The comprehensive analysis of phase verification, structural parameters and crystalline structure of  $\text{La}_2\text{O}_2\text{S}$  phosphor was carried out by powder X-ray diffraction using diffractometer with  $\text{CuK}\alpha$  radiation ( $1.505 \text{ \AA}$ ) at operating voltage 40 KV, 30 mA and in the range  $2\theta$  of  $10 - 90$  degree, prepared by solid state diffusion method at room temperature. The XRD pattern of the synthesised phosphor material  $\text{La}_2\text{O}_2\text{S}$  is as shown in figure 1. It is found that acquired diffraction peaks of the phosphor prepared at  $1150^\circ\text{C}$  are in well agreement with the standard ICDD file No 71-2098. The sample was visually ensured and found to be physically stable (non-hygroscopic) and purely milky white in appearance. The obtained pattern reveals that  $\text{La}_2\text{O}_2\text{S}$  powder was formed with no contaminated phases, and implies the complete formation of the homogeneous phosphor material. Reasonably all the diffraction peaks can be indexed to the high crystallinity and high purity of  $\text{La}_2\text{O}_2\text{S}$ . The XRD pattern did not indicate the

existence of the constituents and other likely phases which are direct authentication of the formation of the phosphor.

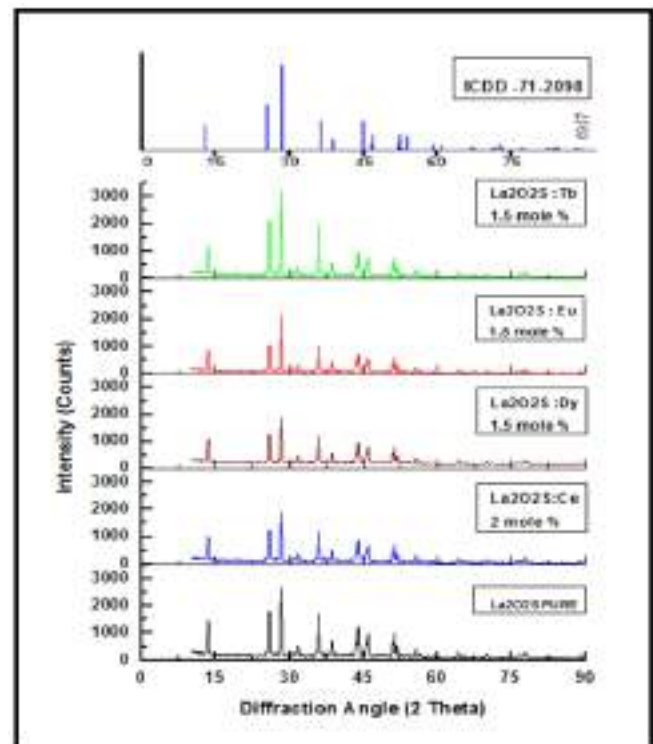


**Figure 1:** XRD pattern of  $\text{La}_2\text{O}_2\text{S}$  pure and  $\text{La}_2\text{O}_2\text{S}:\text{RE}^{3+}$  (Where  $\text{RE}^{3+} = \text{Ce}^{3+}, \text{Dy}^{3+}, \text{Eu}^{3+}$ , and  $\text{Tb}^{3+}$ ).

### B. Surface Morphology

Surface morphology of the phosphor was examined by using scanning electron microscopy (SEM, JED-2300) equipped with an energy dispersive spectrometry attached to the JEOL 6380A. SEM images provide the direct information about the size and typical shapes of the prepared samples. SEM micrographs of  $\text{La}_2\text{O}_2\text{S}$  and  $\text{Y}_2\text{O}_2\text{S}$  phosphors are shown in figure 2. The obtained micrographs show that the particles agglomerate and the average grain size diameter is in the range of 300–800 nm submicron range. It is clearly seen that the sample consists of microspheres with a slight agglomerate phenomenon and is irregularly spherical shaped morphology with a mean diameter of about 300–800 nm. The particle sizes strongly depend on the synthesis methods and synthesis conditions. The particle size and surface morphology which always affect the luminescent properties could be well controlled to improve the luminescent performance.

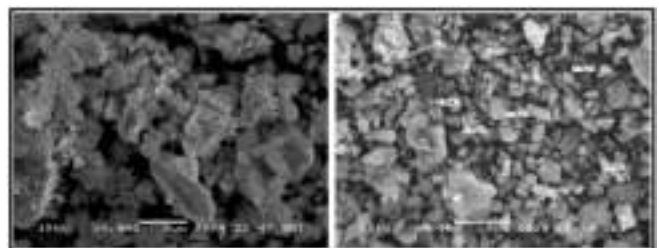


**Figure 2:** Scanning electron microscope (SEM) image of synthesized  $\text{La}_2\text{O}_2\text{S}$ .

### C. Crystal Structure

Crystal structure of  $\text{La}_2\text{O}_2\text{S}$  is shown in figure 3. The symmetry is trigonal and the space group is  $P3\bar{m}1$ . There is one formula unit per unit cell. The structure is very closely related to the A-type rare-earth oxide structure, the difference being that one of the three oxygen sites is occupied by a sulphur atom. Each metal atom seems to be bonded to four oxygen atoms and three sulphur atoms, to form a seven coordinated geometry with the oxygen and the metal in the same plane.

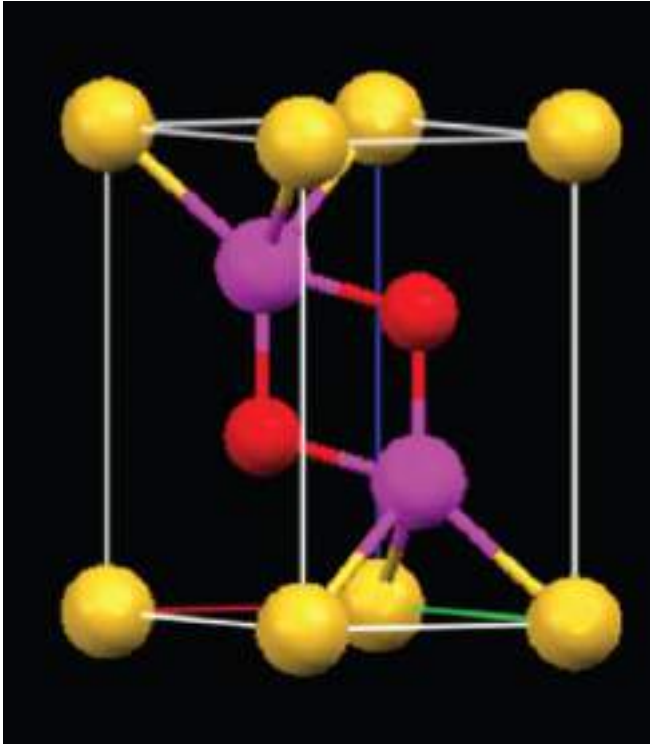


**Figure 3:** Crystal structure of  $\text{La}_2\text{O}_2\text{S}$ . La (Pink), O (red) and S (yellow). (For interpretation of the references to color in this figure legend, the reader is referred to the web version of this article.)

### D. FT-IR Analysis

Infrared spectroscopy exploits the fact that molecules have specific frequencies at which they rotate or vibrate corresponding to discrete energy levels. FT-IR spectra shown in figure 4 were recorded in the range of 500 to 4000  $\text{cm}^{-1}$  to show the functional groups for pure  $\text{La}_2\text{O}_2\text{S}$  sample. The weak absorption band after 3500  $\text{cm}^{-1}$  indicates the absorption of water from atmosphere. It is attributed to the stretching vibration of the O–H bond and the bending vibration of H–O–H from water molecules on the external surface of the samples during handling to record the spectra. It is a basic character of lanthanides to absorb water and carbon dioxide when they are exposed to atmosphere. For this reason storing of these compounds away from atmospheric condition is necessary [7–10]. The absorption band of cubic phase  $\text{La}_2\text{O}_2\text{S}$  appears at 544, 524 and 517  $\text{cm}^{-1}$ . A strong peak at 617  $\text{cm}^{-1}$  is related to La-S stretching mode. The weak peak at 880  $\text{cm}^{-1}$  can be assigned to S-O stretching group. The weak absorbance at 1454 and 1101  $\text{cm}^{-1}$  La-O are symmetric stretching mode.

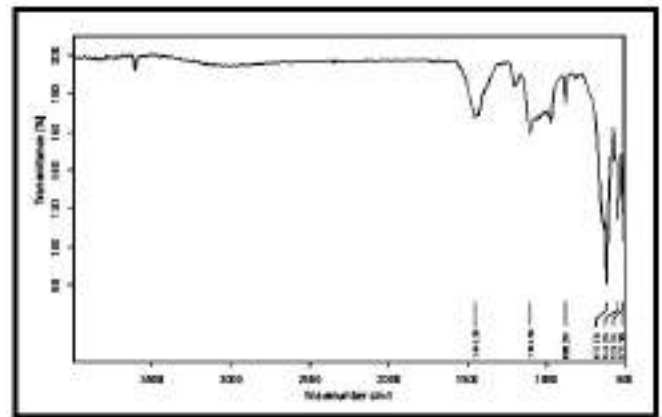


**Figure 4:** FT-IR spectrum of synthesized  $\text{La}_2\text{O}_2\text{S}$  phosphor.

### E. PL emission of $\text{RE}^{3+}$ in $\text{La}_2\text{O}_2\text{S}$ (Where $\text{RE}^{3+} = \text{Ce}^{3+}$ , $\text{Dy}^{3+}$ , $\text{Eu}^{3+}$ , and $\text{Tb}^{3+}$ )

#### i) PL emission of $\text{Ce}^{3+}$ in $\text{La}_2\text{O}_2\text{S}$

Figure 5 shows the excitation spectra in the 300–380 nm range and the emission spectra in the 350–500 nm range for samples  $\text{La}_{2(1-x)}\text{O}_2\text{S}:\text{Ce}_x$  (Where  $X = X = 0.5, 1, 2, 5,$  and 10 mole %) at room temperature. The excitation spectrum is obtained by monitoring the emission at 415 nm. The broad band is observed at around 340 nm at room temperature. The excitation band at 340 nm is assigned to the lowest 4f–5d transition for  $\text{Ce}^{3+}$  in the host lattice. A single 4f–5d excitation bands shows that the crystal field might not have split the excited state ( $^5\text{D}_1$ ) into more than one component indicating that  $\text{Ce}^{3+}$  ions occupy one lattice site [11].

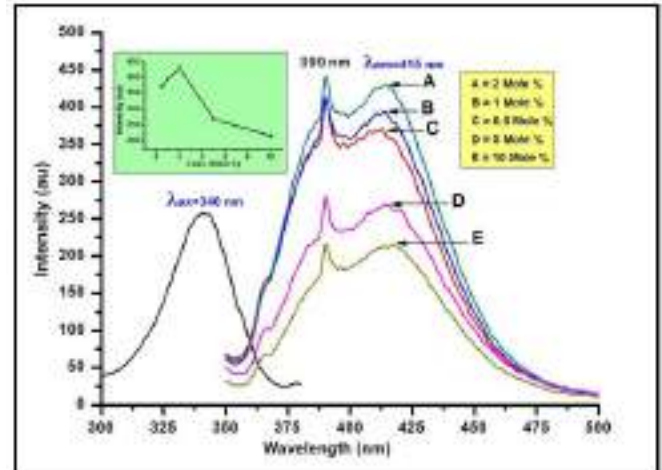


**Figure 5:** Excitation and emission spectra of synthesized  $\text{La}_2\text{O}_2\text{S}:\text{Ce}^{3+}$  phosphor.

The PL emission spectra of  $\text{Ce}^{3+}$  ions in  $\text{La}_2\text{O}_2\text{S}$  phosphors with different concentrations under the excitation of 340 nm wavelengths of light is as shown in figure 5. It shows a double humped characteristics with a sharp strong peak at 390 nm and a broad strong peak at 415 nm which are assigned to the 5d–4f transition of  $\text{Ce}^{3+}$  ions. It is clear that the emission bands correspond to the 5d–4f transition of  $\text{Ce}^{3+}$  ions. The characteristic emission of  $\text{Ce}^{3+}$  in the near UV region originates from parity allowed electric dipole transition between excited 5d and ground 4f states.

The 5d orbitals have their energy levels split by crystal effects into at least two sublevels of 5d. Due to spin orbit coupling the lowest sublevels of 5d can be further split into new components, as it is also the case for the ground state level 4f, which splits into the  $^2F_{5/2}$  and  $^2F_{7/2}$  sublevels. Thus excited state derived from the 5d state is sensitive to the crystal field and is coupled to the lattice vibrations which results in broad band emission rather than line emission. The energy structure of  $\text{Ce}^{3+}$  is such that localised multiphoton non-radiative relaxation and transfer cross relaxation quenching to other like ions are highly improbable and therefore the 5d luminescence of  $\text{Ce}^{3+}$  is strong and efficient. The crystal fields play an important role in 5d→4f transitions because 5d levels are outside the Ce atomic nucleus. M. Raukas et al.[12-13] suggested that luminescence efficiency was determined by small but crucial differences on the location of the lowest 5d level relative to the conduction band.

It may be induced by the difference in radius between  $\text{La}^{3+}$  ( $R = 103 \text{ pm}$ ) and  $\text{Ce}^{3+}$  ( $R = 100 \text{ pm}$ ), which will cause the distortion of lattice, the changes of the crystal field and the band gap. All these may cause the  $\text{Ce}^{3+}$  emission efficiency in  $\text{La}_2\text{O}_2\text{S}$  to change. It is also noticed that the peak positions of the emission bands for all  $\text{Ce}^{3+}$  doped  $\text{La}_2\text{O}_2\text{S}$  have not changed.

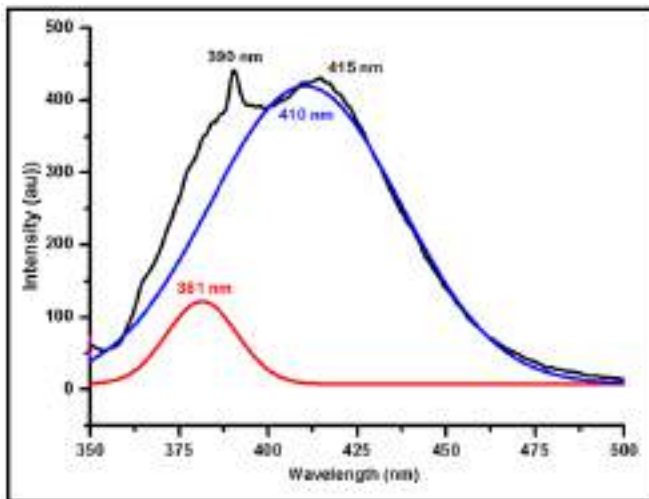


**Figure 6:** Gaussian fitted curve for synthesised  $\text{La}_2\text{O}_2\text{S}:\text{Ce}^{3+}$  phosphor.

The PL spectrum when further resolved by assuming a Gaussian profile for two emission peaks at 390 and 415 nm, attributed to the transitions of 5d to  $^2F_{5/2}$  and  $^2F_{7/2}$ , respectively, gives the peak at 381 nm and 410 nm as shown in figure 6. The energy difference between 381 and 410 nm was calculated to be  $\sim 1856 \text{ cm}^{-1}$ , which is close to theoretical value of  $\sim 2000 \text{ cm}^{-1}$ . The stoke's shift  $\Delta S$  ( $\lambda_{em}=390 \text{ nm} - \lambda_{ex}=340 \text{ nm}$ ) and ( $\lambda_{em}=415 \text{ nm} - \lambda_{ex}=340 \text{ nm}$ ) is found to be  $3771 \text{ cm}^{-1}$  and  $5257 \text{ cm}^{-1}$ , respectively. The stoke's shift is due to the strong electron lattice coupling in host. On the basis of configuration coordinate diagram, the excitation band is expanded and therefore the equilibrium of the ground state might have displaced [14].

Various models have been proposed to explain the presence or absence of luminescence. Among them, one-dimensional configuration curve has been most widely

used. To illustrate how radiative processes of  $\text{Ce}^{3+}$  in  $\text{La}_2\text{O}_2\text{S}$  phosphor works, a partial electronic energy levels and energetic structure along with configuration co-ordinate diagram are shown in figure 7.

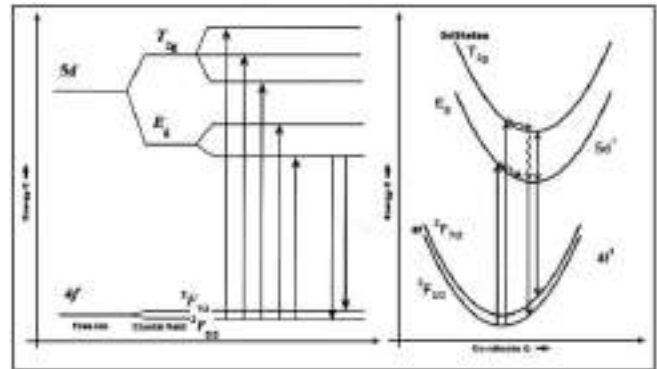


**Figure 7:** Schematic illustration of partial energy levels and configurational coordinate diagram of  $\text{Ce}^{3+}$ .

In partial electronic structure, the 4f ground state of  $\text{Ce}^{3+}$  ion is split into  $^2F_{7/2}$  and  $^2F_{5/2}$  levels due to spin orbit coupling. Its lowest excited state is the 5d band that is easily affected by the crystal field. The crystal field splitting of 5d usually forms 2 to 5 configurations.  $\text{Ce}^{3+}$  fluorescence is related to an electric dipole 4f→5d transition [15]. The transition is parity and spin allowed. When  $\text{Ce}^{3+}$  is placed in a crystal, the emission occurs from ultraviolet to visible band depending on the particular compound or host symmetry. It is because the 5d state of  $\text{Ce}^{3+}$  is strongly affected by three interrelated effects: crystal field splitting (crystal field effect), covalence (nephelauxetic effect) and Stokes shift.[16] Therefore, the luminescence centre is a good candidate as activators in phosphors with the designed excitation and emission wavelengths because luminescence positions can be flexibly adjusted.

In configuration co-ordinate diagram, the potential energy of the luminescent centre in the crystal lattice is plotted as functions of the configuration coordinate Q. The quantity Q represents the distance between rare earth ion and its surrounding ions. Optical transitions are represented vertically on the configuration co-ordinate diagrams, because they occur rapidly compared with nuclear motions, As we can see, ground and excited states take form of parabola potential wells. The two lowest parabolas represent the ground electronic configuration  $4f_1$  by spin-orbit interaction into  $^2F_{5/2}$  (the ground state) and  $^2F_{7/2}$  (the first excited state). The lowest states of excited electronic configuration  $5d_1$  are represented by two higher parabolas. Electron-lattice interaction in the excited electronic manifold causes the shift of the respective parabolas in the configurational space. In this diagram, the potential energy of the luminescent centre  $\text{Ce}^{3+}$  is plotted on the vertical axis and the value of single parameter describing the effective displacement of the ion surrounding the activator, Q, is plotted on the horizontal axis. Promotion of the inner 4f electron to the outer 5d states perturbs the surrounding ions, the lattice relaxes, and the potential energy curve changes as shown below in figure 7.

The good adaptability of the position of the 4f–5d absorptions and the corresponding emissions make Ce<sup>3+</sup> an important ingredient in light emitting materials. The respective excitation and emission pathways are indicated in figure by arrows [17, 18].

ii) PL emission of Dy<sup>3+</sup> in La<sub>2</sub>O<sub>2</sub>S

The photoluminescence excitation and emission spectra of the La<sub>2</sub>(1-x)O<sub>2</sub>S: Dy<sub>x</sub> (Where X = 0.2, 0.5, 1, 1.5, 2 mole %) optoelectronics phosphor at room temperature is shown in figure 8. The excitation spectrum in the range 350 - 400 nm consists of the f-f transition of the Dy<sup>3+</sup> ion. The excitation peaks observed at 351 nm, 367 nm and 388 nm are due to transitions from ground level, <sup>6</sup>H<sub>15/2</sub> to higher energy levels <sup>4</sup>G<sub>11/2</sub>, <sup>4</sup>I<sub>15/2</sub>, and <sup>4</sup>F<sub>9/2</sub> of Dy<sup>3+</sup> ion, respectively. Amongst these three near UV excitation peaks, though the emission intensity is larger for λ<sub>ex</sub>=351 nm and λ<sub>ex</sub>=367 nm as shown in figure 8, we chose 388 nm as excitation wavelength because it is more suitable for solid state lighting [19, 20].

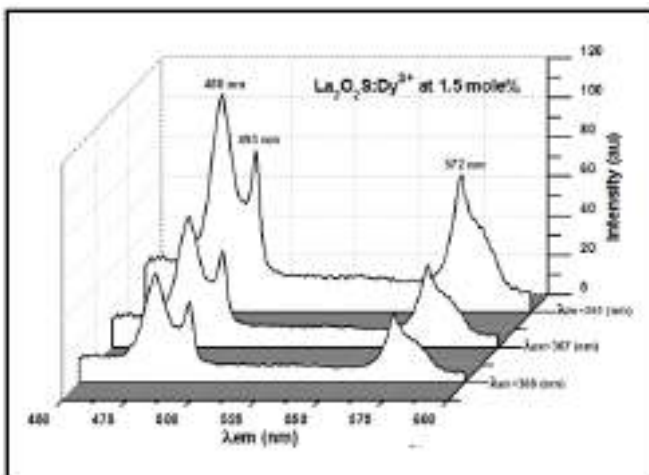


Figure 8: Emission spectra of synthesized La<sub>2</sub>O<sub>2</sub>S:Dy<sup>3+</sup> phosphor at 1.5 mole% for various excitation wavelengths.

La<sub>2</sub>O<sub>2</sub>S:Dy<sup>3+</sup> phosphor exhibits characteristics emission bands centred at 480 nm and yellow band at 572 nm originating from Dy<sup>3+</sup> ion under the excitation of 388 nm. Dy<sup>3+</sup> emission at around 480 nm (<sup>4</sup>F<sub>9/2</sub> → <sup>6</sup>H<sub>15/2</sub>) is due to magnetic dipole moment and 576 nm (<sup>4</sup>F<sub>9/2</sub> → <sup>6</sup>H<sub>13/2</sub>) is due to electric dipole moment. The ionic radius of Dy<sup>3+</sup> (91.2 pm) is much smaller than that La<sup>3+</sup> (103 pm). Therefore, most of the Dy<sup>3+</sup> ions may have entered the lattice with few of them located on the surface of the La<sub>2</sub>O<sub>2</sub>S:Dy<sup>3+</sup> host crystal due to the porosity of the structure. From the PL spectra it is clear that, energy transfer is possible from the host to the Dy<sup>3+</sup> activator ions in La<sub>2</sub>O<sub>2</sub>S:Dy<sup>3+</sup> host lattice. The inset of figure 9, shows the dependence of the luminescence intensity with the Dy<sup>3+</sup> concentration. The emission spectrum shape does not vary with the Dy<sup>3+</sup> concentration but the luminescence intensity changes more significantly. It is found that the emission intensity of Dy<sup>3+</sup> increases with an increase of dopant ion concentration. It reaches to a maximum value at 1 mole %, and then decreases with an increase of dopant at 2 mole % due to self-quench processes. Such near UV

excitation in phosphors host may be helpful for white-LEDs [21 – 24].

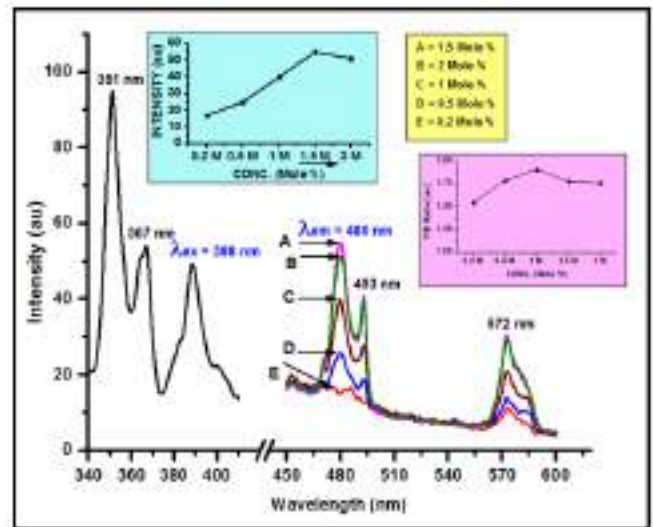


Figure 9: Excitation and emission spectra of synthesised La<sub>2</sub>O<sub>2</sub>S:Dy<sup>3+</sup> phosphor.

The emission intensity of yellow to blue (Y/B) ratio is depicted in inset of figure 9. By carefully observing the emission spectra it is found that the emission intensity of yellow to blue (Y/B) ratio is less than 1. This shows that Dy<sup>3+</sup> ions occupy the site with inversion symmetry predominantly [25].

The partial energy levels and energetic structure and radiative processes in Dy<sup>3+</sup> are presented in a configurational coordinate diagram in figure 10. In the figure the <sup>6</sup>H and <sup>6</sup>F states of the ground multiplet and the <sup>4</sup>F, <sup>4</sup>I, and <sup>4</sup>G states of the <sup>4</sup>f<sub>9</sub> electronic configuration, are presented. Under excitation through <sup>4</sup>f<sub>9</sub> transitions in the Dy<sup>3+</sup> ion at 388 nm the system can relax nonradiatively to the <sup>4</sup>F<sub>9/2</sub> state and then yield Dy<sup>3+</sup> emission. The respective emission pathways are indicated in figure by arrows.

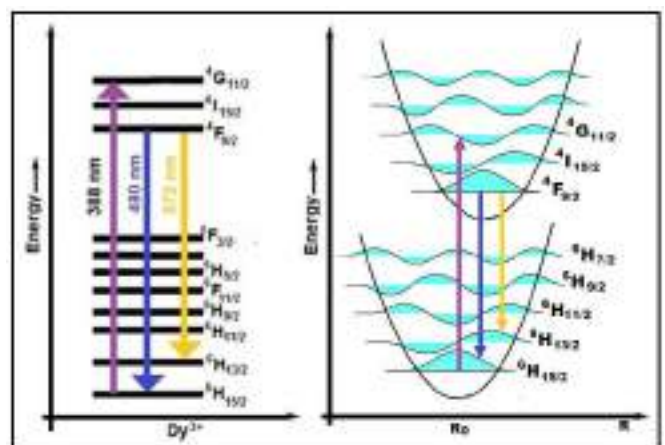


Figure 10: Schematic illustration of partial energy levels and configurational coordinate diagram of Dy<sup>3+</sup>.

iii) PL emission of  $\text{Eu}^{3+}$  in  $\text{La}_2\text{O}_2\text{S}$

The PL excitation spectra of  $\text{La}_{2(1-x)}\text{O}_2\text{S}:\text{Eu}_x$  (Where X = 0.2, 0.5, 1, 1.5, 2 mole %) optoelectronics phosphor at room temperature is shown in figure 11. The excitation spectrum at 396 nm is characteristic of W-LED excitation in the near UV range. The sharp excitation peaks between 350 and 400 nm are due to the typical f-f transition of  $\text{Eu}^{3+}$ . The strongest line absorption in the excitation spectrum is located at 396 nm, which is resulting from the  ${}^7\text{F}_0 \rightarrow {}^5\text{L}_6$  transition [26, 27].

The  $\text{La}_2\text{O}_2\text{S}:\text{Eu}^{3+}$  phosphor has one sharp orange emission bands at 590 nm and weak bands at 615 nm due to characteristics emission of  $\text{Eu}^{3+}$  ion, as shown in figure 11, observed due to the  ${}^5\text{D}_0 \rightarrow {}^7\text{F}_{i=0,1,2,3,4}$  transitions of  $\text{Eu}^{3+}$  ions. The emission band at 590 nm is more prominent and corresponds to the magnetic dipole transition ( ${}^5\text{D}_0 \rightarrow {}^7\text{F}_1$ ) of  $\text{Eu}^{3+}$  ion whereas the emission band at 615 nm is less prominent and is due to electric dipole transition ( ${}^5\text{D}_0 \rightarrow {}^7\text{F}_2$ ) of  $\text{Eu}^{3+}$  ion. These two emission peaks are obtained due to crystal field splitting of  ${}^5\text{D}_0$  level to  ${}^7\text{F}_j$  ground state levels. The luminescence spectra of  $\text{Eu}^{3+}$  ion is slightly influenced by surrounding ligands of the host material because the transition of  $\text{Eu}^{3+}$  involve only a redistribution of electrons within the inner 4f subshells. The relative intensities of the 590 nm ( ${}^5\text{D}_0 \rightarrow {}^7\text{F}_1$ ) and 615 nm ( ${}^5\text{D}_0 \rightarrow {}^7\text{F}_2$ ) emissions are very sensitive to the site that  $\text{Eu}^{3+}$  ions occupied. As for  $\text{La}_2\text{O}_2\text{S}:\text{Eu}^{3+}$  particles, the  $\text{Eu}^{3+}$  ions may have occupied the La ion in host lattice and are at a site with inversion symmetry in the  $\text{La}_2\text{O}_2\text{S}$  matrix and thus dominating the emission centred at 593 nm corresponding to the  ${}^5\text{D}_0 \rightarrow {}^7\text{F}_1$  magnetic dipole transition. Thus,  $\text{La}_2\text{O}_2\text{S}:\text{Eu}^{3+}$  phosphor may be promising candidates for the development of white-LEDs [28 – 33].

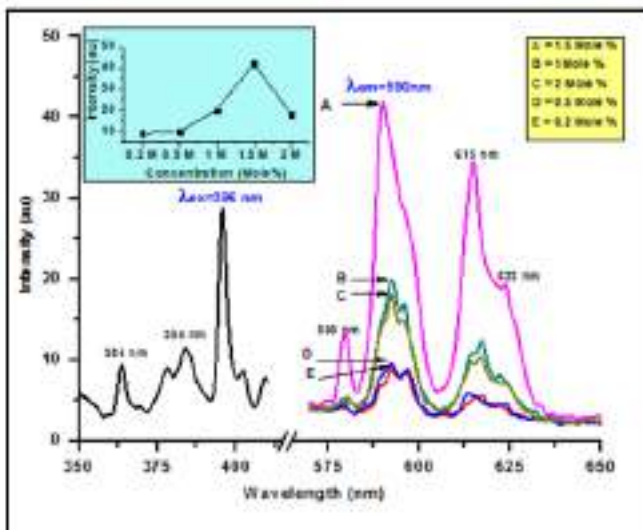


Figure 6: Excitation and emission spectra of  $\text{La}_2\text{O}_2\text{S}:\text{Eu}^{3+}$  phosphor.

The partial energy levels and energetic structure and radiative processes in  $\text{Eu}^{3+}$  are presented in a configurational coordinate diagram in figure 12. In the figure the  ${}^7\text{F}_j$  states for  $J= 0,1,2,3,4,5,6$  of the ground multiplet and the excited electronic states  ${}^5\text{D}_0, {}^5\text{D}_1, {}^5\text{D}_2, {}^5\text{D}_3$  and  ${}^5\text{L}_6$  states of the  ${}^4\text{f}_6$  electronic configuration, are presented. Under excitation through  ${}^4\text{f}_6$  transitions in the  $\text{Eu}^{3+}$  ion at 396 nm the system can relax nonradiatively to the  ${}^5\text{D}_0$  state and then yield  $\text{Eu}^{3+}$

emission. The respective emission pathways are indicated in figure by arrows.

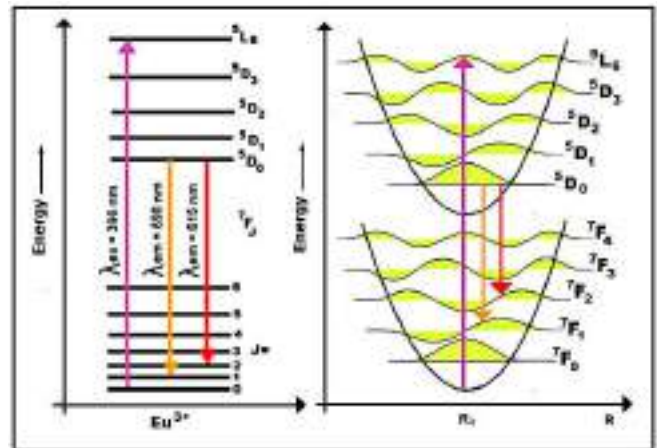


Figure 12: Schematic illustration of partial energy levels and configurational coordinate diagram of  $\text{Eu}^{3+}$ .

iv) PL emission of  $\text{Tb}^{3+}$  in  $\text{La}_2\text{O}_2\text{S}$

Figure 13 shows the excitation spectra in the 340–400 nm range and the emission spectra in the 450–650 nm range for samples  $\text{La}_{2(1-x)}\text{O}_2\text{S}:\text{Tb}_x$  (Where X = 0.2, 0.5, 1, 1.5, 2 mole %) at room temperature.

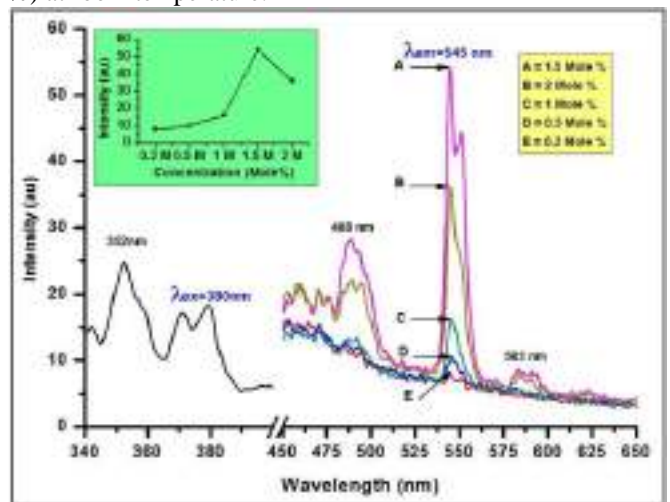
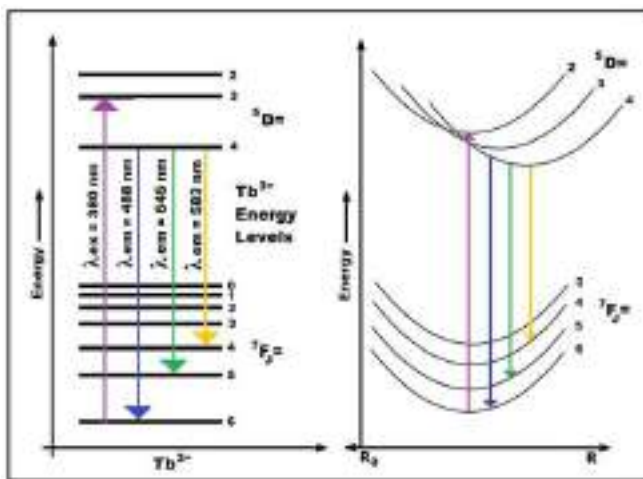


Figure 13: Excitation and emission spectra of  $\text{La}_2\text{O}_2\text{S}:\text{Tb}^{3+}$  phosphor.

The overall excitation spectrum of  $\text{Tb}^{3+}$  can be divided into two parts. One, in the wavelength range 220 nm–310 nm comprising of  ${}^4\text{f}_8 \rightarrow {}^4\text{f}_7^5\text{d}_1$  transitions and other part of the excitation spectrum, in the range 310 nm–500 nm which stands for  ${}^4\text{f}_8 \rightarrow {}^4\text{f}_8$  transitions of the  $\text{Tb}^{3+}$  ions [34]. There are several excitation peaks in the 340 to 390 nm region corresponding to transitions between  ${}^7\text{F}_6$  and the various excited states belonging to the  ${}^4\text{f}_8$  electronic configuration of  $\text{Tb}^{3+}$  ions [35]. The excitation peaks at 352 nm ( ${}^7\text{F}_6 \rightarrow {}^5\text{L}_9$ ), 371 nm ( ${}^7\text{F}_6 \rightarrow {}^5\text{G}_5$ ) and 380 nm ( ${}^7\text{F}_6 \rightarrow {}^5\text{G}_6$ ) due to forbidden 4f-4f transition of  $\text{Tb}^{3+}$  ion. Though there were significant absorption in the near-UV region and the excitation at 352 nm has highest intensity, we have chosen  $\lambda_{\text{ex}}=380$  nm as it is more suitable near UV excitation for white LED and therefore  $\text{La}_2\text{O}_2\text{S}:\text{Tb}$  had potential to be used as near-UV LED phosphors [36].



The emission spectrum of  $\text{La}_2\text{O}_2\text{S}:\text{Tb}$  is determined by the transitions of electrons from an upper ( $^5\text{D}_3$ ) and a lower ( $^5\text{D}_4$ ) excited level to the level of the multiplet term  $^7\text{F}_J$  ( $J = 0, 1, 2, 3, 4, 5, 6$ ) levels of the  $^4\text{f}_8$  configuration [37, 38]. The emission of terbium doped phosphor is mainly in the green due to transitions  $^5\text{D}_4 \rightarrow ^7\text{F}_J$  and the blue emission contributes to the emission from the higher level transitions  $^5\text{D}_3 \rightarrow ^7\text{F}_J$ . **Figure 13** shows the emission spectra of  $\text{La}_2\text{O}_2\text{S}:\text{Tb}^{3+}$  phosphors under the excitation wavelength of 380 nm. The emission peaks were found at 488, 545, and 583 nm, which were assigned to the  $^5\text{D}_4 \rightarrow ^7\text{F}_J$  ( $J = 6, 5, 4$ ) transition of  $\text{Tb}^{3+}$  ions [9]. As expected, the spectral shift was not observed because the 4f shell of  $\text{Tb}^{3+}$  was well shielded by 5s and 5p shells. Moreover, the emission from  $^5\text{D}_3 \rightarrow ^7\text{F}_J$  level are quenched by the cross relaxation ( $\text{Tb}^{3+} (^5\text{D}_3) + \text{Tb}^{3+} (^7\text{F}_6) \rightarrow \text{Tb}^{3+} (^5\text{D}_4) + \text{Tb}^{3+} (^7\text{F}_1)$ ) [39, 40]. The cross relaxation process produces the rapid population of the  $^5\text{D}_4$  level at the expense of  $^5\text{D}_3$ , resulting in a strong emission from the  $^5\text{D}_4$  to the  $^7\text{F}_J$  level. Generally, the cross relaxation is observed at higher  $\text{Tb}^{3+}$  concentration, which made good agreement with the results in our case.



**Figure 14:** Schematic illustration of partial energy levels and configurational coordinate diagram of  $\text{Tb}^{3+}$ .

The luminescent mechanism of phosphor is due to competition between the optical activation of  $\text{Tb}^{3+}$  ions which results in increase of PL intensity and the clustering of  $\text{Tb}^{3+}$  causes concentration quenching. At lower concentration of concentration, the PL intensity of 545 nm ( $^5\text{D}_4 \rightarrow ^7\text{F}_5$ ) and 488 nm ( $^5\text{D}_4 \rightarrow ^7\text{F}_6$ ) emissions decreases with increase of  $\text{Tb}^{3+}$  ion concentration. As the concentration of  $\text{Tb}^{3+}$  exceed the critical concentration, distance between  $\text{Tb}^{3+}$  ions become shorter, which cause activator to form pairs and thus results in concentration quenching. The emission intensity reached its optimum doping concentration at about 1.5 mole% in the  $\text{La}_2\text{O}_2\text{S}:\text{Tb}^{3+}$  phosphors.

The partial energy levels and energetic structure and radiative processes in  $\text{Tb}^{3+}$  are presented in a configurational coordinate diagram in **figure 14**. In the **figure** the  $^7\text{F}_J$  states  $^7\text{F}_3$ ,  $^7\text{F}_4$ ,  $^7\text{F}_5$ , and  $^7\text{F}_6$  of the ground multiplet and the  $^5\text{D}_2$ ,  $^5\text{D}_3$  and  $^5\text{D}_4$  states of the  $^4\text{f}_8$  electronic configuration, are presented. Under excitation through  $^4\text{f}_8$  transitions in the  $\text{Tb}^{3+}$  ion at 380 nm the system can relax nonradiatively to the  $^5\text{D}_4$  state and

then yield  $\text{Tb}^{3+}$  emission. The respective emission pathways are indicated in **figure** by arrows [41].  $\text{Tb}^{3+}$ , the first mechanism is dominant in the luminescent process and the PL intensity increases with the increase in concentration of  $\text{Tb}^{3+}$ . The inset of **figure 13** show the relative PL intensities of 545 nm ( $^5\text{D}_4 \rightarrow ^7\text{F}_5$ ) and 488 nm ( $^5\text{D}_4 \rightarrow ^7\text{F}_6$ ) emissions under 380 nm excitation. Up to 1.5 mole% concentration of  $\text{Tb}^{3+}$  ion the PL intensity of 545 nm ( $^5\text{D}_4 \rightarrow ^7\text{F}_5$ ) and 488 nm ( $^5\text{D}_4 \rightarrow ^7\text{F}_6$ ) emission increases with increase of  $\text{Tb}^{3+}$  ion concentration above 1.5 mole % .

**F. Chromatic Properties**

The **figure 15** shows the Commission International de l'Eclairage (CIE) chromaticity co-ordinates of the prepared phosphor  $\text{La}_2\text{O}_2\text{S}:\text{RE}^{3+}$  phosphor (Where  $\text{RE}^{3+} = \text{Ce}^{3+}, \text{Dy}^{3+}, \text{Eu}^{3+}$  and  $\text{Tb}^{3+}$ ). The chromatic co-ordinates (X, Y) are calculated using the colour calculator radiant imaging software and are summarized in following **table 1**.

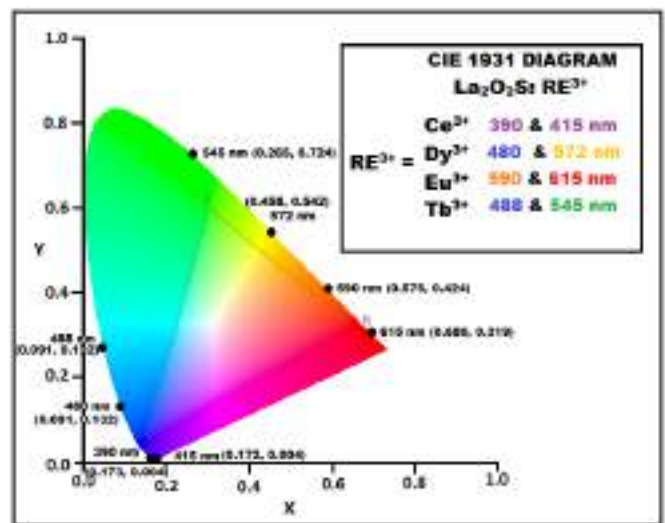


**Figure 15:** Chromatic graph of  $\text{La}_2\text{O}_2\text{S}:\text{RE}^{3+}$  phosphor (Where  $\text{RE}^{3+} = \text{Ce}^{3+}, \text{Dy}^{3+}, \text{Eu}^{3+}$  and  $\text{Tb}^{3+}$ ).

**G. Luminescence and energy transfer in  $\text{La}_2\text{O}_2\text{S}:\text{Tb}^{3+}, \text{Ce}^{3+}$**

In this section, PL characteristics of  $\text{La}_2\text{O}_2\text{S}$  phosphor with doubly doped  $\text{Tb}^{3+}$  and  $\text{Ce}^{3+}$  is investigated. Energy transfer from  $\text{Ce}^{3+}$  to  $\text{Tb}^{3+}$  is also discussed. The  $\text{Tb}^{3+}$  and  $\text{Ce}^{3+}$  are two important rare earth ions, which have been used to produce green and blue emission [42]. In addition,  $\text{Ce}^{3+}$  is also an efficient sensitizer to  $\text{Tb}^{3+}$ , due to its allowed optical transition from 4f to 5d and broad emission. The broad emission of  $\text{Ce}^{3+}$  creates high possibility overlapping with the excitation band of  $\text{Tb}^{3+}$  which gives bright green emission suitable for lighting and display devices.

Emission and excitation spectra of the  $\text{La}_2\text{O}_2\text{S}:\text{Ce}^{3+}$  and  $\text{La}_2\text{O}_2\text{S}:\text{Tb}^{3+}$  phosphor is already discussed and shown in



**Table I:** CIE Co-ordinates of  $\text{La}_2\text{O}_2\text{S}:\text{RE}^{3+}$  phosphor (Where  $\text{RE}^{3+} = \text{Ce}^{3+}, \text{Dy}^{3+}, \text{Eu}^{3+}$  and  $\text{Tb}^{3+}$ ).

PHOSPHOR	EXCITATION (nm)	STRONG EMISSION (nm)	(X,Y) COORDINATE	COLOUR REGION
$\text{La}_2\text{O}_2\text{S}:\text{Ce}^{3+}$	340	390 415	(0.173, 0.004) (0.172, 0.004)	UV UV
$\text{La}_2\text{O}_2\text{S}:\text{Dy}^{3+}$	397	480 572	(0.091, 0.132) (0.458, 0.542)	Blue Yellow
$\text{La}_2\text{O}_2\text{S}:\text{Eu}^{3+}$	396	590 615	(0.575, 0.424) (0.680, 0.319)	Orange Red
$\text{La}_2\text{O}_2\text{S}:\text{Tb}^{3+}$	380	488 545	(0.091, 0.132) (0.265, 0.724)	Blue Green

figure 5 and 13 respectively. The emission of  $\text{Ce}^{3+}$  includes emission bands of the transitions of 5d-excited state to  $^2\text{F}_{7/2}$  and  $^2\text{F}_{5/2}$  states. The emission spectrum observed in  $\text{La}_2\text{O}_2\text{S}:\text{Ce}^{3+}$  consist of emission peaking at 390 and 415 nm under excitation wavelength of 340 nm which corresponds to the transitions from ground state of  $\text{Ce}^{3+}$  to its field splitting levels of  $^5\text{d}_1$  states [43]. The emission spectra of  $\text{La}_2\text{O}_2\text{S}:\text{Tb}^{3+}$  phosphor consist of emission peaks at 488, 545, 583 nm, which are assigned to the  $^5\text{D}_4$  to  $^7\text{F}_j$  ( $J=6, 5, 4$ ) transitions of singly doped  $\text{Tb}^{3+}$  in  $\text{La}_2\text{O}_2\text{S}$  when excited at near UV 380 nm wavelength. Some emissions from  $^5\text{D}_3$  to  $^7\text{F}_j$  ( $J=5, 4, 3, 2, 1, 0$ ) are also found from 400 to 485 nm in  $\text{Tb}^{3+}$  singly doped sample [44].

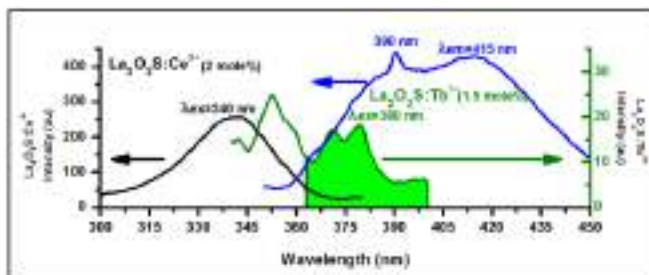


**Figure 16:** Excitation & Emission spectra of single doped  $\text{La}_2\text{O}_2\text{S}:\text{Ce}^{3+}$  (2 M%) and Excitation spectrum of  $\text{La}_2\text{O}_2\text{S}:\text{Tb}^{3+}$  (1.5 M%) showing strong overlap between  $\text{Ce}^{3+}$  emission and  $\text{Tb}^{3+}$  absorption in the range 300 to 450 nm.

Energy transfer is controlled by luminescent kinetics, which is affected by energy level, lifetime, distance between co-dopants, etc. One of the dopant is called as activator from where the emission takes place and other is sensitizer, which will improve the luminescence efficiency of activator emission.  $\text{Ce}^{3+}$  to  $\text{Tb}^{3+}$  energy transfer process in different host matrices is well known [45, 46]. Broad band emitters are often used to sensitize the luminescence of RE ions. Efficient energy transfer from the broad (i.e.,  $\text{Ce}^{3+}$ ) to the narrow-line emitter (i.e.,  $\text{Tb}^{3+}$ ) is possible only between nearest neighbours in the crystal lattice and optimal spectral overlap. If the spectral overlap is small, only partial energy transfer is possible.

As shown in figure 16,  $\text{Ce}^{3+}$  doped sample exhibits broad band emission from 360 - 450 nm, while  $\text{Tb}^{3+}$  doped sample shows an excitation band ranging from 345 to 400 nm. It means that, there is a strong overlap between  $\text{Ce}^{3+}$  emission and  $\text{Tb}^{3+}$  excitation in the range of 360- 400 nm. Therefore, it

is expected that an efficient energy transfer can occur from  $\text{Ce}^{3+}$  to  $\text{Tb}^{3+}$ .

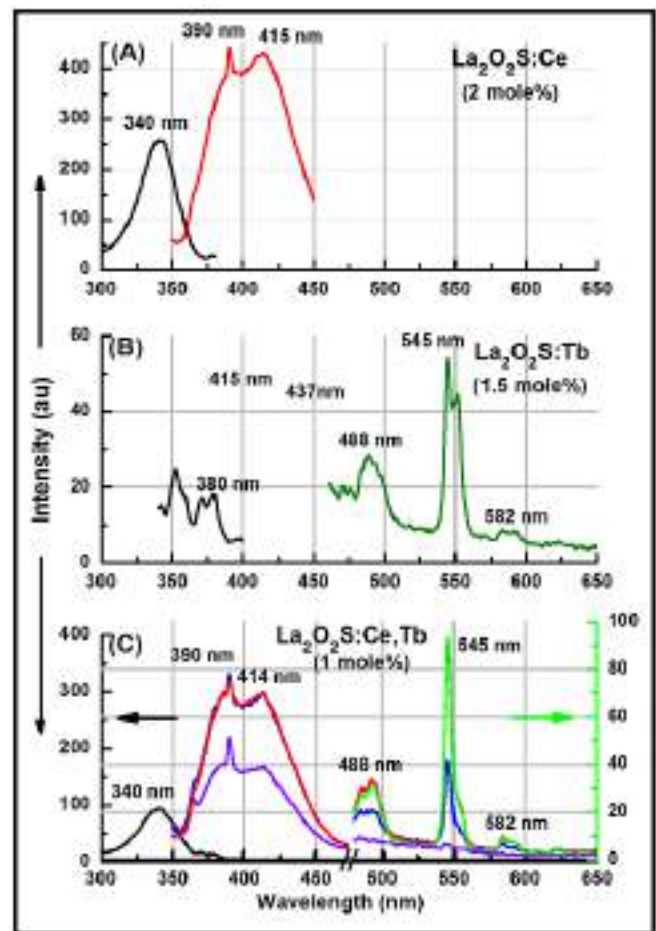


**Figure 17:** Excitation and emission spectra of the single-doped and co-doped samples, (A)  $\text{La}_2\text{O}_2\text{S}:\text{Ce}^{3+}$ , (B)  $\text{La}_2\text{O}_2\text{S}:\text{Tb}^{3+}$  and (c)  $\text{La}_2\text{O}_2\text{S}:\text{Ce}^{3+} \rightarrow \text{Tb}^{3+}$ .

Figure 17 (A) shows the excitation and emission spectra of  $\text{La}_2\text{O}_2\text{S}:\text{Ce}^{3+}$  at 2 mole%. Figure 17 (B) shows the excitation and emission spectra of  $\text{La}_2\text{O}_2\text{S}:\text{Tb}^{3+}$  at 1.5 mole%. Figure 17 (C) depicts the excitation and emission spectra of  $\text{La}_2\text{O}_2\text{S}:\text{Ce}^{3+} \rightarrow \text{Tb}^{3+}$  sample. The excitation spectrum is monitored at  $\lambda_{em}=545\text{nm}$ . The broad excitation band at 340 nm is in agreement with the  $\text{Ce}^{3+}$  solely doped system.

The emission spectra in Figure 17 (C) indicate the high light output of  $Tb^{3+}$  which actually comes from the energy transfer process from  $Ce^{3+}$  to  $Tb^{3+}$ . The optimal excitation wavelength for  $Ce^{3+}$  is 340 nm light excitation but not for  $Tb^{3+}$ . In  $La_2O_2S$  phosphor,  $Ce^{3+}$  not only exhibit the emission at 390 and 414 nm, but also due to energy transfer  $Tb^{3+}$  radiates the strong green emission band at 545 nm along with weak emission at 488 and 582 nm. The  $Ce^{3+}$  ion first absorbs UV light at 340 nm. An electron is pumped to 5d level, and then non-radiatively relaxes to the lowest component of 5d level finally decaying to  $^2F_{5/2}$  and  $^2F_{7/2}$  levels by radiative process emitting photons at 390 and 414 nm. As the value of energy level of excited 5d state of  $Ce^{3+}$  is close to the  $^5D_3$  and other levels of  $Tb^{3+}$  ions, the energy transfers from  $Ce^{3+}$  to  $Tb^{3+}$  ions would have been occurred, promoting it from  $^7F_6$  ground state to  $^5D_3$  and other levels of  $Tb^{3+}$  ion. Then the excited  $Tb^{3+}$  ion relaxes, non-radiatively, to the  $^5D_4$  levels and gives the strong emission of  $Tb^{3+}$  ( $^5D_4 \rightarrow ^7F_1$ ). Figure 18 shows schematic energy level diagram indicating  $Ce^{3+} \rightarrow Tb^{3+}$  energy transfer in  $La_2O_2S$ .

For a better understanding, an energy level model that explains the energy transfer from  $Ce^{3+} \rightarrow Tb^{3+}$  is illustrated in figure 18. It shows interaction between the  $^5D$  state of  $Ce^{3+}$  and the  $^5D$  state of  $Tb^{3+}$ . The  $^5D_4 \rightarrow ^7F_6$  (blue) and  $^5D_4 \rightarrow ^7F_5$  (green) occurs at 488 nm and 588 nm, respectively. As a result, the energy transfer from  $Ce^{3+}$  to  $Tb^{3+}$  is allowed by the law of conservation of energy. Thus it illustrates that both blue emission and green emission of  $Tb^{3+}$  ions could be obtained in the  $La_2O_2S$  host, which is the base of multicolour emission under the excitation of UV light in the present system.

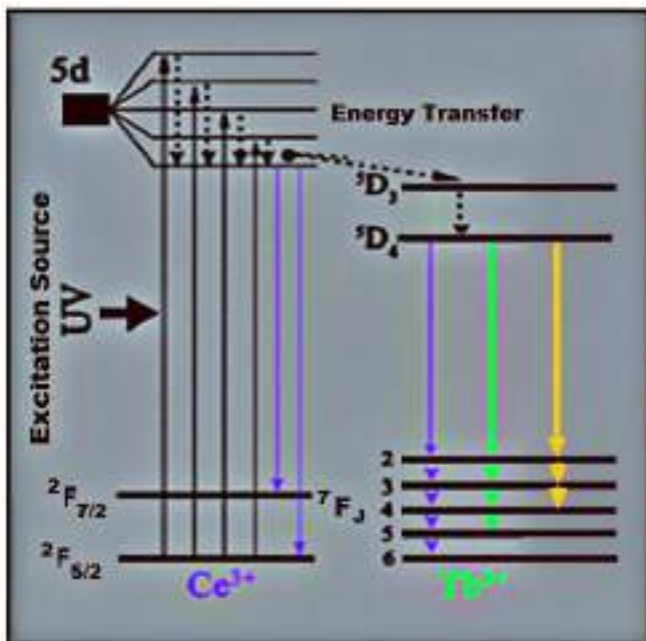


Figure 18: Schematic energy level diagram indicating  $Ce^{3+} \rightarrow Tb^{3+}$  energy transfer in  $La_2O_2S$ .

The luminescence colours of  $La_2O_2S:Ce^{3+} \rightarrow Tb^{3+}$  phosphors excited at 340 nm are characterized by Commission International de l'Eclairage (CIE) chromaticity diagram and is shown in figure 19. The chromaticity coordinate  $La_2O_2S:Ce^{3+} \rightarrow Tb^{3+}$  phosphors is calculated to be

(0.265, 0.724) for 415 nm and (0.265, 0.724) for 545 nm. The line connecting the chromaticity point passes nearly from white region. It is worthwhile to notice that by combining the emission band of  $Ce^{3+}$  ions at blue region and the emission band of  $Tb^{3+}$  ions at green region, white light emission may be achieved.

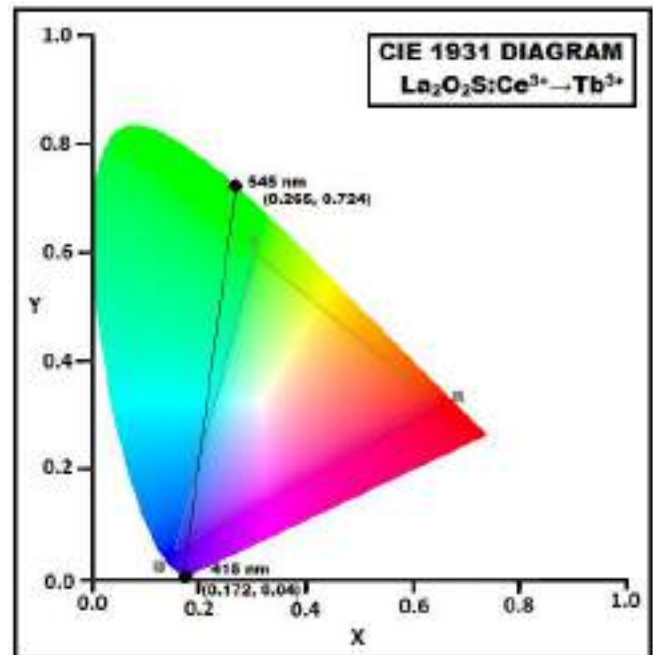


Figure 19: Chromatic graph of  $La_2O_2S:Ce^{3+} \rightarrow Tb^{3+}$  phosphors phosphor excited near UV excitation.

#### IV. CONCLUSION

The  $La_2O_2S:RE^{3+}$  (Where  $RE^{3+} = Ce^{3+}, Dy^{3+}, Eu^{3+}$  and  $Tb^{3+}$ ) optoelectronics phosphor has been prepared by the solid state flux diffusion method. PL properties in the near UV and visible region which are characteristics for optoelectronic devices are studied. XRD analysis is carried out to check phase purity of the prepared optoelectronics phosphor. SEM analysis show agglomerates ranging from few microns to a few tens of microns with highly porous morphology of the synthesised phosphor. FT-IR spectra were recorded to show the functional groups for pure  $La_2O_2S$  sample. CIE is carried out to check colour quality of the prepared phosphor. The developed  $La_2O_2S:RE^{3+}$  (Where  $RE^{3+} = Ce^{3+}, Dy^{3+}, Eu^{3+}$  and  $Tb^{3+}$ ) phosphor has been excited in near UV range which is desirable characteristics for commercially available W-LED. The developed phosphor emits in the blue, yellow, green and red region. Hence it has potential to be used in phosphor converted LED as a primary colour emitter in 3 band pc-LED or red spectrum enhancer in yellow phosphor converted white LED and therefore our results indicate that prepared phosphor may be a promising candidates for white LEDs. Cross relaxation process led to non-radiative quenching therefore the emission intensity of  $RE^{3+}$  ions decreased with increasing amount of doped  $RE^{3+}$  ions.

To investigate the energy transfer from  $Ce^{3+}$  to  $Tb^{3+}$  ions,



# Synthesis and Luminescence Properties of $\text{La}_2\text{O}_2\text{S}:\text{RE}^{3+}$ ( $\text{RE}^{3+} = \text{Ce}^{3+}$ , $\text{Dy}^{3+}$ , $\text{Eu}^{3+}$ and $\text{Tb}^{3+}$ ) Submicron Size Phosphors for Lamp Industry

the emission spectra of  $\text{La}_2\text{O}_2\text{S}:\text{Ce}^{3+} \rightarrow \text{Tb}^{3+}$  phosphors under excitation wavelength 340 nm were measured. The emissions of  $\text{Ce}^{3+}$  and  $\text{Tb}^{3+}$  were observed. The intensity of  $\text{Ce}^{3+}$  emission were found reduced and that of  $\text{Tb}^{3+}$  increased when compared with emission intensity  $\text{La}_2\text{O}_2\text{S}:\text{Ce}^{3+}$  and  $\text{La}_2\text{O}_2\text{S}:\text{Tb}^{3+}$ , indicating the energy transfer from  $\text{Ce}^{3+}$  to  $\text{Tb}^{3+}$  ions in  $\text{La}_2\text{O}_2\text{S}$  host.

## REFERENCES

1. P.F.S. Pereira, M.G. Matos, L.R. Avila, E.C.O. Nassor, A. Cestari, K.J. Ciuffi, P.S. Calefi, E.J. Nassar, J. Lumin. 130 (2010) 488.
2. S. Nakamura, T. Mukai, and M. Senoh, Appl. Phys. Lett. 64(13) (1994) 1687.
3. S. Nakamura, MRS Bull, (1997) 29.
4. S. Nakamura and G. Fasol, Springer, (1997) 277.
5. R.C. Ropp, Luminescence and the Solid State, Elsevier, Amsterdam, (1991) 139.
6. P. Dorenbos, Phys. Rev. B 62 (2000) 15640.
7. T. L. Van, M. Che, J. M. Tatibouet, M. Kermarec, J. Catal. 142 (1993) 18.
8. S. Bernal, F. J. Botana, R. Garcia, J. M. Rodriguez-Izquierdo, React. Solids 4 (1987) 23.
9. G. Adachi, N. Imanaka, Chem. Rev., 98 (1998) 1479.
10. S. Bernal, G. Blanco, J. J. Calvino, J. Solid State Chem. 180 (2007) 2154.
11. W. M. Yen, M. Raukas, S. A. Basun, W. Schaik, U. van and Happek, J. Lumin. 69 (1996) 287.
12. M. Raukas, S. A. Basun, W. Schaik Van, W. M. Yen and U. Happek, Appl. Phys. Lett. 69, (1996) 3300
13. G. Blasse and B. C. Grabmaier, Luminescent Materials, (Springer, Berlin, German, (1994), Chap. 3.
14. X. Zhang, B. Park, N. Choi, J. Kima, G. C. Kimc, J. H. Yoo, Materials Letters, 63 (2009) 700.
15. B. F. Aull and H. P. Jenssen Phys. Rev., B 34 (1986) 6647.
16. J. W. H. Van Kreveld, H. T. Hintzen, R. Metselaar and A. Meijerink, J. Alloys Compd. 268 (1998) 272.
17. D. Curie, Plenum., (1975), 71.
18. H. G. Drickamer, C. W. Frank, and C. P. Slichter, Proc. Nat. Acad. Sci., 69 (1972) 933.
19. M. Jayasimhadri, B. V. Ratnam, K. Jang, H. S. Lee, B. J. Chen, S. S. Yi, J. H. Jeong, L. R. Moorthy, J. Am. Ceram. Soc. 93 (2010) 494.
20. Q. Su, J. Lin, B. Li, J. Alloys Compd., 225 (1995) 120.
21. W. X. Kuang, Y. N. Fan, K. W. Yao, Y. Chen, J. Solid State Chem. 140 (1998) 354.
22. A. N. Yerpude, S. J. Dhoble, Journal of Luminescence 132 (2012) 2975.
23. D. Marrero-Lopez, P. Nunez, M. Abril, V. Lavin, U.R. Rodriguez-Mendoza, V.D. Rodriguez, J. Non-Cryst. Solids 345 (2004) 377.
24. Z. L. Wang, H. B. Liang, L. Y. Zhou, J. Wang, M. L. Gong, Q. Su, J. Lumin. 128 (2008) 147.
25. X. X. Zhao, X. J. Wang, B. J. Chen, Q. Y. Meng, B. Yan, W. H. Di, Opt. Mater. 29 (2007) 1680.
26. D. Ananias, M. Kostova, F. A. Almeida Paz, A. Ferreira, L. D. Carlos, J. Klinowski, J. Rocha, J. Am. Chem. Soc. 126 (2004) 10410.
27. S. Shionoya, W. M. Yen, Boca 303 Raton, (1999) 190.
28. H. Wang, M. Yu, C. K. Lin, J. Lin, J. Colloid and Interface Sci. 300 (2006) 176.
29. K. N. Shinde, S. J. Dhoble, Animesh Kumar, Physica B 406, (2011), 94.
30. I. M. Nagpure, V. B. Pawade and S. J. Dhoble, Luminescence, 25 (2010) 9.
31. P. S. Thakre, S. C. Gedam, S. J. Dhoble, R. G. Atram doi:10.1016/j.jlumin.06(2011)50.
32. A. N. Yerpude, S. J. Dhoble, Journal of Luminescence, 132 (2012) 1781.
33. Y. D. Huh, J. H. Shim, Y. Kim, Y. R. Do, J. Electrochem. Soc. H57 (2003) 150.
34. Z. Ren, C. Tao, H. Yang and S. Feng, Mater. Lett. 61 (2007) 1654.
35. C. H. Lu, S. V. Godbole, M. Qureshi, Jpn. J. Appl. Phys. 45(4A) (2006) 2606.
36. I. M. Nagpure, K. N. Shinde, S. J. Dhoble, A. Kumar, J. Alloys and Comp., 481 (2009) 632.

37. A. M. Amiryani, A. M. Gurwich, R. V. Ktomina, Journal of Applied Spectroscopy 27 (1977) 468.
38. G. Blasse, B. C. Grabmaier, Luminescent Materials, Springer, Berlin, Heidelberg, (1994).
39. R. P. Rap, J. Electrochem. Soc., 150 (2003) H165 401
40. H. Lai, A. Bao, Y. Yang, Y. Tao, H. Yang, Y. Zhang, L. Han, J. Phys. Chem. C 112 (2008) 282.
41. J. Liao, B. Qiu, H. Lai, H. J. Lumin., 129 (2009) 668.
42. H. Matsukiyo, H. Yamada, Extended Abstracts, (1997) 315.
43. B. Huttel, U. Troppenz, K. O. Velthaus, C. R. Ronda, R. H. Mauch, J. Appl. Phys. 78 (12) (1995) 7282.
44. K. S. Sohn, Y. Y. Choi, H. D. Park, Y. G. Choi, J. Electrochem. Soc., 147 (6) (2000) 2375.
45. S. D. Cheng, C. H. Kam, S. Buddhudu, Mater. Res. Bull., 36 (2001) 1131.
46. J. L. Sommerdijk, J. M. P. J. Vestegen, J. Lumin., 9 (1974) 415.

## AUTHORS PROFILE



**V. V. Shinde** is presently working as Associate Professor & Head, Department of Electronics in Bajaj College of Science, Wardha, Maharashtra. He obtained his Ph. D. from R.T.M. Nagpur University, Nagpur. He has 33 years of teaching experience. He has 7 national and international research papers to his credit.



**Prof. Sanjay J. Dhoble**, is presently working as Professor in Department of Physics, RTM Nagpur university, Nagpur. He obtained his Ph.D. degree in 1992 in Solid State Physics from RTM Nagpur university, Nagpur.. He has 28 years of teaching and 27 Years of Research Experience. He worked on the synthesis and characterization of solid-state lighting materials, development of radiation dosimetry phosphors using thermo luminescence technique and utilization of fly ash. Dr. Dhoble published/ filed 16 patents and more than 552 research papers published in Scopus indexing journals. His h-index is 30 and 5209 citations on Scopus. Dr. Dhoble successfully guided 53 students for Ph.D. degree. He authored following books:

1. Principles and applications of organic light emitting diode (Publisher: Elsevier)
  2. Nanomaterials for Green Energy (Publisher: Elsevier)
  3. Spectroscopy of Lanthanide Doped Oxide Materials (Publisher: Elsevier)
  4. Phosphate phosphors for solid state lighting (Publisher: Springer)
  5. Phosphors for energy saving and conversion technology (Publisher: Taylor & Francis Group)
  6. Phosphors: Synthesis and Applications (Publisher: Pan Stanford).
- Dr. Dhoble is Editor of Luminescence: The Journal of Biological and Chemical Luminescence, John Wiley & Sons Ltd. Publication (Impact Factor: 1.691). He is also recipient of India's Top Faculty Research Award-2018 by Careers 360, for the top ten researchers in India in Physics on the basis of research papers published in Scopus research database in session 2017-2018, on 20th March 2018. His ORCID Id: 0000-0002-4249-8228.

# Prospective of *Monascus* Pigments as an Additive to Commercial Sunscreens

Natural Product Communications  
Volume 14(12): 1–7  
© The Author(s) 2019  
Article reuse guidelines:  
sagepub.com/journals-permissions  
DOI: 10.1177/1934578X19894095  
journals.sagepub.com/home/npx



Sunil H. Koli<sup>1</sup>, Rahul K. Suryawanshi<sup>1</sup>, Bhavana V. Mohite<sup>2</sup>, and Satish V. Patil<sup>1,3</sup>

## Abstract

Red and yellow pigments from *Monascus purpureus* (NMCC-PF01) were evaluated to enhance sun protection factor (SPF) of commercial sunscreens and *Aloe vera* extract. The extracted *Monascus* pigments contain rubropunctamine (red pigment) and the mixture of monascin and ankaflavin (yellow pigment) as major components. Antioxidant activity and *in-vitro* safety of the pigments were assessed by ferric reduction potential and DPPH radical scavenging assays, human keratinocytes (HaCaT), and erythrocytes (RBCs) cytotoxicity assay, respectively. In results, SPF of commercial sunscreens showed an increase of 36.5% with red pigment compared to the 13% increase by yellow pigment. The *in-vitro* studies showed 67.6% ferric reducing potential and 27% DPPH radical scavenging activity, neither cytotoxic effect against human keratinocytes nor haemolytic activity. These results confirmed the safe nature of the *Monascus* pigments; however, *in-vivo* studies merit further research. In conclusion, screened pigments from *Monascus purpureus* may act as potential candidates to increase SPF of commercial sunscreen naturally.

## Keywords

SPF, commercial sunscreens, *Monascus* pigments, antioxidant, *Aloe vera* extract

Received: August 1st, 2019; Accepted: November 5th, 2019.

Ultraviolet (UV) radiation can damage the skin by multiple modes like mutations in cell DNA, the formation of reactive oxygen species, changes in histochemistry of cell, increased expression levels of the p53 gene, and/or influencing the immune system.<sup>1</sup> Increased consciousness about skin exposure to ultraviolet radiation has tempted the use of commercial sunscreen products. The commercial sunscreen is generally composed of organic, inorganic UV absorbers like aminobenzoates, cinnamates, avobenzene, oxybenzone, and oxides of zinc, titanium, iron. However, increasing side effects of some sunscreen components has made it indispensable to search for natural photoprotectants.<sup>2</sup> The most commonly utilizing sunscreen ingredients such as oxybenzone linked to sun exposure triggered allergic reactions, generating free radicals, which may be associated with cell damages.<sup>3,4</sup> While the nanoscale TiO<sub>2</sub> and ZnO are responsible for the generation of a substantial amount of reactive oxygen species, which upon UV illumination causes modifications in nucleic acid bases and eventually cell death.<sup>5,6</sup> Consequently, it is the need of an hour to look for other options to replace harmful components of sunscreens.

Nature is an abundant source of metabolites, considering the fact that UV damage is not only limited to humans but also to microbes. In continuation of our research on natural UV protectants,<sup>7</sup> we targeted pigments from *Monascus purpureus*, which are well known for their multifaceted use in food

coloration and range of other bioactivities. The selection of these pigments was rationalized on their variable bioactivity after linking with different amino acids.<sup>8</sup> This amino acid-based derivatization of *Monascus* pigments may change their absorption maxima in the UV region. Here we sought to study the ability of food-grade pigments from *Monascus purpureus* (NMCC-PF01) (i) to increase the SPF of commercially available sunscreens, (ii) evaluation of their antioxidant potential, and (iii) cytotoxicity testing on human keratinocytes and erythrocytes cells.

<sup>1</sup>School of Life Sciences, Kavayitri Bahinabai Chaudhari North Maharashtra University, Jalgaon, Maharashtra, India

<sup>2</sup>Department of Microbiology, Jankidevi Bajaj College of Science, Wardha, Maharashtra, India

<sup>3</sup>North Maharashtra Microbial Culture Collection Centre (NMCC), Kavayitri Bahinabai Chaudhari North Maharashtra University, Jalgaon, Maharashtra, India

## Corresponding Author:

Satish V. Patil, School of Life Sciences, Kavayitri Bahinabai Chaudhari North Maharashtra University, Post Box - 80, Jalgaon, 425001, Maharashtra, India.  
Email: satish.patil7@gmail.com



## Experimental

### Commercial Sunscreens, Chemicals, and Plant Extract

Two different commercial sunscreens with labeled sun protection factors (SPFs) of 15 and 24 were brought from local market Jalgaon, India. Ethanol was purchased from Sd-fine chemicals (India). For plant extract, 10 g of *Aloe vera* leaf was macerated and filtrated through muslin cloth; the resultant extract was used for further studies.

### Microorganisms and Cultural Conditions

*Monascus purpureus* (NMCC-PF01) was procured from North Maharashtra Microbial Culture Collection Centre (NMCC), Jalgaon and used for pigment production. The potato dextrose agar (PDA) (Hi-Media, India) slope was used for the maintenance of fungal culture at 4°C and subcultured periodically.

### Microbial Pigments Production

The inoculum preparation and production of *Monascus* pigments were performed in aliquots as per our previous report.<sup>9</sup>

### Extraction and Purification of Pigments

For extraction of extracellular *Monascus* pigments, fungal mycelium was separated by filtering fermentation broth using Whatman filter paper. The dark red colored filtrate was concentrated under vacuum and extracted by 95% (v/v) ethanol. It was kept rotating for 1 hour at 200 rpm, followed by filtration through Whatman paper to derive crude extract of pigments.<sup>10</sup> The crude *Monascus* pigments were further purified by chromatographic methods.

### Column Chromatography

The chromatography column (300 × 18 mm sintered disc glass column) with silica mesh (60 × 120) was used with a solvent gradient system of 100: 0, 100: 10, 50: 50 chloroform: methanol gradient 4 mL/min.<sup>9</sup>

### Thin-Layer Chromatography

The pigment fractions collected after column chromatography were concentrated and spotted on TLC (silica gel 60 Merck Darmstadt, Germany) plate, and pigments were separated with a solvent system of chloroform : methanol : acetic acid (285: 24: 9). The two separated (yellow and red color) bands on TLC plate were scrapped and redissolved in ethanol and centrifuge

at 3000 rpm for 15 minutes to settle down the silica. The supernatant was collected and concentrated for further study.<sup>11,12</sup>

### Pigments Characterization

Two dominant colored pigments (yellow and red) were obtained and characterized using UV-Visible absorption (Shimadzu spectrophotometer), Fourier transform infrared spectroscopic analysis (Shimadzu FTIR 8400, range 400 cm<sup>-1</sup> to 4000 cm<sup>-1</sup>), and mass spectrophotometry analysis (WATER Q-TOF MICROMASS).

### Determination of Sunscreen Protection Factors

The sunscreen protection factors (SPFs) of commercial sunscreens (SPF-15 & 24) and sunscreens enrich with *Monascus* pigments were determined by the *in vitro* spectrophotometric method with slight modification.<sup>7,13,14</sup> The commercial sunscreens with labeled SPF of 15 and 24 and *Aloe vera* extract were constituted as control while, in the test, *Monascus* pigments at a concentration of 4% and 8% w/w were added to the above commercial sunscreens. Multiple samples (0.1 g) each from control and test sunscreens formulations were taken and separately added to volumetric flasks containing 10 mL ethanol. All samples (ie, controls and pigment-supplemented samples) were ultrasonicated for 5 minutes and then filtrated through a muslin cloth. The 0.5 mL aliquots of filtrate were collected in tube and made up to 2.5 mL by addition of ethanol.

The optical density of each of these solutions was measured in the UV range from 290 to 320 nm at 5 nm intervals using ethanol as blank. Three independent analyses were performed, and SPFs were calculated, according to Mansur et al. (1986)<sup>15</sup> using the following formula:

$$\text{SPF} = \text{CF} \times \sum_{290}^{320} \text{EE} (\lambda) \times I (\lambda) \times \text{Abs} (\lambda)$$

where CF (correction factor) = 10; EE (λ) = erythmogenic effect of radiation with wavelength λ; Abs. (λ) = absorbance value of a solution; and I = solar intensity spectrum. EE (λ) × I is constant and determined by Sayre et al. (1979),<sup>16</sup> as shown in Supplemental table S1.

### Ferric Reducing Potential

Antioxidant potential of the pigment samples was determined by evaluating ferric reducing activity as per our previous reports.<sup>7,14</sup> In brief, individual test samples, including red and yellow pigments (10 mg each) were added to 2.5 mL phosphate buffer (pH 6.6) and 2.5 mL of 1 % w/v potassium ferricyanide and incubated for 20 minutes. Further, the mixture was added with 10 % w/v trichloroacetic acid (2.5 mL) and centrifuged at 3000 rpm for 10 minutes (Remi C-24 BL). Then, 2.5 mL of the mixture from the upper layer was mixed with distilled water (2.5 mL), and freshly prepared 0.5 mL of ferric chloride solution (0.1% w/v) was added, and the volume was made up to

100 mL with distilled water. The optical density was recorded at 700 nm. Percent reduction in the ferric chloride was determined by comparing with the ascorbic acid as a positive control. The experiment was carried out in triplicates.

### DPPH Radical Scavenging Assay

The radical scavenging activity was determined by DPPH (1,1-Diphenyl-2-picrylhydrazyl) assay with a slight modification of Chang et al<sup>17</sup> method. In brief, 40  $\mu$ L of *Monascus* pigments (10 mg/mL in DMSO) was mixed with 2.96 mL DPPH (0.1 mM) solution. The reaction mixture was vigorously shaken and incubated in dark condition at room temperature for 30 minutes. The absorbance was measured at 517 nm with DPPH as control. Ascorbic acid was used as positive control. The % radical scavenging activity was calculated using the following formula,

$$\% \text{ Inhibition} = \frac{\text{Abs Control} - \text{Abs Sample}}{\text{Abs Control}} \times 100$$

where *Abs control* is the absorbance of DPPH solution and *Abs sample* is the DPPH + pigments.

### Human Keratinocytes Cytotoxicity Assay

The cytotoxicity of the pigments was analyzed using human keratinocytes (HaCaT) cell line (obtained from NCCS, Pune, India). Dulbecco's Modified Eagle's medium (DMEM) supplemented with 10% fetal bovine serum (FBS), and the 1X antibiotic solution was used for cells maintenance at 37°C in a CO<sub>2</sub> incubator. The cells were harvested and seeded into a 96-well plate at a concentration of  $1 \times 10^4$  cells/well. After 24 hour incubation, the samples were added at different concentrations (0.25-2 mg/mL), and the cells were incubated for further 24 hour. The test samples were prepared in 10% DMSO. The cytotoxicity of the samples was evaluated using the standard method of MTT (3-(4,5-dimethylthiazol-2-yl)-2,5-diphenyltetrazolium bromide) assay.<sup>18</sup> Twenty microliter (stock-5 mg/mL) MTT reagent was added in each well and kept for incubation in the CO<sub>2</sub> incubator at 37°C for 4 hour. Then 100  $\mu$ L of DMSO was added to each well and kept in the dark for 1 hour. The absorbance was measured at 595 nm wavelength. The cells without treatment were taken as a control (added 10% DMSO) for the study. Experiments were done in triplicate, and the percentage viability was calculated by using the following equation:

$$\% \text{ Cell viability} = (\text{OD}_{595} \text{ (Test)} / \text{OD}_{595} \text{ (Control)}) \times 100$$

### Human Erythrocytes Cytotoxicity Assay

The cytotoxicity testing of the pigment molecules was performed by hemolysis assay according to the method of Borase et al<sup>14</sup> with appropriate modifications. Five-milliliter blood was collected from a healthy volunteer, and it was added with ethylene diamine tetra-acetic acid (EDTA) to inhibit the

coagulation of blood cells. The RBCs (red blood cells) were separated from blood, 1 mL of blood was mixed into 5 mL of phosphate buffer saline (PBS) (pH-7.4) and the mixture centrifuged to 6000 rpm for 10 minutes at 37°C (Remi C-24 BL, India) to remove the supernatant containing platelets and plasma to obtain pellets of RBCs. The pellet of RBCs was resuspended into 10 mL of PBS and (a process of washing was repeated four times) again centrifuged them.

One milliliter aliquots of uniformed cells suspension (RBCs) were taken in eppendorf tubes, and 1 mg/mL of yellow and red *Monascus* pigments were added in test vial and mixed by gentle shaking. One milliliter of sterile water and phosphate buffer saline was added in the positive and negative control, respectively. The mixtures in all tubes were incubated in the dark for 4 hour and centrifuged for 10 minutes at 1000g. Supernatants from all the tubes were further subjected to spectroscopic absorption at 541 nm, and the optical densities were used to calculate percent hemolysis by the following formula:

$$\% \text{ Hemolysis} = \frac{\text{Sample absorbance} - \text{Negative control absorbance}}{\text{Positive control absorbance} - \text{Negative control absorbance}} \times 100$$

The hemolysis of the RBCs for different treatment and positive and negative control were also confirmed by using Foldscope (Foldscope Instrument Inc., CA).

The partially purified pigments from *M. purpureus* were first characterized by UV visible (Supplemental figure S1) and mass spectroscopic analysis (Supplemental figure S2). The pigment components were identified as red pigment fraction representing rubropunctamine ( $m/z$  354.16 MH<sup>+</sup>), while yellow representing a mixture of monascin ( $m/z$  359.23 MH<sup>+</sup>) and ankaflavin ( $m/z$  387.28 MH<sup>+</sup>).

The SPF was calculated by measuring the absorbance within the range of 290-320 nm.<sup>15</sup> Two commercial sunscreens with claimed SPF values of 15 and 24 empirically showed SPF values of  $16.26 \pm 0.75$  and  $24.42 \pm 1.06$ , respectively, whereas SPF of *Aloe vera* extract was  $0.1 \pm 0.01$ . In combinational studies, red pigment (4% w/w) combined with sunscreen having 15 and 24 labeled SPF showed 17.0% and 13.26% increase, respectively, while the yellow pigment (4% w/w) with same sunscreens showed a marginal increase of 1.6% and 3.48%, respectively. The same pigments with 8% (w/w) concentration increased the SPF by 36.53% and 30.67% (rubropunctamine) and 13.16% and 12.40% (monascin and ankaflavin), respectively (Table 1). Similarly, with the rubropunctamine (4% and 8%) combined with *Aloe vera* extract, the SPF was  $2.55 \pm 0.38$  (2550%) and  $3.87 \pm 0.37$  (3870%), respectively (Table 1). A mixture of monascin and ankaflavin increased the SPF of *Aloe vera* to  $1.74 \pm 0.11$  (1740%) and  $2.13 \pm 0.124$  (2130%) with respective concentrations of 4% and 8% (Table 1).

The rationale behind this SPF increment probably lies in a combination of pigment with sunscreen components that resulted in significant changes in the infra-red spectrum (Supplemental figure S3c). For yellow pigment and sunscreen combination, the changes were indicated by the broadening of the peaks at  $3460.41 \text{ cm}^{-1}$  for the alcoholic group and  $2967.58$

**Table 1.** Sunscreen Protection Factors (SPFs) for Commercial Sunscreen Preparations and Natural Plant Extracts Before and After Supplementation with Pigments From *Monascus purpureus*

Commercial sunscreens	Ingredients	SPF	Calculated SPF	SPF pigment + sunscreens			
				Red pigment		Yellow pigment	
				4%	8%	4%	8%
Sunscreen 1	Aqua, Paraffinum Liquidum, Emulsifying Wax, Titanium Dioxide, Steric Acid, Borex, Almond Oil, Vit-e, Isopropyl Myristate, Benzophenone-3, Octylmethoxy Cinnamate, Propylene Glycol, Allantoin, Phenoxyethanol, Methyl Paraben, Myristate, Ethylene Diamine Tetra Acetate, Imidazolidinyl Urea, Allantoin, Propyl Paraben, Isopropyl, Fragrance	15	16.26 ± 0.75	19.03 ± 0.74	22.2 ± 1.2	16.95 ± 0.62	18.4 ± 0.52
Sunscreen 2	Aqua, Ethylhexyl, Salicylate, Avobenzone, Glycerine, Steric Acid, Palmitic acid, Phenylbenzimidazol Sulphonic Acid, Glycol Stearate, Steramide AMP, PEG-100 Stearate, Dimethicone, Glyceryl Stearate, Xanthan Gum, Potassium Hydroxide, Niacinamide, Disodium EDTA, Propylene Glycol, Carbomer, Cetyl Alcohol, Sodium Hydroxide, Cymbopogon, Schoenanthus (Lemongrass) Extract, CucumisSativis (Cucumber) Fruit Juice, Lactic Acid, Phenoxyethanol, Methyl and Propylparaben	24	24.42 ± 1.06	27.66 ± 0.81	31.91 ± 1.63	25.27 ± 0.33	27.45 ± 1.54
Aloe vera plant extract		NA	0.1 ± 0.01	2.55 ± 0.38	3.87 ± 0.37	1.74 ± 0.11	2.13 ± 0.124

NA-, not applicable.

$\text{cm}^{-1}$  for C-H. The frequency at  $1652.03 \text{ cm}^{-1}$  indicated  $\alpha$ - $\beta$  unsaturated ketone, while the other two peaks at  $1922.13$  and  $1229.48 \text{ cm}^{-1}$  were newly detected. The infra-red results indicate that the *Monascus* pigments may chemically interact with commercial sunscreen and undergo derivatization by making some changes in functional groups of chemical constituents present in sunscreen. The outcome of the study specifies the use of *Monascus* pigments as an additive to sunscreen, which may provide more protection from UV-B radiation. These results are in agreement with Suryawanshi et al and Borase et al.<sup>7,14</sup>

The genesis of free radicals may occur when the skin is exposed to UV light. Antioxidants are well known to protect the skin from free radicals. Thus, a variety of antioxidant compounds are incorporated in cosmetic products, which are protecting the skin from oxidative damage. In the present study, whether, the pigments have the potential to protect the skin from free radicals were determined by antioxidant assay. The *Monascus* fermented products and extracted compounds are known to use in cosmetic preparation, for their antioxidant and nutricosmetic potential.<sup>19</sup> During the study, red pigment (rubropunctamine) showed 67.6% ferric reduction potential as compared to 100% for standard antioxidant, ascorbic acid, and 3.2% for yellow pigments. Similarly, the DPPH assay revealed that 27% and 14.51% radical scavenging activity for red and yellow pigments, respectively. These signify that red pigments have high antioxidant potential as compared to yellow pigments. Similarly, the antioxidant activity of *Monascus* fermented products and/or extract such as rice, corn, and sorghum have been reported and correlated with the high amount of red pigments present.<sup>20</sup>

The extracted *Monascus* fermented soybean in methanol and 80% ethanol were shown the highest Trolox equivalent antioxidant activity ( $3.13 \pm 0.06 \text{ mM TE/g}$ ) and oxygen radical

**Table 2.** *In Vitro* Toxicity Testing of Red *Monascus* Pigments in Human Keratinocytes (HaCaT) Cell Line

Pigments concentrations (mg/mL)	Cytotoxicity against human keratinocytes	
	% Viability of cells	
	Red pigment	Yellow pigment
0.00	$100 \pm 0.24$	$100 \pm 1.39$
0.25	$97.43 \pm 1.02$	$97.72 \pm 1.33$
0.50	$96.44 \pm 0.95$	$94.49 \pm 1.12$
1.00	$95.25 \pm 0.57$	$92.76 \pm 0.89$
2.00	$91.72 \pm 1.42$	$90.64 \pm 0.96$

scavenging activity ( $2.79 \pm 0.09 \text{ mM TE/g}$ ), respectively. Besides, pigments showed significant inhibition of enzymes, tyrosinase, hyaluronidase, and elastase, which are related to skin aging.<sup>21</sup> The results of the present study have also following these previous reports, which ascertain the antioxidant potential of *Monascus* pigments.

The assessment of the toxicological properties of the ingredients of cosmetics and pharmaceutical formulations is an essential regulatory requirement.<sup>22</sup> Various *in vitro* and *in vivo* toxicological methods were executed for the evaluation of toxicity. In the case of cosmetic products, considering the specific route of topical application, the *in vitro* cytotoxicity testing on skin cell lines (in particular keratinocytes and fibroblasts) can be used for primary toxicological evaluation of new ingredients such as surfactants, colorants, preservatives, and additives.<sup>2,23-25</sup> In this study, the human keratinocyte (HaCaT cell line) was used for evaluation of the *Monascus* pigments skin toxicity by using *in vitro* MTT assay.

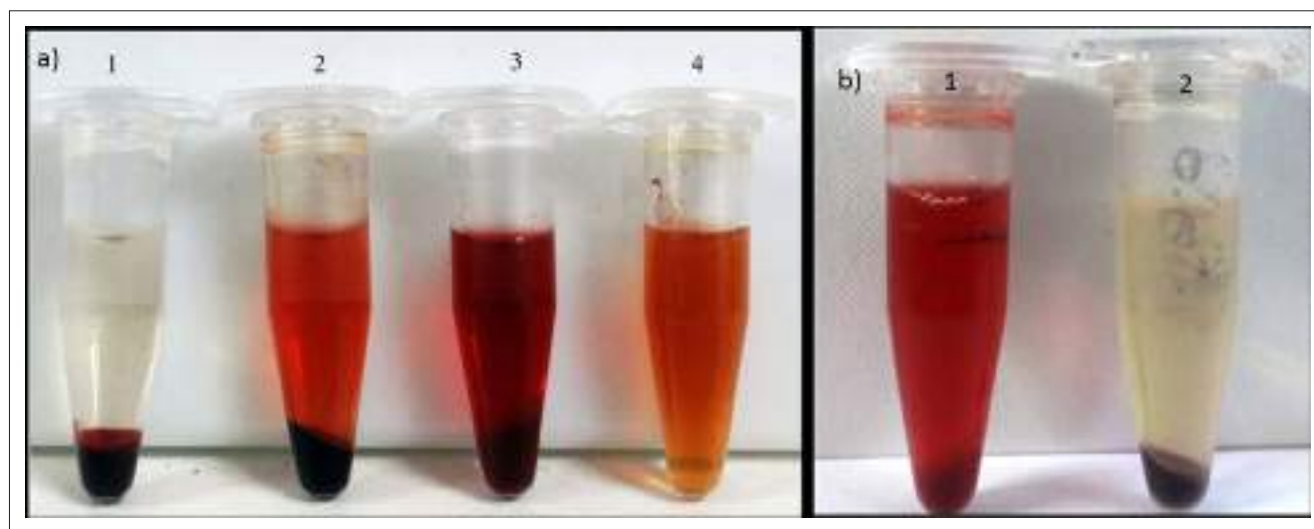


**Figure 1.** Toxicity Testing of *Monascus* Pigments by RBCs Hemolysis: (a) 1 - PBS-Negative Control, 2-Red Pigment +RBCs Test, 3-Sterile Water Positive Control, 4- Red Pigment, and (b) 1 Positive Control, 2-Yellow Pigment +RBCs Test.

The results of the cytotoxicity of *Monascus* pigments against normal human keratinocytes were shown in Table 2 which indicated that *Monascus* pigments are nontoxic toward the normal skin cell in the *in vitro* study. Since the cells even were treated with a higher concentration (2 mg/mL) of pigments, no significant cell mortality (<10% mortality) was recorded. Likewise, the yellow *Monascus* pigment, ankaflavin showed selective cytotoxicity to human hepatocellular carcinoma cells (Hep G2), but low toxicity to normal fibroblast, while, no cytotoxicity of monascin against the normal human lung fibroblast (WI-38 and MCR-5 fibroblast cells). Also, the red *Monascus* pigments are not reported for toxicity against the normal human cells. In recent year, Yuliana et al studied the toxicity of *Monascus* pigments by using computerized structure-activity relationships, against fish, daphnid, and green algae and the toxicity were determined by ecological structure-activity relationships (ECOSAR).<sup>26</sup> Among the 57 tested *Monascus* pigments, almost all red pigments were shown no toxicity toward the tested organism. This suggesting that the pigments derived from *Monascus* are nontoxic nature and safe to be used in commercial sunscreen formulations, which are applied on the skin.

In cytotoxicity analysis, the potential of pigments to damage the RBC was measured by the amount of hemoglobin released from treated RBCs. RBCs test enables the quantification and evaluation of the *in vitro* irritant effects of the surfactants (added into a range of cosmetics products) and sunscreens formulations.<sup>27,28</sup> In the present investigation, both pigment molecules were responsible for a negligible percentage of hemolysis, that is,  $0.11 \pm 0.01\%$  by rubropunctamine and  $0.36 \pm 0.04\%$  by a mixture of monascin and ankaflavin. Sterile water served as a positive control, which was considered to show 100% hemolysis (Figure 1). In microscopic observation, RBCs in test samples were healthy and well ordered compared with positive control showing disorganized and faint cells.

Red and yellow *Monascus* pigments, in combination with commercial sunscreens, may form different functional groups that consequently responsible for absorption of light in UVB region (290-320 nm). The potential to increase SPF, antioxidant activity, no cytotoxicity against the healthy skin cells as well as earlier reported antimicrobial activities of these pigments might help to put more emphasis on the use of microbial pigments in commercial sunscreens. Though *Monascus* is food grade pigments, their use on skin rest on *in vivo* safety studies and consumers' choice.

### Acknowledgments

SVP acknowledges the Department of Biotechnology, New Delhi, for the Indo-US Foldscope Major Research Project. The authors are thankful to UGC-SAP and DST-FIST for providing financial support to the SOLS department.

### Declaration of Conflicting Interests

The author(s) declared no potential conflicts of interest with respect to the research, authorship, and/or publication of this article.

### Funding

The author(s) disclosed receipt of the following financial support for the research, authorship, and/or publication of this article: Mr Sunil Koli thankful to UGC-BSR for providing fellowship to research work (Fie No. NMU/SLS/491/2015(UGC BSR, Dated 11 Aug.2015).

### ORCID ID

Satish V. Patil  <https://orcid.org/0000-0001-6167-2511>

### Supplemental Material

Supplemental material for this article is available online.

### References

- Maverakis E, Miyamura Y, Bowen MP, Correa G, Ono Y, Goodarzi H. Light, including ultraviolet. *J Autoimmun.* 2010;34(3):J24 7-J257.
- Alnuqaydan AM, Sanderson BJ. Toxicity and genotoxicity of beauty products on human skin cells in vitro. *J Clin Toxicol.* 2016;6(4):315.
- Rodríguez E, Valbuena MC, Rey M, Porras de Quintana L. Causal agents of photoallergic contact dermatitis diagnosed in the National Institute of dermatology of Colombia. *Photodermatol Photoimmunol Photomed.* 2006;22(4):189-192.
- Hanson KM, Gratton E, Bardeen CJ. Sunscreen enhancement of UV-induced reactive oxygen species in the skin. *Free Radic Biol Med.* 2006;41(8):1205-1212.
- Matej S, Metka F, Jana P, Sasa N. Titanium dioxide in our everyday life; is it safe? *Radiol Oncol.* 2011;45:227-247.
- Lewicka ZA, William WY, Oliva BL, Contreras EQ, Colvin VL. Photochemical behavior of nanoscale TiO<sub>2</sub> and ZnO sunscreen ingredients. *J Photoch Photobio A Chem.* 2013;263:24-33.
- Suryawanshi RK, Patil CD, Borase HP, et al. Towards an understanding of bacterial metabolites prodigiosin and violacein and their potential for use in commercial sunscreens. *Int J Cos Sci.* 2014:1-10.
- Kim C, Jung H, Kim YO, Shin CS. Antimicrobial activities of amino acid derivatives of *Monascus* pigments. *FEMS Microbiol Lett.* 2006;264(1):117-124.
- Koli SH, Suryawanshi RK, Patil CD, Patil SV. Fluconazole treatment enhances extracellular release of red pigments in the fungus *Monascus purpureus*. *FEMS Microbiol Lett.* 2017;364(8):fnx058.
- Velmurugan P, Hur H, Balachandar V, et al. *Monascus* pigment production by solid-state fermentation with corn cob substrate. *J Biosci Bioeng.* 2011;112(6):590-594.
- Martínková L, J<sup>o</sup>zlová P, Veselý D. Biological activity of polyketide pigments produced by the fungus *Monascus*. *J Appl Bacteriol.* 1995;79(6):609-616.
- Hu Z, Zhang X, Wu Z, Qi H, Wang Z. Perstraction of intracellular pigments by submerged cultivation of *Monascus* in non-ionic surfactant micelle aqueous solution. *Appl Microbiol Biotechnol.* 2012;94(1):81-89.
- Dutra EA, Oliveira DAGdaC, Kedor-Hackmann ERM, Santoro MIRM. Determination of sun protection factor (SPF) of

- sunscreens by ultraviolet spectrophotometry. *Rev Bras Cienc Farm.* 2004;40(3):381-385.
14. Borase HP, Patil CD, Suryawanshi RK, Patil SV. *Ficus carica* latex-mediated synthesis of silver nanoparticles and its application as a chemophotoprotective agent. *Appl Biochem Biotechnol.* 2013;171(3):676-688.
  15. Mansur JS, Breder MN, Mansur MC, Azulay RD. Determination of sun protection factor by spectrophotometry. *An Bras Dermatol.* 1986;61:121-124.
  16. Sayre RM, Agin PP, LeVee GJ, Marlowe E. A comparison of in vivo and in vitro testing of sunscreens formulas. *Photochem Photobiol.* 1979;29(3):559-566.
  17. Chang S-T, Wu J-H, Wang S-Y, Kang P-L, Yang N-S, Shyr L-F. Antioxidant Activity of Extracts from *Acacia confusa* Bark and Heartwood. *J Agric Food Chem.* 2001;49(7):3420-3424.
  18. Gasparini LS, Macedo ND, Pimentel EF, et al. *In vitro* Cell Viability by CellProfiler<sup>®</sup> Software as Equivalent to MTT Assay. *Pharmacogn Mag.* 2017;13(Suppl 2):S365-S369.
  19. Caro Y, Venkatachalam M, Lebeau J, Fouillaud M, Dufossé L. Pigments and colorants from filamentous fungi. In: Merillon J-M, Ramawat GK, eds. *Fungal Metabolites*. Cham, Switzerland: Springer; 2017:1-70. 499-568.
  20. Srianta I, Zubaidah E, Estiasih T, Iuchi Y, Yamada M. Antioxidant activity of pigments derived from *Monascus purpureus*-fermented rice, corn, and sorghum. *Int Food Res J.* 2017;24(3):186-1191.
  21. Jin Y-J, Pyo Y-H. Effect of *Monascus*-fermented soybean extracts on antioxidant and skin aging-related enzymes inhibitory activities. *Prev Nutr Food Sci.* 2017;22(4):376-380.
  22. da Rocha VPM. Study of the cytotoxicity of raw materials of cosmetic and topical pharmaceutical formulations [Master's thesis]. Porto, Portugal: Faculdade De Medicina Universidade Do Porto; 2015.
  23. Kyadarkunte A, Patole M, Pokharkar V. In vitro cytotoxicity and phototoxicity assessment of acylglutamate surfactants using a human keratinocyte cell line. *Cosmetics.* 2014;1(3):159-170.
  24. Tomankova K, Kejlova K, Binder S, et al. In vitro cytotoxicity and phototoxicity study of cosmetics colorants. *Toxicol In Vitro.* 2011;25(6):1242-1250.
  25. Spindola DG, Hinsberger A, Antunes VMdeS, Michelin LFG, Bincoletto C, Oliveira CR. In vitro cytotoxicity of chemical preservatives on human fibroblast cells. *Braz J Pharm Sci.* 2018;54(1):1-9.
  26. Yuliana A, Wibowo MS, Julianti E. Solubility and toxicity level of *Monascus* pigments. *Trends Tech Sci Res.* 2018;2(4):1-3.
  27. Alves EN, Presgrave RdeF, Presgrave OAF, Sabagh FP, de Freitas JCBR, Corrado AP. A reassessment of the *in vitro* RBC haemolysis assay with defibrinated sheep blood for the determination of the ocular irritation potential of cosmetic products: comparison with the *in vivo* Draize rabbit test. *Altern Lab Anim.* 2008;36(3):275-284.
  28. Reis Mansur MCPP, Leitão SG, Cerqueira-Coutinho C, et al. In vitro and in vivo evaluation of efficacy and safety of photoprotective formulations containing antioxidant extracts. *Rev Bras Farmacogn.* 2016;26(2):251-258.

---



---

 PHYSICAL CHEMISTRY  
 OF SOLUTIONS
 

---



---

# Ultrasonic Investigations on Molecular Interactions of *N*-Phthaloyl Compounds in Protic and Non-Protic Solvents at 303–318 K

Pradip Tekade<sup>a,\*</sup>, Bhagyashri Tale<sup>a,\*\*</sup>, and Sonal Bajaj<sup>a</sup>

<sup>a</sup>Department of Chemistry, Jankidevi Bajaj College of Science, Jannalal Bajaj Marg, Civil Lines, Wardha, India

\*e-mail: pradiptekade@gmail.com

\*\* e-mail: bhagyashritale@gmail.com

Received January 27, 2018; revised December 27, 2018; accepted January 15, 2019

**Abstract**—Ultrasonic studies of (1,3-dioxo-1,3-dihydro-2H-isoindol-2-yl)-4-methylpentanoic acid (NPTLU), 2-(2-(2-(4-chlorophenyl)-1H-benzo[d]imidazol-1-yl)-2-oxoethyl)isoindoline-1,3-dione (C-BI-CL-L), 2-(4-methyl-1-(2-(4-nitrophenyl)-1H-benzo[d]imidazol-1-yl)-1-oxopentan-2-yl)isoindoline-1,3-dione (C-BI-NO<sub>2</sub>-L), 2-(1-(2-(4-nitrophenyl)-1H-benzo[d]imidazol-1-yl)-1-oxobutan-2-yl)-2,3-dihydroinden-1-one (C-BI-NO<sub>2</sub>-G), 2-(1,3-dioxo-1,3-dihydro-2H-isoindol-2-yl)-*N*-(4-oxo-2-phenylquinazolin-3(4H)-yl) acetamide (C-QA-GL), and 1-(2-((4-oxo-2-phenylquinazolin-3(4H)-yl)carbamoyl)benzoyl)pyrrolidine-2-carboxylic acid (C-QA-PR) in solution of polar and non-polar solvent of various concentrations at 303–318 K. Density and ultrasonic velocity measured and with the help of these data, different thermo-acoustical parameters viz. adiabatic compressibility, intermolecular free length, acoustic impedance, surface tension, Rao's constant, molar volume, Wada's constant calculated using standard formulas. The variation of these parameters with concentration and temperature studied using graphical representations of these parameters. Ethyl alcohol and DMSO were chosen as polar and non-polar solvents, respectively. The variation in different properties reveals the presence of specific molecular interactions in solute and solvent used, which will give information regarding drug transmission and absorption.

**Keywords:** adiabatic compressibility, intermolecular free length, acoustic impedance, surface tension, Rao's constant, molar volume, Wada's constant

**DOI:** 10.1134/S0036024419090188

## INTRODUCTION

Ultrasonic waves are used to study the molecular structures, interactions and molecular energies. We reported ultrasonic studies on molecular interactions in *N*-phenyl-3-(pyridin-4-yl) prop-2-enamide solutions in ethanol at 303, 308, 313 K [1] and ultrasonic study of pyridoxine solutions at different temperatures and concentrations [2]. Ultrasonic study of liquid solutions is also reported by various researchers [3–5]. IR spectroscopy study is also reported to study hydrogen bonding [6–9] and molecular interactions [10].

## EXPERIMENTAL

We studied (1,3-dioxo-1,3-dihydro-2H-isoindol-2-yl)-4-methylpentanoic acid (NPTLU), 2-(2-(2-(4-chlorophenyl)-1H-benzo[d]imidazol-1-yl)-2-oxoethyl)isoindoline-1,3-dione (C-BI-CL-L), 2-(4-methyl-1-(2-(4-nitrophenyl)-1H-benzo[d]imidazol-1-yl)-1-oxopentan-2-yl)isoindoline-1,3-dione (C-BI-NO<sub>2</sub>-L), 2-(1-(2-(4-nitrophenyl)-1H-benzo[d]imidazol-1-yl)-1-oxobutan-2-yl)-2,3-dihydroinden-1-one (C-BI-NO<sub>2</sub>-G), 2-(1,3-dioxo-1,3-dihydro-2H-isoindol-2-yl)-*N*-(4-oxo-2-phenylquinazolin-3(4H)-yl) acetamide (C-

QA-GL), and 1-(2-((4-oxo-2-phenylquinazolin-3(4H)-yl)carbamoyl) benzoyl) pyrrolidine-2-carboxylic acid (C-QA-PR) (Table 1) in solution of polar and non-polar solvent. AR grade ethanol and DMSO used as a solvent. Density measurements performed by using pycnometer. The ultrasonic velocity (*U*) of these solutions measured using Digital Ultrasonic Echo Pulse Velocity Meter, Model VCT-70 (Vi Microsystem Pvt. Ltd., Chennai-96) at frequency 2 MHz with an accuracy of 0.1%. The various acoustical parameters like adiabatic compressibility ( $\beta_{ad}$ ), intermolecular free length ( $L_f$ ), acoustic impedance ( $Z$ ), Wada's constant ( $W$ ), Rao's constant ( $R$ ), molar volume ( $V_m$ ), surface tension ( $S$ ) are calculated from  $U$  and  $\rho$  value using standard formulae:

adiabatic compressibility

$$\kappa = (1/v^2\rho), \text{ kg}^{-1} \text{ ms}^2,$$

acoustic impedance

$$Z = v\rho, \text{ kg m}^{-2} \text{ s}^{-1},$$

**Table 1.** Structure of studied compounds

S.N.	Name	Structure
1	2-(1,3-Dioxo-1,3-dihydro-2H-isoindol-2-yl)-4-methyl-pentanoic acid ( <i>N</i> -phthaloylleucine) (NPT-LU)	
2	2-(2-(2-(4-Chlorophenyl)-1H-benzo[d]imidazol-1-yl)-2-oxoethyl)isoindoline-1,3-dione (C-BI-CL-L)	
3	2-(4-Methyl-1-(2-(4-nitrophenyl)-1H-benzo[d]imidazol-1-yl)-1-oxopentan-2-yl)isoindoline-1,3-dione (C-BI-NO <sub>2</sub> -L)	
4	2-(1-(2-(4-Nitrophenyl)-1H-benzo[d]imidazol-1-yl)-1-oxobutan-2-yl)-2,3-dihydroinden-1-one (C-BI-NO <sub>2</sub> -G)	
5	2-(1,3-Dioxo-1,3-dihydro-2H-isoindol-2-yl)- <i>N</i> -(4-oxo-2-phenylquinazolin-3(4H)-yl)acetamide (C-QA-GL)	

Table 1. (Contd.)

S.N.	Name	Structure
6	1-(2-((4-Oxo-2-phenylquinxolin-3(4H)-yl)carbamoyl)benzoyl)pyrrolidine-2-carboxylic acid (C-QA-PR)	

free length

$$L_r = (K/v\rho^{1/2}), \text{ m,}$$

Rao's constant

$$R = Vv^{1/3},$$

surface tension

$$v = (S/6.3 \times 10^{-4} \rho)^{2/3},$$

where  $\rho$  is density of the solution,  $K$  is Jacobson temperature dependent constant defined as  $K = (93.875 + 0.345T) \times 10^{-8}$ ,  $M$  is molecular weight.

FTIR spectrum recorded using Bruker Alpha FTIR spectrometer at Department of Chemistry, Jankidevi Bajaj College of Science, Wardha.

## RESULT AND DISCUSSION

**Acoustical study.** The increase in values of velocity with increasing concentrations indicates the increase in cohesive forces due to solute–solvent interactions, intermolecular attractions and macromolecular motion in solution which is also evidence for the possibility of H-bond formation between solute and solvent. Thus, this increase in ultrasonic velocity may be due to strong dipole–dipole interactions. Increasing value of density with increasing concentration suggests increase in solvent–solvent and solute–solvent interaction due to structure making ability of solute in presence of solvent. Adiabatic compressibility indicates relative change of volume of a liquid with change in pressure or under stress. Higher the values of compressibility, lower will be the intermolecular attractive forces such as dipole–dipole, hydrogen bonding, etc. The distance between the surfaces of the adjacent molecules is called as free length or intermolecular free length. Intermolecular free length ( $L_r$ ) changes because of intermolecular attraction or repulsion. Decrease in values of intermolecular free length with

increasing concentration suggests significant interaction among solute and solvent molecules because as number of ions or particles increases in solution, the gap (intermolecular free length) between two species decreases. Acoustic impedance is the ratio of instantaneous pressure excess at any particle in medium to instantaneous velocity of that particle in medium. The increasing acoustic impedance values also supports effective solute–solvent interactions. The increasing values of apparent molar volume with increase in concentration also confirms the strong solute–solvent and ion–solvent interactions. The values of Rao's constant and Wada's constant variation indicates the changes in molecular interaction. Surface tension is used for the study of surface composition in aqueous solution. A variation of the surface tension supports the effective interactions between the solute and solvent. Graphical representation of various thermo-acoustical parameters shows that there is non-linear variation of these parameters for all the studied binary systems under study over the whole composition and temperature. The deviation from linearity in all the above cases also indicates a strong solute–solvent interaction. On addition of solute in solvents, non-specific physical interactions and unfavorable interactions between unlike component molecules come into play thereby giving the non-linear variation in various thermo-acoustical parameters at different temperature and concentration of binary solvent mixtures.

### *2-(1,3-Dioxo-1,3-dihydro-2H-isoindol-2-yl)-4-methylpentanoic Acid (N-Phthaloylleucine) (NPT-LU)*

The increasing values of ultrasonic velocity, density, acoustic impedance, surface tension with increase in concentration and decreasing values of adiabatic compressibility as well as intermolecular free length suggest strong interaction between solute and solvent.

**Table 2.** IR absorption frequency,  $\text{cm}^{-1}$ 

S.N.	Compound	Solute	Solute + polar solvent	Solute + nonpolar solvent
1	NPTLU	2953.51	3349.74	3402.38
2	C-BI-NO <sub>2</sub> -L	3500	3330.38	3667.79
3	C-BI-NO <sub>2</sub> -G	3500	3346	3851.41
4	C-BI-CL-L	3554.30	3741	3741
5	C-QA-PR	3433.02	3334.57	3407.85
6	C-QA-GL	3412.44	3401.60	3328.60

#### *Benzimidazole Derivatives*

For all solutions (C-BI-CL-L, C-BI-NO<sub>2</sub>-L, C-BI-NO<sub>2</sub>-G in Ethanol and DMSO) density, velocity, acoustic impedance, molar volume, surface tension Rao's constant and Wada's constant increases with increase in concentration. Adiabatic compressibility as well as Intermolecular free length decreases with increase in concentration. This indicates strong intermolecular interaction which supports interactions between solute-solute and solvent-solvent molecules. In other words, it is evidence of interactions between molecules in the solution. The non-linear trend for acoustical parameters is may be due to more interactions between solute-solute and solvent-solvent molecules as compared to solute-solvent molecules.

#### *Quinaxaline Derivatives*

For solutions of C-QA-GL and C-QA-PR in ethanol. Values of density, velocity, acoustic impedance, Rao's constant, Wada's constant, molar volume, surface tension increases and adiabatic compressibility as well as the intermolecular free length decreases with increase in concentration. This indicates strong intermolecular interaction. For solutions of C-QA-GL in DMSO, density, velocity, acoustic impedance, molar volume, surface tension except Rao's constant and Wada's constant, increases with increase in concentration. Adiabatic compressibility as well as Intermolecular free length decreases with increase in concentration. This supports interactions between solute-solute and solvent- molecules. For solutions of C-QA-PR in DMSO, density, velocity, acoustic impedance, molar volume, surface tension, Rao's constant (except at 303 and 318 K) and Wada's constant (except at 303 and 318 K) increases with increase in concentration. Adiabatic compressibility as well as Intermolecular free length decreases with increase in concentration. This is also evidence of interactions between molecules in the solution. The non-linear trend for acoustical parameters is may be due to more interactions between solute-solute and solvent-solvent molecules as compared to solute-solvent molecules.

**FTIR spectral analysis.** Results of ultrasonic velocity measurement are further supported by FTIR spec-

tral study (Table 2). The change in values of transmittance and shift in values of frequency of representative peaks –OH and other functional groups present in the compounds in FTIR spectra gives information about molecular interaction which leads to the complex formation among solute and solvent. The variation of ultrasonic velocity and other parameters may be explained on the basis of hydrogen bond formation between solute and solvent. Here all solutes has carbonyl/ hydroxyl/ carboxylic acid functional group and solvent has hydroxyl/carbonyl functional group. So hydrogen bonding between solute and solvent is possible. In these figures, frequency is expressed in terms of wave number. In IR spectra, when solute dissolved in solvent (ethanol/DMF/DMSO) then its IR absorption frequency is found to be different from the value of IR absorption frequency of pure solute. Alteration in frequency in presence of solvents supports hydrogen bonding among solute and solvent. Although, various oxygen and nitrogen atoms are there in the structure of the compound, which are also available for hydrogen bonding with the hydrogen atom in –O–H group of ethanol. It is seen from the FTIR spectrum of binary mixture that, shift in frequency of –OH group is more pronounced as that of other groups. Therefore, it can be concluded that the –OH group form a hydrogen bond. The complex formation can be explained through the molecular structures of compounds and solvent.

#### CONCLUSION

Ultrasonic studies of NPTLU, C-BI-NO<sub>2</sub>-L, C-BI-NO<sub>2</sub>-G, C-BI-CL-L, C-QA-PR, and C-QA-GL studied in solution of polar and non-polar solvent of various concentrations at different temperatures viz. 303, 308, 313, and 318 K with a view to understand molecular interactions in these solutions. Ethyl alcohol and DMSO/DMF chosen as polar and non-polar solvents respectively. The interaction between the molecules of liquids takes place because of presence of various types of forces such as dispersion forces, charge transfer, hydrogen bonding, dipole-dipole and dipole-induced dipole interactions. We determined density and ultrasonic velocity of *N*-phtaloyl amino acid analogue at different concentration and temperature. Various acoustical parameters such as adiabatic

compressibility, intermolecular free length, Rao's constant, acoustic impedance, relaxation time, surface tension, molar volume, absorption coefficient, free volume, and free length calculated from the experimental velocity and density measurements. Thus the variation of different parameters with temperature and concentration shows the molecular interaction is taking place between the solute molecules in the liquid mixtures. The acoustical and thermodynamic parameters calculated from measured properties suggest the strong molecular interaction in the solution. All the experimental determinations of adiabatic compressibility ( $\beta$ ), molar volume ( $V$ ), free length ( $L_f$ ), acoustic impedance ( $Z$ ), Wada's constant ( $W$ ), and Rao's constant ( $R$ ) are strongly correlated with each other. The solute–solute molecular association takes place due to dipole – interaction and the polar nature of different molecular species in the mixture. The solute–solvent association takes place due to slightly polar solute and polar/nonpolar nature of the solvent. The association in this mixture is the result of hydrogen bonding in the binary liquid mixtures. The natures of intermolecular interaction explained on the basis of variation of acoustical parameter and infrared analysis.

For NPTLU, the interaction of solute with DMSO is stronger than ethanol since values of acoustical parameters are more for DMSO since value of density, acoustic impedance, Wada's constant, surface tension are high for DMSO and adiabatic compressibility is low for DMSO.

For benzimidazole derivatives (C-BI-CL-L, C-BI-NO<sub>2</sub>-L, and C-BI-NO<sub>2</sub>-G) values of acoustical parameters i.e., velocity, Rao's constant ( $R$ ), Wada's constant ( $W$ ), molar volume ( $V_m$ ), except acoustic impedance ( $Z$ ) and surface tension ( $S$ ) are higher for DMF than ethanol. On the other hand, values of adiabatic compressibility ( $\beta_{ad}$ ) and intermolecular free length ( $L_f$ ) of all the three solutes are higher in ethanol. This indicates the occurrence of strong interaction between solute (C-BI-CL-L, C-BI-NO<sub>2</sub>-L, C-BI-NO<sub>2</sub>-G) and DMF. The association in this solution is due to hydrogen bonding between solute and solvent. An analysis of these values suggests strong intermolecular interaction which may be due to hydrogen bond, dipole–dipole interaction, and hyperconjugation. Thus, the concept of intermolecular interaction studied on the basis of variation of acoustical parameter.

For quinaxoline derivatives, (C-QA-GL and C-QA-PR), the values of parameters velocity, density, acoustic impedance ( $Z$ ), Rao's constant ( $R$ ), Wada's constant ( $W$ ), molar volume ( $V_m$ ), surface tension ( $S$ ), of C-QA-GL are higher for DMSO than ethanol

except density, acoustic impedance and surface tension. On the other hand, values of adiabatic compressibility ( $\beta_{ad}$ ) and intermolecular free length ( $L_f$ ) of C-QA-GL are higher in ethanol. All the values of acoustical parameters except molar volume of C-QA-PR are higher for DMSO than ethanol. Conversely, values of adiabatic compressibility ( $\beta_{ad}$ ) and intermolecular free length ( $L_f$ ) of C-QA-PR are higher in ethanol. This indicates the occurrence of strong interaction between solute (C-QA-PR and C-QA-GL) and DMSO.

Moreover, the molecular interaction between solute and solvents confirmed by FTIR study which shows alternation in –OH group frequency (expressed in terms of wave number) when solute dissolves in solvents, which may be due to the presence of hydrogen bonding. It can also be concluded that molecular interactions in the ethanol and DMSO/DMF solution of all solutes are due to complex formation on the basis of hydrogen bonding. This property is directly responsible for the increase in potency of the drug and shows good effectiveness of the drug. So, these compounds possess remarkable and noticeable acoustical property.

## REFERENCES

1. P. Tekade, S. Lohakare, S. Bajaj, and R. Naik, *Russ. J. Phys. Chem. A* **89**, 2105 (2015).  
<https://doi.org/10.1134/S0036024415110187>
2. R. R. Naik, S. V. Bawankar, P. V. Tekade, and O. A. Mahodaya, *Russ. J. Phys. Chem. A* **89**, 152 (2015).  
<https://doi.org/10.1134/S0036024415010227>
3. S. D. Kukade, S. K. Singh, R. R. Naik, and S. V. Bawankar, *J. Mol. Liq.* **222**, 225 (2016).  
<https://doi.org/10.1016/j.molliq.2016.07.059>
4. S. J. Kharat, *J. Mol. Liq.* **140**, 10 (2008).  
<https://doi.org/10.1016/j.molliq.2007.12.006>
5. A. Pal and S. Kumar, *J. Mol. Liq.* **121**, 148 (2005).  
<https://doi.org/10.1016/j.molliq.2004.12.003>
6. S. Schlücker, J. Koster, R. K. Singh, and B. P. Asthana, *J. Phys. Chem. A* **111**, 5185 (2007).  
<https://doi.org/10.1021/jp0702292>
7. S. Kubo and J. F. Kadla, *Biomacromolecules* **6**, 2815 (2005).  
<https://doi.org/10.1021/bm050288q>
8. J. Zhang, F. Han, X. Wei, L. Shui, H. Gong, and P. Zhang, *Ind. Eng. Chem. Res.* **49**, 2025 (2010).  
<https://doi.org/10.1021/ie9014759>
9. K. Mizuno, S. Imafuji, T. Ochi, T. Ohta, and S. Maeda, *J. Phys. Chem. B* **104**, 11001 (2000).  
<https://doi.org/10.1021/jp001079x>
10. F. Schwager, E. Marand, and R. M. Davis, *J. Phys. Chem.* **100**, 19268 (1996).  
<https://doi.org/10.1021/jp9613448>

## RESEARCH ARTICLE

Luminescence study of LiMgBO<sub>3</sub>:Dy for  $\gamma$ -ray and carbon ion beam exposureMangesh M. Yerpude<sup>1</sup> | Vibha Chopra<sup>2</sup>  | N.S. Dhoble<sup>3</sup> | R.M. Kadam<sup>4</sup> | Aleksander R. Krupski<sup>5</sup> | S.J. Dhoble<sup>1</sup> <sup>1</sup>Department of Physics, R.T.M. Nagpur University, Nagpur 440033, India<sup>2</sup>P.G. Department of Physics and Electronics, DAV College, Amritsar 143001, Punjab, India<sup>3</sup>Department of Chemistry, Sevalal Mahila Mahavidyalaya, Nagpur 440009, India<sup>4</sup>Radiochemistry Division, Bhabha Atomic Research Centre, Trombay, India<sup>5</sup>Faculty of Science, SEES, University of Portsmouth, Portsmouth PO1 3QL, UK**Correspondence**Vibha Chopra, P.G. Department of Physics and Electronics, DAV College, Amritsar - 143001, Punjab, India.  
Email: vibhachopra04@gmail.com**Funding information**

IUAC; University Grants Commission-India, Grant/Award Number: UGC-NET-JRF

**Abstract**

LiMgBO<sub>3</sub>:Dy<sup>3+</sup>, a low  $Z_{\text{eff}}$  material was prepared using the solution combustion method and its luminescence properties were studied using X-ray diffraction (XRD), scanning electron microscopy (SEM), thermoluminescence (TL), photoluminescence (PL), Fourier transform infrared spectroscopy, and electron paramagnetic resonance (EPR) techniques. Reitveld refinement was also performed for the structural studies. The PL emission spectra for LiMgBO<sub>3</sub>:Dy<sup>3+</sup> consisted of two peaks at 478 nm due to the <sup>4</sup>F<sub>9/2</sub>→<sup>6</sup>H<sub>15/2</sub> magnetic dipole transition and at 572 nm due to the hypersensitive <sup>4</sup>F<sub>9/2</sub>→<sup>6</sup>H<sub>13/2</sub> electric dipole transition of Dy<sup>3+</sup>, respectively. A TL study was carried out for both the  $\gamma$ -ray-irradiated sample and the C<sup>5+</sup> irradiated samples and was found to show high sensitivity for both. Moreover the  $\gamma$ -ray-irradiated LiMgBO<sub>3</sub>:Dy<sup>3+</sup> sample showed linearity in the dose range 10 Gy to 1 kGy and C<sup>5+</sup>-irradiated samples show linearity in the fluence range  $2 \times 10^{10}$  to  $1 \times 10^{11}$  ions/cm<sup>2</sup>. In the present study, the initial rise method, various heating rate method, the whole glow curve method, glow curve convolution deconvolution function, and Chen's peak shape method were used to calculate kinetic parameters to understand the TL glow curve mechanism in detail. Finally, an EPR study was performed to examine the radicals responsible for the TL process.

**KEYWORDS**ESR, LiMgBO<sub>3</sub>, tissue equivalent material, trapping parameters**1 | INTRODUCTION**

Boron-based materials show interesting thermoluminescence (TL) properties when exposed to ionizing radiation<sup>[1,2]</sup>. The luminescence properties of lithium borate and magnesium borate in both microcrystalline and nanocrystalline forms have been studied previously<sup>[1-4]</sup>. Recently, researchers who studied lithium magnesium borate phosphor found that it was useful for applications in dosimetry<sup>[5,6]</sup>.

To date, only a few studies on LiMgBO<sub>3</sub> have been reported<sup>[5]</sup>. Recently, the TL properties of rare earth ion (RE = Tb, Gd, Dy, Pr, Mn, Ce, Eu)-doped lithium magnesium borate (LMB), prepared using

the solid state diffusion method, have been documented<sup>[6]</sup>. LMB:Tb<sup>3+</sup> showed the best results with a stable TL peak at 240°C. LMB:Tb<sup>3+</sup> was about four times more sensitive than TLD-100. Optical properties of LMB glasses doped with Dy<sup>3+</sup>, Sm<sup>3+</sup> ions have been studied<sup>[7]</sup>. Photoluminescence properties of LMB:Eu and LMB:Eu,Bi have also been studied in detail<sup>[8]</sup>. LiMgBO<sub>3</sub>:Dy<sup>3+</sup> in its polycrystalline form has been prepared using a novel solution combustion method and its TL sensitivity was found to be half compared with commercial TLD-100 and showed a high degree of fading of 30% after 20 days<sup>[9]</sup>. Furthermore, LiMgBO<sub>3</sub>:Dy<sup>3+</sup> in its nanocrystalline form has been prepared using the combustion method and its structural and optical properties have been studied<sup>[10]</sup>.

There have been no previous reports in the published literature on the study of the luminescence properties of LMB synthesized using the solution combustion method using present precursors, and also no reports on ion beam dosimetry with the same material. Recently, in the field of cancer treatment, heavy ion radiotherapy compared with photon therapy has attracted attention<sup>[11,12]</sup>. Heavy ions show low energy straggling and strong increase in their linear energy transfer (LET) in the affected region<sup>[12-16]</sup>. Among the heavy ions, carbon ions are most significant due to increase in LET and the size of carbon ions is such that they cause much damage to the cancer cell, but relatively little damage to healthy cells nearby<sup>[12]</sup>. The effective atomic number of LiMgBO<sub>3</sub> was calculated using the formula:

$$Z_{\text{eff}} = \sqrt[2.94]{f_1 \times (Z_1)^{2.94} + f_2 \times (Z_2)^{2.94} + f_3 \times (Z_3)^{2.94} + f_4 \times (Z_4)^{2.94}} \quad (1)$$

where.

$f_n$  = fraction of total number of electrons associated with each element,

$Z_n$  = atomic number of each element.

It was found that LiMgBO<sub>3</sub> had a low effective atomic number ( $Z_{\text{eff}} \approx 8.8$ ) close to that of biological tissue ( $Z_{\text{eff}} = 7.4$ ), therefore this material can be studied for its dosimetric properties. In the present study, LiMgBO<sub>3</sub> doped with Dy was synthesized using the solution combustion method with different starting materials than reported previously<sup>[9]</sup>. The synthesized samples were irradiated with a  $\gamma$ -ray dose and their luminescence properties were studied using photoluminescence (PL) and electron paramagnetic resonance (EPR) techniques. Finally the TL characteristics of  $\gamma$ -ray- and C<sup>5+</sup> ion beam-exposed samples were studied to find their suitability for application in radiation dosimetry.

## 2 | EXPERIMENTAL

### 2.1 | Synthesis

The solution combustion method was used to prepare Dy<sup>3+</sup> activated with LiMgBO<sub>3</sub>. All analytical reagent (AR) grade precursors: LiNO<sub>3</sub>, Mg(NO<sub>3</sub>)<sub>2</sub>, H<sub>3</sub>BO<sub>3</sub>, and NH<sub>2</sub>CONH<sub>2</sub> were weighed in stoichiometric proportion and dissolved in double-distilled water with constant stirring. Dysprosium nitrate was added by dissolving Dy<sub>2</sub>O<sub>3</sub> in dilute nitric acid at the desired concentration for doping. The prepared mixture was heated by placing on a hot plate at a constant temperature of 80°C with constant stirring. The formed gel was then transferred to a preheated muffle furnace at 500°C. An exothermic reaction took place and a white foamy powder was obtained in the crucible. The foamy powder was crushed to fine particles and was heated in a muffle furnace at 700°C for 2 h and allowed to cool slowly. Later the sample was annealed at 700°C for 1 h and quenched quickly to room temperature by putting it on a metal block. The final product obtained was studied for its different luminescence properties.

### 2.2 | Characterization

For characterization of the synthesized materials, X-ray diffraction (XRD), TL, PL, ESR techniques have been used. The XRD pattern was recorded using a diffractometer with Cu-K $\alpha$  radiation ( $\lambda = 1.5406 \text{ \AA}$ ) at a 40 kV tube voltage on a Rigaku instrument with a step size of  $2\theta = 0.02^\circ$ . Furthermore, for SEM, a JEOL 6380 A instrument was used to study the surface morphology of the synthesized sample. Fourier transform infrared (FTIR) spectra from the prepared phosphor were recorded using a Shimadzu IR Affinity-1 spectrophotometer. PL measurements were taken using an RF-5301PC spectrofluorophotometer with a xenon lamp as the excitation source. EPR measurements were performed using a Bruker EMM-1843 spectrometer operating at an X-band frequency of 9.43 GHz. About 150 mg of LiMgBO<sub>3</sub>:Dy<sup>3+</sup> sample was used to record the EPR spectra and the sample was exposed to a 1 kGy dose of  $\gamma$ -rays from a <sup>60</sup>Co source before EPR measurements. For the TL measurements, the synthesized samples were irradiated with  $\gamma$ -rays or a 75 MeV C<sup>5+</sup> ion beam.  $\gamma$ -Ray exposure was carried out using a calibrated <sup>60</sup>Co source or C<sup>5+</sup> ion beam exposure was carried out using a 16MV tandem Van de Graaff-type electrostatic accelerator (15 UD Pelletron)<sup>[17]</sup> at

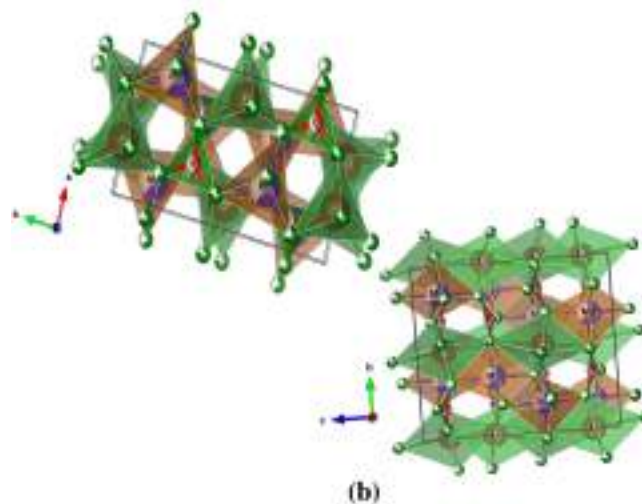
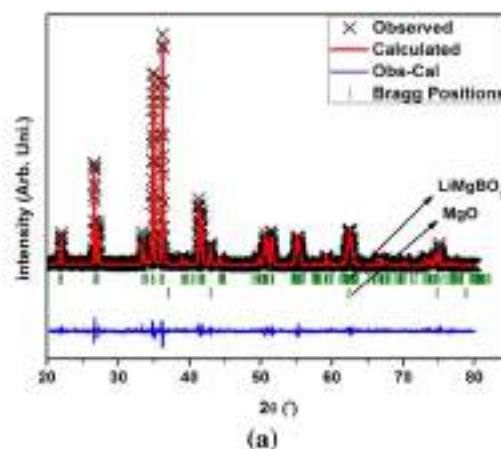


**FIGURE 1** (a) Rietveld refined X-ray diffraction pattern; (b) crystal structure of monoclinic LiMgBO<sub>3</sub> phosphor

the Inter-University Accelerator Center (IUAC), New Delhi, India. After irradiation, TL measurements were recorded using a Nucleonix TLD reader (model: 1009I) taking 5 mg of sample every time.

### 3 | RESULTS AND DISCUSSION

#### 3.1 | Structure analysis

The Rietveld refined XRD pattern of monoclinic  $\text{LiMgBO}_3$  (97%) with a secondary cubic MgO (3%) phase is shown in Figure 1(a). The XRD pattern is consistent with the standard pattern depicting the pure monoclinic phase with space group  $C2/c$ <sup>[10]</sup>. The diffraction peaks were indexed according to the JCPDS file (00-079-1996)<sup>[10]</sup>. Furthermore, addition of dopant  $\text{Dy}^{3+}$  (activator) did not affect the crystal structure of the host lattice. For the determination and refinement of lattice parameters, Rietveld XRD profile fitting was performed using FULLPROF software. Initial parameters were taken from the already reported structural characterization of  $\text{LiMgBO}_3$ <sup>[5]</sup>. The calculated lattice parameters were approximated to be  $a = 5.168 \text{ \AA}$ ,  $b = 8.887 \text{ \AA}$ ,  $c = 9.916 \text{ \AA}$ ,  $\beta = 91.20^\circ$  and  $V = 455.322 \text{ \AA}^3$ <sup>[10]</sup>. The Rietveld refinement parameters are listed in Table 1. The crystal structure of  $\text{LiMgBO}_3$  is shown in Figure 1(b). Norrestem *et al.* showed that the Li atom in  $\text{LiMgBO}_3$  occupied a disordered position, allowing the lithium atom to occupy two positions around the initial average position<sup>[5]</sup>. But, in the present study, a more ordered position for the lithium atom with bonds elongated along the  $c$ -axis was observed. The Li position has a triangular coordination using the three O atoms with very short bond distances of about  $1.9 \text{ \AA}$ , further away (about  $2.7 \text{ \AA}$ ) there were two more O atoms so that a  $3 + 2$  coordination in the form of an elongated trigonal bi-pyramidal coordination polyhedron was obtained. The Li and Mg atoms were five-coordinated using an oxygen atom to form a distorted trigonal bi-pyramidal coordination polyhedron.

**TABLE 1** Rietveld refinement parameters for monoclinic  $\text{LiMgBO}_3$

Empirical formula						$\text{LiMgBO}_3:\text{Dy}^{3+}$
Crystal system and space group						Monoclinic, $C2/c$ (15)
Unit cell parameters						$a = 5.168 \text{ \AA}$ , $b = 8.887 \text{ \AA}$ , $c = 9.916 \text{ \AA}$ , $\beta = 91.22^\circ$
Volume						$V = 455.322 \text{ \AA}^3$
Calculated density						$2.194 \text{ g/cm}^3$
Goodness of fit ( $\chi^2$ )						1.41
Reliability factors						$R_p = 10.7$ , $R_{wp} = 14.9$ , $R_{exp} = 12.5$
Atom	x	y	z	Occupancy	B	
Li	0.1427	0.5167	0.1151	0.972	4.327	
Mg	0.1625	0.1708	0.1261	0.7635	1.571	
Dy	0.1625	0.1708	0.1261	0.0016	2.189	
B	0.1702	0.8480	0.1296	0.5941	1.443	
O <sub>1</sub>	0.2753	0.6939	0.1621	0.8515	2.134	
O <sub>2</sub>	0.3095	0.9553	0.1294	0.8565	2.382	
O <sub>3</sub>	0.4056	0.3299	0.0857	0.8677	2.725	

$\text{LiO}_5$  polyhedrons were interconnected by two oxygen atoms forming layers parallel to the  $c$ - $a$  plane distributed along the  $b$ -axis. The  $\text{MgO}_5$  polyhedrons shared two oxygen atoms with other  $\text{MgO}_5$  polyhedrons forming diagonal layers. These  $\text{LiO}_5$  and  $\text{MgO}_5$  layers were linked together by edge and shared into zig-zag rows extending in the diagonal  $c$ - $a$  direction. The Li and B ions linked these rows together into a three-dimensional network.

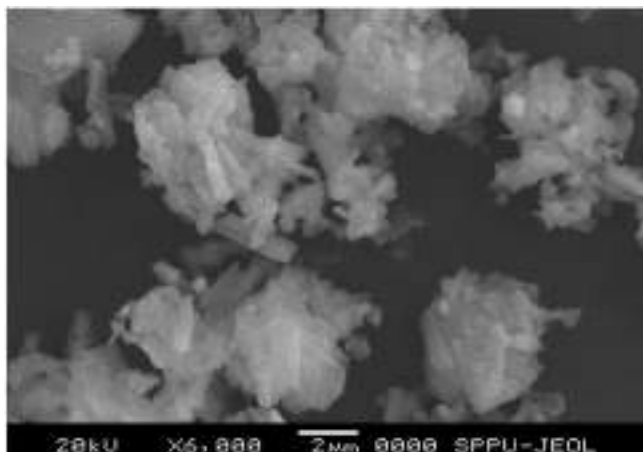
Figure 2 shows the SEM photographs from the  $\text{LiMgBO}_3:\text{Dy}^{3+}$  phosphor and clearly indicated agglomeration with rod shapes distributed widely. The morphology of the powder was observed to be polycrystalline, made of microcrystalline particles. Voids and pores seen in the SEM images were due to the production of combusting gases during the sol-gel combustion process<sup>[9]</sup>.

#### 3.2 | Fourier transform (FTIR) analysis

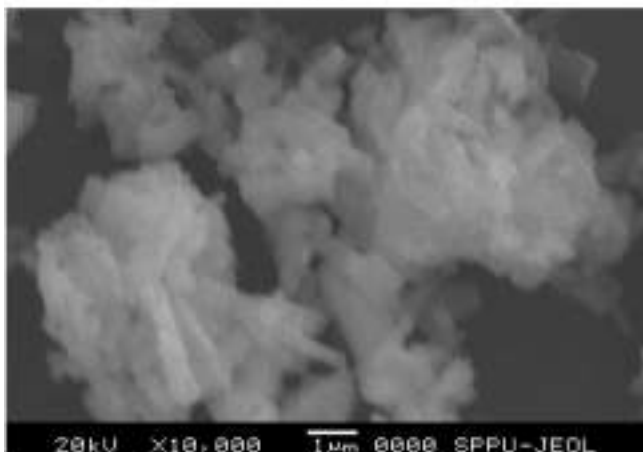
FTIR spectra of the synthesized phosphor  $\text{LiMgBO}_3:\text{Dy}^{3+}$  prepared using the solution chemical route are displayed in Figure 3. The spectra were recorded for the mid-infrared region  $400 \text{ cm}^{-1}$  to  $4000 \text{ cm}^{-1}$  using transmittance mode. Bands at  $1458 \text{ cm}^{-1}$  and  $1287 \text{ cm}^{-1}$  corresponded to asymmetric stretching relaxations of the B-O bond in the trigonal  $\text{BO}_3$  unit<sup>[9]</sup>. The band at  $1182 \text{ cm}^{-1}$  showed the symmetrical stretching vibrations of a B-O bond. Bands at  $1025 \text{ cm}^{-1}$  and  $836 \text{ cm}^{-1}$  showed the bending vibrations of borate segments<sup>[18]</sup>. Furthermore, borate deformation and plane bending of the boron-oxygen triangles were expressed by bands at  $704$  and  $676 \text{ cm}^{-1}$ . Finally, bands at wavelengths less than  $450 \text{ cm}^{-1}$  were attributed to lattice vibrations.

#### 3.3 | Photoluminescence (PL)

Photoluminescence spectra were studied to confirm the state of the dopant in the host lattice. The excitation and emission spectra of



(a)



(b)

**FIGURE 2** (a, b) Scanning electron microscopy micrographs of the LiMgBO<sub>3</sub>:Dy<sup>3+</sup> phosphor

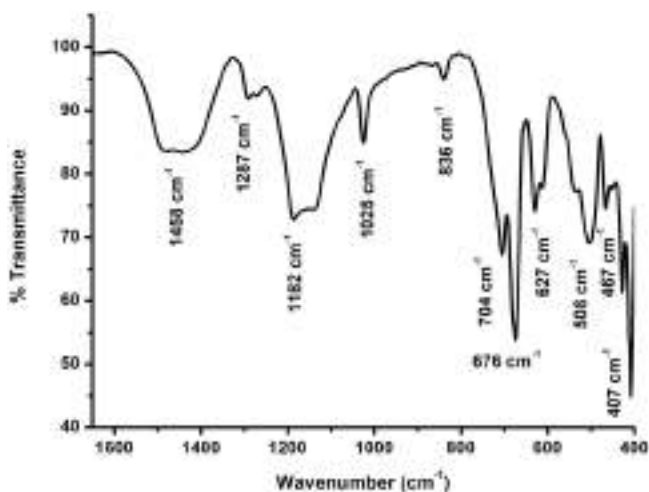
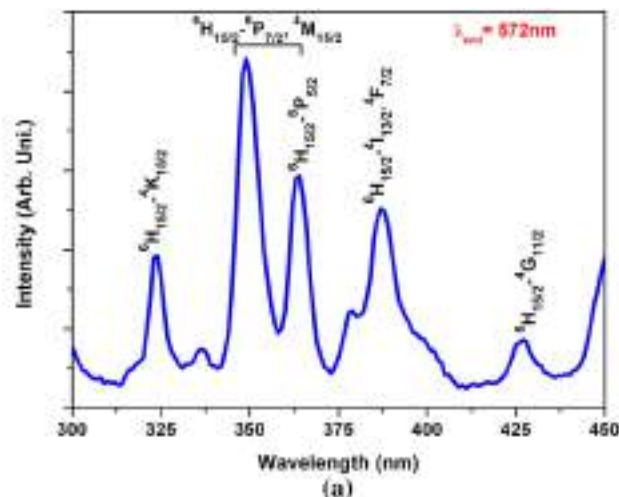
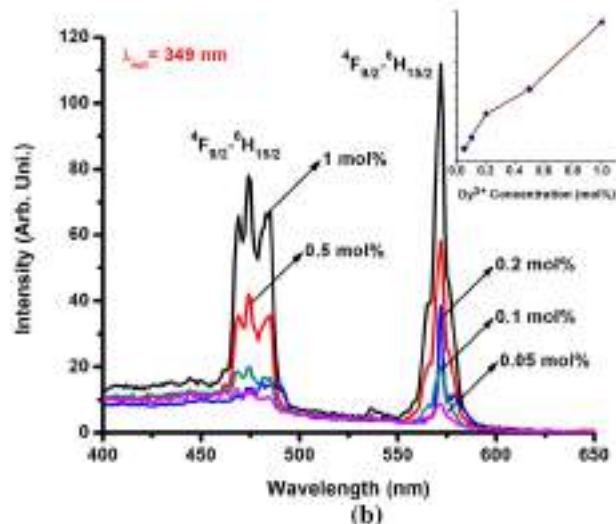


**FIGURE 3** Fourier transform infrared spectrum of the synthesized LiMgBO<sub>3</sub>:Dy<sup>3+</sup> phosphor

synthesized LiMgBO<sub>3</sub>:Dy<sup>3+</sup> are shown in Figure 4(a) and Figure 4(b), respectively. Peaks at 323, 349, 365, 388 and 427 nm were observed in the excitation spectrum monitored at the 572 nm emission that is



(a)



(b)

**FIGURE 4** Photoluminescence (a) excitation; and (b) emission spectra of the LiMgBO<sub>3</sub>:Dy<sup>3+</sup> phosphor

shown in Figure 4(a). Peaks corresponded to  ${}^6\text{H}_{15/2} \rightarrow {}^4\text{K}_{15/2}$ , [ ${}^6\text{H}_{15/2} \rightarrow {}^6\text{P}_{7/2}$ ,  ${}^4\text{M}_{15/2}$ ],  ${}^6\text{H}_{15/2} \rightarrow {}^6\text{P}_{5/2}$ , [ ${}^6\text{H}_{15/2} \rightarrow {}^4\text{I}_{13/2}$ ,  ${}^4\text{F}_{7/2}$ ] and  ${}^6\text{H}_{15/2} \rightarrow {}^4\text{G}_{11/2}$  transitions, respectively. The PL emission spectra of Dy<sup>3+</sup>-doped LiMgBO<sub>3</sub> sample excited at 349 nm wavelength is shown in Figure 4(b). The emission spectra consisted of two peaks centred at 478 nm and 572 nm that were due to the  ${}^4\text{F}_{9/2} \rightarrow {}^6\text{H}_{15/2}$  magnetic dipole transition and the hypersensitive  ${}^4\text{F}_{9/2} \rightarrow {}^6\text{H}_{13/2}$  electric dipole transitions, respectively of Dy<sup>3+</sup>[19,20]. Furthermore, the inset in Figure 4(b) shows that emission intensity increased with increase in Dy<sup>3+</sup> concentration and did not show any concentration quenching until the 1 mol% concentration.

### 3.4 | Thermoluminescence (TL) studies

TL studies of LiMgBO<sub>3</sub>:Dy<sup>3+</sup> were performed after irradiation of the samples with  $\gamma$ -rays and an C<sup>5+</sup> ion beam. The study included the effect of dopant concentration on the TL glow curves and the effect of dose on TL glow curves, the TL response, the effect of various heating rates and the calculation of trapping parameters.

### 3.4.1 | TL studies of $\gamma$ -ray-irradiated $\text{LiMgBO}_3:\text{Dy}$

#### Effect of concentration on TL glow curves

TL glow curves for  $\text{LiMgBO}_3:\text{Dy}^{3+}$  with different  $\text{Dy}^{3+}$  concentrations, and irradiated with a 200 Gy  $\gamma$ -ray dose are shown in Figure 5. A single glow curve was observed due to one type of defect (luminescent centre) for the prepared phosphor with a glow peak at 160°C. TL glow curves were recorded for 0.05, 0.1, 0.2, 0.5 and 1 mol% concentrations of  $\text{Dy}^{3+}$  ions in  $\text{LiMgBO}_3$ . The concentration profile shown in the inset of Figure 5 shows maximum intensity for 0.1 mol% of  $\text{Dy}^{3+}$  ions. With further increase in concentration, the intensity decreased, then became constant. The decrease in TL intensity might have arisen due to concentration quenching of  $\text{Dy}^{3+}$  ions<sup>[21]</sup>. With increase in dopant concentration, the distance between the dopant ions decreased, therefore energy levels of dopant ions perturbed each other to quench each other's emission and causing a decrease in the TL intensity<sup>[22]</sup>. In the present study, a 0.1 mol% concentration of  $\text{Dy}^{3+}$  was found to be the best concentration for studying the TL properties, so this was used for further characterization.

#### Effect of heating rates on TL glow curves

The variation in  $T_m$  with various heating rates of  $\text{LiMgBO}_3:\text{Dy}^{3+}$  is shown in Figure 6. The glow curve occurred at a lower temperature with a maximum TL intensity for a 2°C/s heating rate. As the heating rate increased from 2°C/s to 12°C/s, the glow curve moved towards the higher temperature side and the intensity continued to decrease. However the shape of the glow curve remained unchanged<sup>[23–25]</sup>. The decrease in TL intensity and shift in the peak position towards the higher temperature with increase in heating rate is explained by the theory of thermal quenching<sup>[26,27]</sup>.

#### TL response

To study the dose–response of the prepared phosphor, samples were exposed to different doses ranging from 10 Gy to 1.2 kGy  $\gamma$ -rays using

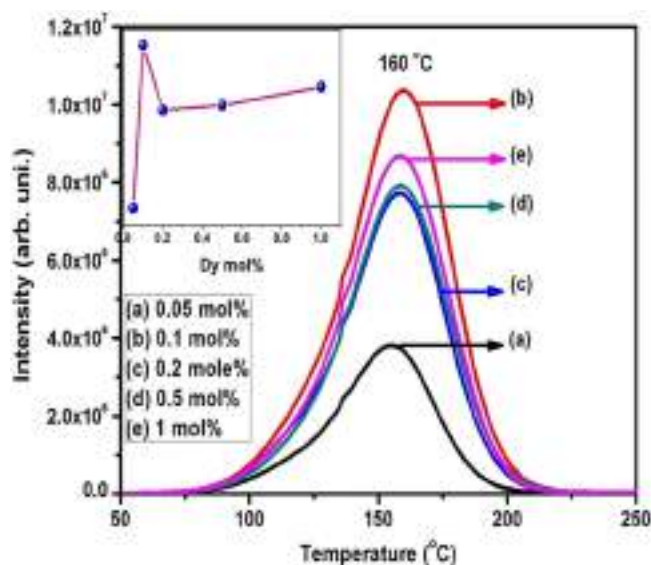


**FIGURE 5** Thermoluminescence glow curves for different concentrations of  $\text{Dy}^{3+}$  in the  $\text{LiMgBO}_3:\text{Dy}^{3+}$  phosphor

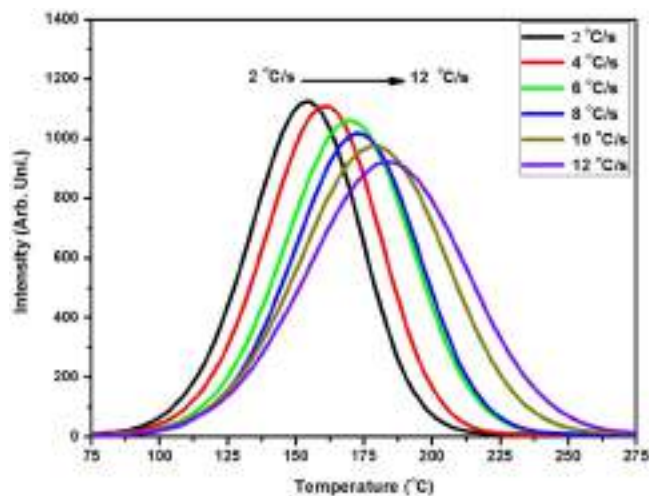


**FIGURE 6** Variation of thermoluminescence glow curves of  $\text{LiMgBO}_3:\text{Dy}^{3+}$  phosphor with various heating rates

a  $^{60}\text{Co}$  source. It was found that the shape and peak temperature of the glow curve remained invariant with varying dose, this is a crucial characteristic for a TLD. Figure 7 shows the TL response of the present phosphor with varying  $\gamma$ -ray doses, the fitted line indicates the linear behaviour of the present phosphor up to a dose of 1 kGy. Further increase in dose resulted in a decrease in intensity and finally saturation at higher doses. This linear TL response can be explained based on the track interaction model<sup>[28,29]</sup>.

#### Trapping parameters

In the present study, trapping parameters were calculated to understand the mechanism of TL glow curve in detail. Different methods used were the initial rise method, the whole glow curve method, the various heating rate method, the glow curve convolution deconvolution function and Chen's peak shape method.

**(a) Initial rise method** Activation energy was estimated using the initial rise method by plotting  $\ln(I)$  and  $1/kT$ , where  $I$  is TL intensity,  $k$

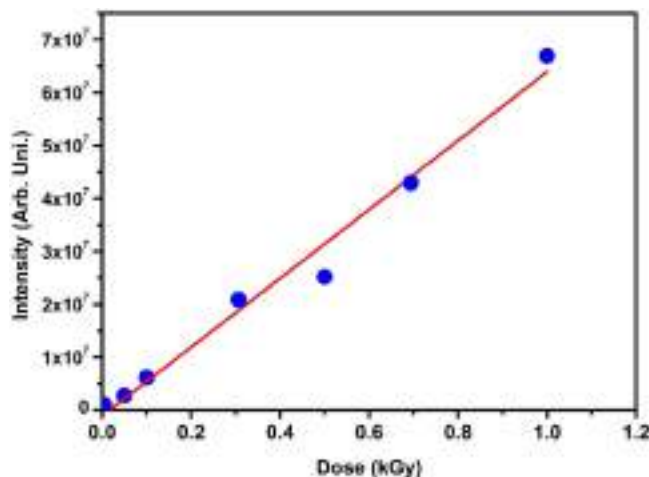


**FIGURE 7** Thermoluminescence response of the  $\text{LiMgBO}_3:\text{Dy}^{3+}$  phosphor with varying  $\gamma$ -ray doses

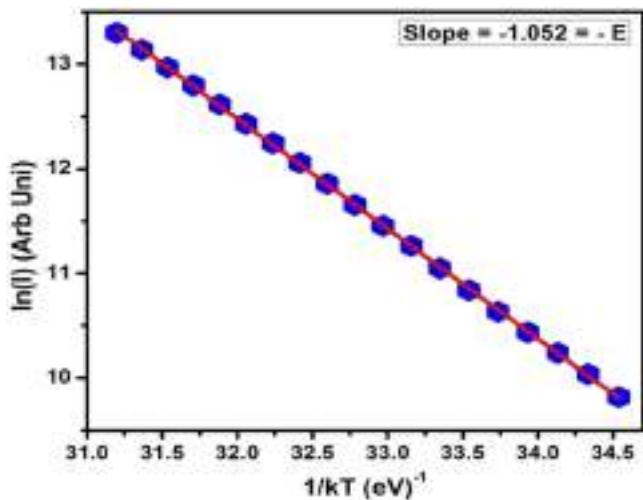


**FIGURE 8** Initial rise portion of a single thermoluminescence glow peak for LiMgBO<sub>3</sub>:Dy<sup>3+</sup> irradiated with a 10 Gy  $\gamma$ -ray dose

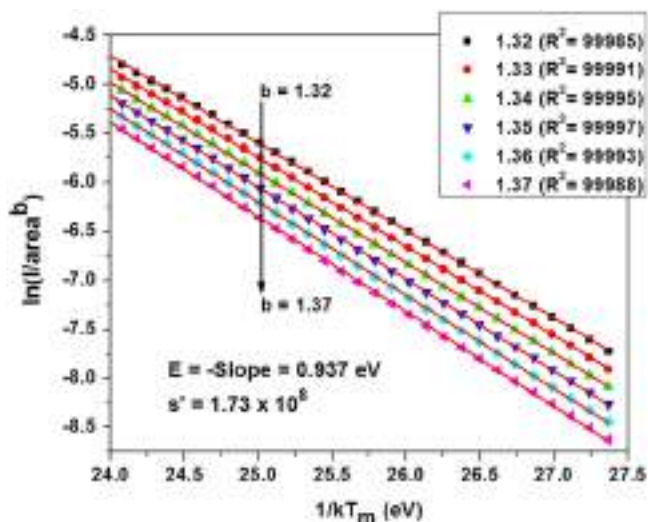


**FIGURE 9** Plot of  $\ln(I/n^b)$  versus  $1/kT$  using the whole glow curve method

is the Boltzmann constant (in eV/K) and  $T$  is the temperature in K<sup>[30]</sup>. The slope of the curve gives the activation energy  $E$ . This method was suggested by Garlic and Gibson<sup>[31]</sup>. The rate of retrapping was negligible for the initial rising portion up to a cut-off temperature  $T_c$ , for which the TL intensity was 15% less than that of the maximum TL intensity<sup>[32]</sup>. Figure 8 shows the initial rise portion of TL glow curve of the sample exposed to a 10 Gy  $\gamma$ -ray dose. The slope of the straight line obtained provided the activation energy  $E$  equal to 1.052 eV.

**(b) Whole glow curve method** The whole glow curve method was used to find the order of kinetics, activation energy and frequency factor<sup>[30]</sup>. This method uses an area of peak to find these trapping parameters.

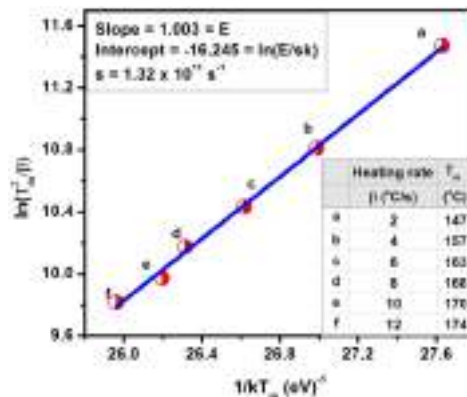


**FIGURE 10** Plot of  $\ln T_m^2/\beta$  against  $1/kT_m$  for the various heating rate method

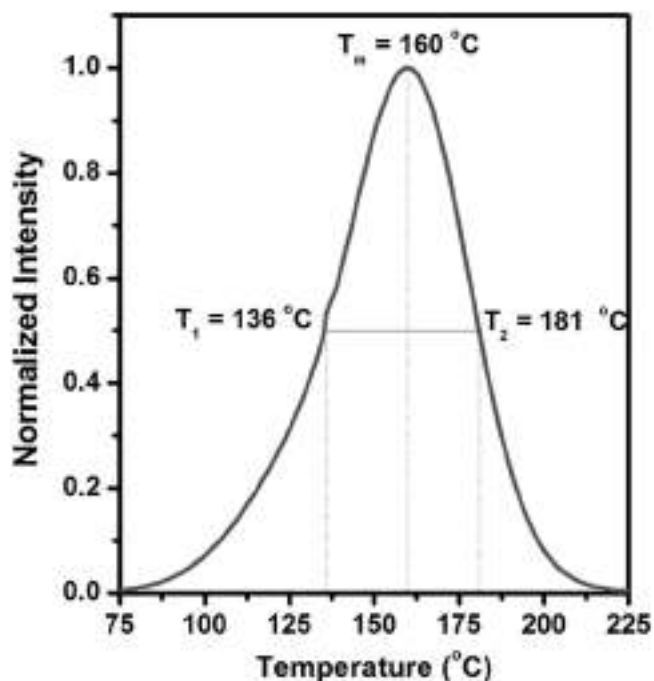


**FIGURE 11** Normalized glow curve showing parameters  $T_1$ ,  $T_2$ ,  $T_m$  for Chen's peak shape method

For general order kinetics, the equation is as follows:

$$\ln\left(\frac{I}{n^b}\right) = \ln\left(\frac{s'}{\beta}\right) - \frac{E}{kT} \quad (2)$$

where  $s'$  is the effective frequency factor for general order kinetics,  $\beta$  is the heating rate and  $b$  is the order of kinetics. For a particular value of  $b$ , the plot of  $\ln(I/n^b)$  versus  $1/kT$  is linear with slope  $-E$  and intercept  $(s'/\beta)$ . For the unknown value of ' $b$ ', several lines were drawn to represent different values of  $b$  and the best straight line was chosen<sup>[33]</sup>. For the present study, Figure 9 shows the plot between  $\ln(I/n^b)$  and  $1/kT$  for some values of  $b$ , out of which

**TABLE 2** Trapping parameters for LiMgBO<sub>3</sub>:Dy irradiated with  $\gamma$ -rays and using Chen's peak shape method

	$\alpha$	$c_\alpha$	$b_\alpha$	$E_\alpha$ (eV)	$s_\alpha$ (s <sup>-1</sup> )
$T_1 = 136^\circ\text{C}$	$\tau = 24$	1.65	1.78	0.978	$7.13 \times 10^{10}$
$T_2 = 181^\circ\text{C}$	$\delta = 21$	1.32	0	1.013	$1.88 \times 10^{11}$
$T_m = 160^\circ\text{C}$	$\omega = 45$	3.00	1	1.001	$1.35 \times 10^{11}$
$\mu_g = 0.47$	$\gamma = 0.88$	Kinetic order $b = 1.42$		Mean $E = 0.997$ eV	Mean $s = 1.31 \times 10^{11}$ s <sup>-1</sup>

$b = 1.35$  showed the best linearity. The  $b$  value shows that the peaks followed general order kinetics. Activation energy was calculated to be 0.937 eV and the frequency factor was  $1.73 \times 10^8$  s<sup>-1</sup>. The results were found to be consistent with the results from the Chen's peak shape method.

**(c) Various heating rate method** The method of various heating rates was suggested to find the values for the trapping parameters<sup>[24]</sup>. The method uses the following relationship:

$$\ln\left(\frac{T_M^2}{\beta}\right) = \frac{E}{kT_M} + \ln\left(\frac{E}{sk}\right) \quad (3)$$

The result suggested that a plot of  $\ln T_M^2/\beta$  against  $1/kT_M$  with slope  $E$  and an intercept of  $\ln(E/sk)$  should be linear, from which  $E$  and  $s$  values can be obtained. Figure 10 shows the plot of  $\ln T_M^2/\beta$  against  $1/kT_M$ . A straight line is obtained and therefore the activation energy was calculated to be 1.003 eV and frequency factor was observed to be  $1.32 \times 10^{11}$  s<sup>-1</sup>. These results were consistent with those of the Chen's peak shape method.

**(d) Chen's peak shape method** The activation energy, order of kinetics and frequency factor can also be determined using Chen's general equations<sup>[32,34]</sup>. Chen's peak shape method needs three temperature values on the peak: the temperature of the TL maximum,  $T_m$ , as well as  $T_1$  and  $T_2$ , which are the temperatures in the ascending and descending parts of the glow curve respectively, for which the TL intensity is a half of the TL at  $T_m$ . Figure 11 shows the normalized glow curve with parameters  $T_1 = 136^\circ\text{C}$ ,  $T_2 = 181^\circ\text{C}$ , and  $T_m = 160^\circ\text{C}$  for Chen's peak shape method. Before calculating the kinetic parameters using Chen's equations, some geometrical parameters,  $\tau$ ,  $\delta$ ,  $\omega$ , were calculated<sup>[17]</sup>. The kinetic parameters calculated from this method are given in Table 2. The values of the symmetry factor ( $\mu_g$ ) and the Balarian parameter ( $\gamma$ ) were found to be 0.47 and 0.88 respectively

**TABLE 3** Comparative study of values of trapping parameters for LiMgBO<sub>3</sub>:Dy irradiated with  $\gamma$ -ray using different methods

Method of calculation	$E$ (eV)	$s$ (s <sup>-1</sup> )	$b$
Chen's peak shape	0.997	$1.31 \times 10^{11}$	1.38
Initial rise	1.052	-	
Various heating rate	1.003	$1.32 \times 10^{11}$	
Whole glow peak method	0.937	$1.73 \times 10^8$	1.35
Curve fitting method	P1 0.99 P2 0.98		1.35 1

and indicated the general order characteristic of TL glow curve. From the relationship between kinetic order ( $b$ ), the geometrical factor ( $\mu$ ) and the Balarian parameter ( $\gamma$ )<sup>[30]</sup>, the value of kinetic order was found to be 1.42. A comparison of the values for trapping parameters from the Chen's peak shape method and the initial rise method is shown in Table 3. Activation energy value using Chen's peak shape method and the initial rise method are almost the same within experimental errors. The value of activation energy using Chen's peak shape method was somewhat less; this might be due to widening of the glow curve due to the presence of less intense traps and the complex nature of the glow curve<sup>[35]</sup>, which are sometimes not distinguishable. The frequency factor by both the methods showed good agreement with each other. The order of kinetics found using Chen's peak shape method was found to be 1.42 and suggested that there might be a possibility of retrapping.

**(e) Glow curve deconvolution method** The trapping parameters of the TL glow curve could be found using the glow curve convolution deconvolution function for first, second, and general order kinetics developed by Kitis *et al.*<sup>[36]</sup>. For applying the glow curve convolution deconvolution function to the experimental value, a rough estimation of values of  $E$  and  $b$  was found using Chen's peak shape method. These values were put in the glow curve convolution deconvolution function and a theoretical curve was generated. The TL glow curve for LiMgBO<sub>3</sub>:Dy<sup>3+</sup> irradiated with a 200 Gy  $\gamma$ -ray dose was deconvoluted to two peaks and is shown in Figure 12. The figure of merit (FOM) value was found to be 1.57 and showed the best fit to the experimental and theoretically generated curve. Activation energy and frequency factor values were found to be consistent with the values obtained from Chen's peak shape method.

### Reproducibility

Reproducibility of the synthesized LiMgBO<sub>3</sub>:Dy material was studied by carrying out repeated post read-out annealing at 400°C for 10 min, seven times at 50 Gy dose every time. Reproducibility results are shown in Figure 13. It was found that the TL response reduced to less than 10% in first five readouts and then reduced to 23% after seven cycles.

### 3.4.2 | TL studies of C<sup>5+</sup> ray-irradiated LiMgBO<sub>3</sub>

LiMgBO<sub>3</sub>:Dy<sup>3+</sup> samples were irradiated with a 75 MeV C<sup>5+</sup> ion beam and the TL glow curves were studied for different concentrations of Dy and are shown in Figure 14. The glow curve shows two peaks, a prominent peak at 148°C and another at 255°C compared with the TL

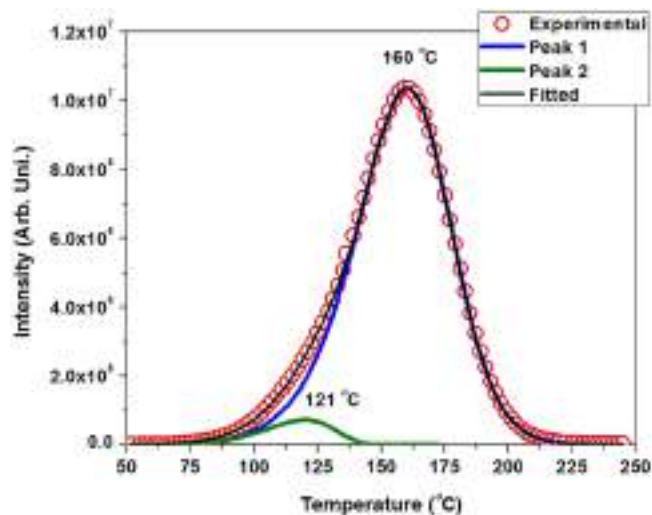


**FIGURE 12** Deconvolution of the thermoluminescence glow curve for  $\text{LiMgBO}_3:\text{Dy}^{3+}$  irradiated with a 200 Gy  $\gamma$ -ray dose

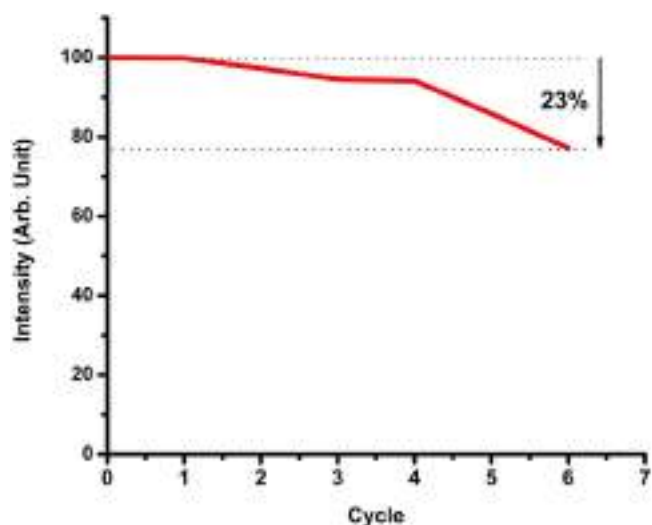


**FIGURE 13** Reproducibility of the synthesized  $\text{LiMgBO}_3:\text{Dy}$  phosphor

glow curve for  $\gamma$ -ray-exposed samples that showed single peak at 160°C. Heavy carbon ions lost their whole energy after penetrating the phosphor, this action perturbed the normal lattice site and therefore altered the trapping mechanism and resulted in the generation of new trap centres that caused the peak at 255°C<sup>[12,37]</sup>. The present phosphor showed a maximum TL intensity at 0.7 mol% of Dy when exposed to the  $\text{C}^{5+}$  ion beam fluence  $1 \times 10^{11}$  ions/cm<sup>2</sup>. Furthermore, the TL glow curves were observed at different fluence ranges for the  $\text{C}^{5+}$  ion beam from  $2 \times 10^{10}$  ions/cm<sup>2</sup> to  $1 \times 10^{12}$  ions/cm<sup>2</sup>, as shown in Figure 15. With increase in fluence up to  $1 \times 10^{11}$  ions/cm<sup>2</sup>, the TL intensity increased and then decreased after further increase. With increase in radiation dose, traps were increasingly filled and then, on thermal stimulation, traps released their charge carriers

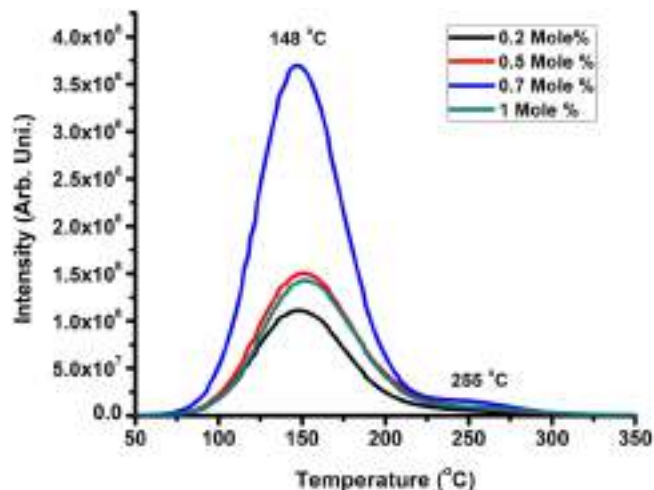


**FIGURE 14** Thermoluminescence glow curves recorded for different concentrations of Dy in the  $\text{LiMgBO}_3:\text{Dy}^{3+}$  samples exposed to a MeV of  $\text{C}^{5+}$  ion beam

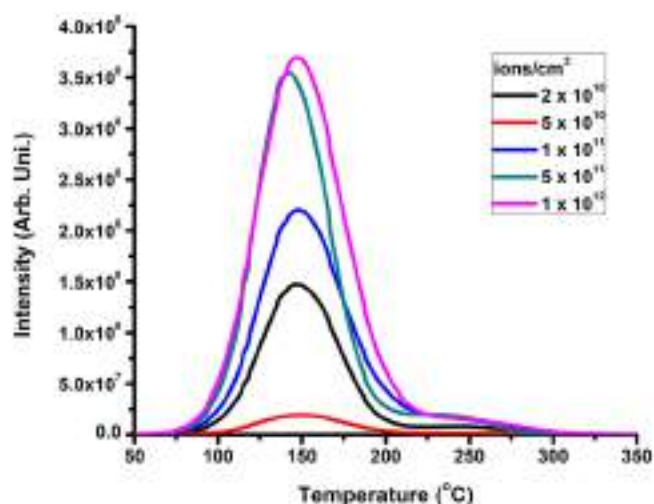


**FIGURE 15** Thermoluminescence glow curves of  $\text{LiMgBO}_3:\text{Dy}^{3+}$  exposed to different fluence ranges of  $\text{C}^{5+}$  ion beams

to finally recombine with their counterparts and give rise to an increase in the TL intensity of the glow peak<sup>[38]</sup>. The TL response curve for the  $\text{C}^{5+}$  ion beam-irradiated  $\text{LiMgBO}_3:\text{Dy}^{3+}$  samples is shown in Figure 16, which shows that the TL response was linear in the range  $2 \times 10^{10}$  to  $1 \times 10^{11}$  ions/cm<sup>2</sup> and then decreased. Therefore, the phosphor was useful in the respective range for  $\text{C}^{5+}$  ion irradiation. Fading of the synthesized material for  $\gamma$ -ray and  $\text{C}^{5+}$  beam exposure is shown in Figure 17. To study fading, samples were irradiated with 50 Gy for  $\gamma$ -rays and  $1 \times 10^{11}$  ions/cm<sup>2</sup> for  $\text{C}^{5+}$  ion beams and then samples were stored for 27 days in the dark. The results in Figure 17 revealed that fading for  $\gamma$ -ray-exposed and carbon beam-exposed sample for first 3 days was approximately 30%, however on fifth day fading remains same for the  $\gamma$ -ray exposed sample but carbon

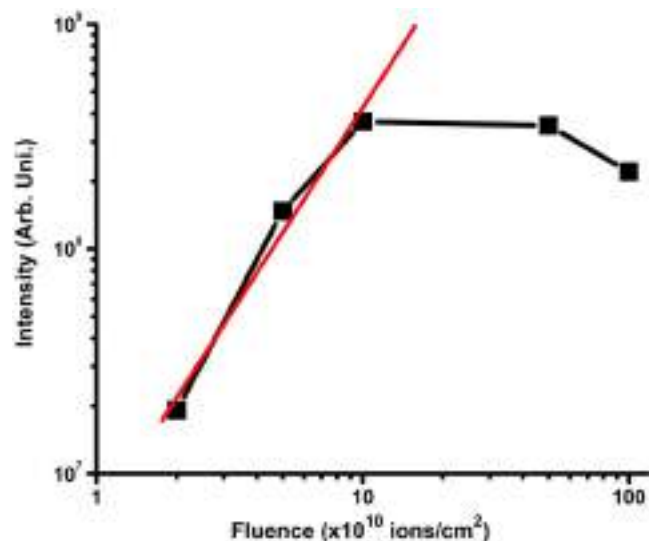


**FIGURE 16** Thermoluminescence response curve for  $C^{5+}$  ion beam-irradiated  $LiMgBO_3:Dy^{3+}$  samples

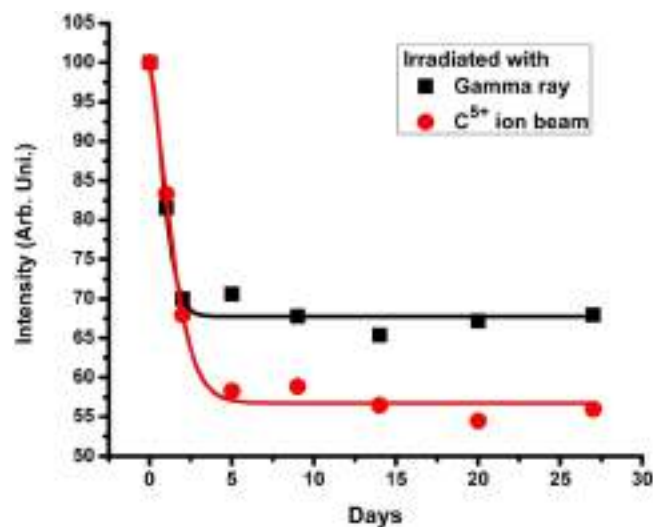


**FIGURE 17** Fading of synthesized  $LiMgBO_3:Dy^{3+}$  for  $\gamma$ -ray and  $C^{5+}$  beam exposure

beam-exposed samples faded to 42%, which was very high for a dosimeter.

The trapping parameters of  $LiMgBO_3:Dy$  irradiated with the 75 MeV  $C^{5+}$  ion beam were calculated. The TL glow curve for  $1 \times 10^{11}$  ions/cm<sup>2</sup> fluence of the carbon beam was deconvoluted to three peaks using the glow curve deconvolution method with FOM 1.61% and is shown in Figure 18. The trapping parameters for each peak for all fluencies were calculated and are shown in Table 4.

### 3.5 | Electron paramagnetic resonance (EPR)

EPR spectra were recorded at room temperature (RT) and liquid nitrogen temperature (LNT). Phosphors were irradiated with a  $\gamma$ -ray dose

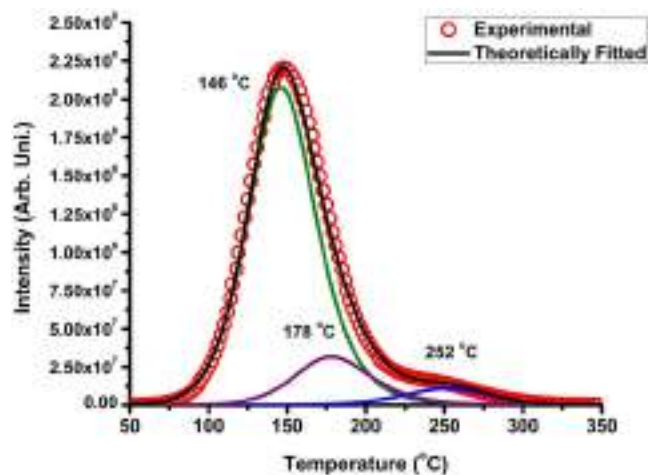


**FIGURE 18** Deconvolution of thermoluminescence glow curves for  $LiMgBO_3:Dy$  irradiated with a 75 MeV  $C^{5+}$  ion beam

**TABLE 4** Trapping parameters for  $LiMgBO_3:Dy$  irradiated with a 75 MeV  $C^{5+}$  ion beam using the glow curve deconvolution method

Fluence (ions/cm <sup>2</sup> )	Peak	T <sub>m</sub>	E	b
$2 \times 10^{10}$	P1	146	0.93	2
	P2	170	0.96	2
	P3	249	1.04	1.3
$5 \times 10^{10}$	P1	146	0.97	1.7
	P2	168	0.98	1.7
	P3	248	1.02	1
$1 \times 10^{11}$	P1	146	0.92	2
	P2	168	0.99	1.9
	P3	248	1.06	2
$5 \times 10^{11}$	P1	142	0.95	1.6
	P2	174	0.97	2
	P3	242	1.06	1
$1 \times 10^{12}$	P1	146	0.95	1.9
	P2	178	1.01	2
	P3	252	1.06	1.5

for EPR studies. EPR studies on  $Dy^{3+}$  ions in  $YAl_3(BO_3)_4$  and  $EuAl_3(BO_3)_4$  aluminoborates,  $LiNaSO_4$ ,  $CaMg_2(SO_4)_3:Dy^{3+}$  have been reported recently<sup>[39–41]</sup>. It was noted that EPR was observed only at liquid helium temperature, because the electronic configuration of  $Dy^{3+}$  ion is  $4f^9$  and its ground state, first excited state and second excited states are given by  ${}^6H_{15/2}$ ,  ${}^6H_{13/2}$  and  ${}^6H_{11/2}$ , respectively. Furthermore,  ${}^6H_{15/2}$  splits into eight,  ${}^6H_{13/2}$  into seven and  ${}^6H_{11/2}$  into six Kramer's doublets under very low crystal field symmetry<sup>[41]</sup>. The first excited multiplet  ${}^6H_{13/2}$  was located  $\approx 3.5 \times 10^3$  cm<sup>-1</sup> higher in energy. Due to mixing of the higher states and the large orbital angular momentum associated with these states, there was a very short spin lattice relaxation time for the  $Dy^{3+}$  ion and therefore EPR was observed<sup>[41]</sup>.

The non-irradiated  $LiMgBO_3:Dy$  sample did not show an EPR signal at RT. The EPR spectrum for  $\gamma$ -ray-irradiated  $LiMgBO_3:Dy$  is shown in Figure 19. The RT EPR spectrum consisted of a well resolved

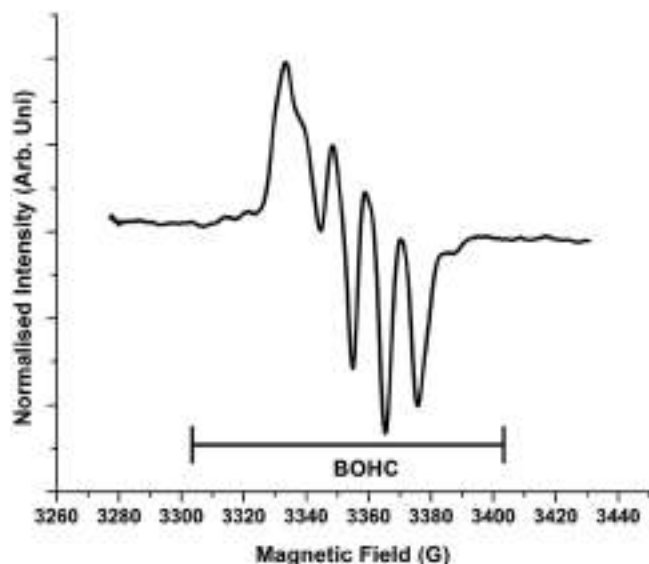


**FIGURE 19** Electron paramagnetic resonance spectrum of a polycrystalline sample of  $\gamma$ -ray-irradiated  $\text{LiMgBO}_3:\text{Dy}$

quartet structure (perpendicular components) with spacing of 10 G and having nearly equal intensity. Superimposed onto the lowest field component of this quartet structure, a broad parallel-like structure (parallel component) was observed, but without any hyperfine structure. The observed EPR spectrum was assumed to arise from single paramagnetic species having nearly axial symmetry ( $g_{\parallel} = 2.020$ ;  $g_{\perp} = 2.0064$ ,  $A_{\parallel} = 0$  G and  $A_{\perp} = 10.5$  G). The quartet hyperfine Bohr magnetron structure was due to the interaction of unpaired electrons in the radical with the most abundant isotope of boron,  $^{11}\text{B}$  ( $I = 3/2$ , natural abundance 80.2%). The hyperfine structure due to the  $^{10}\text{B}$  nucleus ( $I = 3$ ; isotopic abundance 19.80%) was unresolved due to overlapping of its hyperfine lines<sup>[42]</sup> and resulting in significant line-broadening to as much as 5 G. This finding is shown in Figure 19. The experimentally observed  $g_{\text{iso}} = 2.0111$  for this radical was close to the  $g_{\text{iso}}$  value (2.0111) reported in the literature. Based on observed

$g$  values, this signal was attributed to the boron–oxygen hole centre (BOHC) ( $g$  for  $e$  trapped centres is less than 2.00, whereas for hole-trapped species  $g$  is greater than 2.00). The EPR parameters for different types of BOHCs are given in Table 5. EPR parameters for free radicals were precisely determined from the calculated spectra, assuming axial symmetry of  $g$  and  $A$  tensors, which were obtained using the WIN-EPR BRUKER SIMFONIC program based on perturbation theory<sup>[43]</sup>. The theoretical EPR signals were calculated using spin Hamiltonian  $H_s = \beta eS \cdot g \cdot B + I \cdot A \cdot S$ , where  $\beta e$  is the electron magnetron;  $S$  and  $I$  are the electron spin and nuclear spin operators, respectively;  $g$  is the spectroscopic factor;  $B$  is the applied magnetic field; and  $A$  is the hyperfine terms for the  $^{11}\text{B}$  nucleus<sup>[44]</sup>. The possibilities for EPR spectrum generation could be:

(i) The quartet structure arising from the interaction of unpaired electrons with the  $^7\text{Li}$  nucleus ( $^7\text{Li}$ , having a natural abundance of 92.5%) as observed in  $[\text{Li}]^0$ , but the unpaired spin density resides on the  $S$  orbital for this centre, leading to a large hyperfine coupling constant and isotropic  $g = 2.0023$ .

Howard J. A. and Sutcliffe R. observed three types of  $[\text{Li}]^0$  centres with  $g$  values close to free electron  $g$  value 2.0023 and a large hyperfine coupling constant 135 G in the hydrocarbon matrix. In same system, authors observed evidence for stabilization of the lithium trimer,  $\text{Li}_3$  ( $A = 33.1$  G and  $g = 2.001$ )<sup>[45]</sup>. However, the small hyperfine coupling constant and  $g$  value observed in our case did not support this finding.

(ii) The unpaired spin density on oxygen interacted with  $^7\text{Li}$ . Even though there have been many papers on EPR studies on irradiated lithium-based glasses and inorganic matrices, no paramagnetic centre of this type has been reported.

EPR spectra at different temperatures in the range 300–450 K were recorded to identify the role of electron–hole recombination reactions in thermally stimulated luminescence (TSL) processes. Spectra are shown in Figure 20. It was observed that, in the temperature range 400–425 K, there was a drastic reduction in the intensity of the BOHC signal. Furthermore, the BOHC signal became thermally destroyed at 425 K by releasing the trapped hole. The recombination of this hole

**TABLE 5** Spin Hamiltonian ( $g$  and  $A$ ) parameters for boron–oxygen hole centres (BOHCs) in different minerals and inorganic matrices (the principal hyperfine coupling constant ( $a$  value) for  $^{11}\text{B}$  is given in gauss)

Matrix	Radical	$g_1$	$g_2$	$g_3$	$g_{\text{ava}}$	$A_1$	$A_2$	$A_3$	$A_{\text{iso}}$	Temp. (K)	Ref.
$\text{CaCO}_3$	$\text{BO}_3^{2-}$	2.0080	2.0127	2.0127	2.0111	12.6	8.4	8.4	9.8	4.2 K	1
$\text{CaBSiO}_4(\text{OH})$	$[\text{BO}_4]^0$	2.0059	2.0066	2.0512	2.0212	9.2	6.3	4.6	6.7	77 K	2
$\text{CaBSiO}_4(\text{OH})$	$[\text{BO}_4]^0$	2.0031	2.0118	2.0482	2.0210	9.85	9.06	4.01	7.64	10 K	3
$\text{CaB}_2(\text{SiO}_4)_2$	$[\text{BO}_4]^0$	2.0059	2.0066	2.0481	2.0202	9.6	9.4	4.9	7.97	77 K	2
$\text{ZrSiO}_4$	$[\text{BO}_4]^0$	2.0039	2.0013	2.0474	2.0175	4.88	5.19	1.90	3.99	15 K	4
$\text{K}_2\text{B}_2\text{O}_4$	$\text{BO}_3^{2-}$	2.0091	2.0143	2.0128	2.0121	12.37	7.54	7.54	9.15	300 K	5
$\text{SrB}_4\text{O}_7$	$\text{BO}_3^{2-}$	1.9950	2.0130	2.0130	2.0070	13.26	9.46	9.46	10.73	300 K	6
$\text{BaBPO}_5$	BOHC	1.9907	2.0133	2.0419	2.0153	8.0	9.0	8.25	8.42	300 K	7
$\text{SrBPO}_5$	BOHC	1.9908	2.0133	2.0416	2.0152	9.0	9.0	8.5	8.83	300 K	8
$\text{LiMgBO}_3$	BOHC	2.0064	2.0064	2.0200	2.0110	–	10.50	10.50	7.0	300 K	Present work <sup>a</sup>

<sup>a</sup> $\text{CaCO}_3$ ,  $\text{CaBSiO}_4(\text{OH})$ ,  $\text{CaB}_2(\text{SiO}_4)_2$  and  $\text{ZrSiO}_4$  represents calcite, detolite, danburite and zircon minerals respectively; errors in estimation of  $g$  and  $A$  values are  $\pm 0.0001$  and  $\pm 0.05$  Gauss respectively.

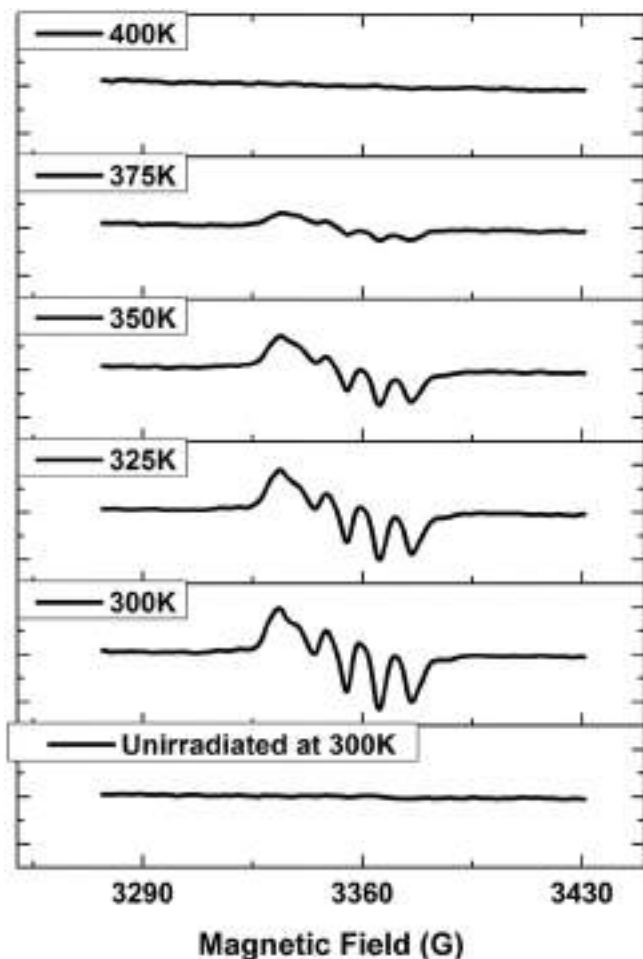


**FIGURE 20** Electron paramagnetic resonance spectra of LiMgBO<sub>3</sub>:Dy recorded at different temperatures in the range 300–450 K

with electrons resulted in the production of an excited state of Dy<sup>3+</sup>. De-excitation of Dy<sup>3+</sup> gave its characteristic emission before reaching the ground state, resulting in a glow peak at around 160°C.

## 4 | CONCLUSIONS

A LiMgBO<sub>3</sub>:Dy<sup>3+</sup> phosphor was prepared using the solution combustion method and different techniques were used to study its luminescence properties. The XRD pattern was found to be consistent with standard patterns and depicted that the pattern belonged to the pure monoclinic phase with space group C2/c. SEM micrographs clearly indicated agglomeration with rod shapes distributed widely. FTIR spectrum showed bands at 1458 cm<sup>-1</sup> and 1287 cm<sup>-1</sup>, corresponding to asymmetrical stretching relaxations of the B–O bond of the trigonal BO<sub>3</sub> unit. PL emission spectra for LiMgBO<sub>3</sub>:Dy<sup>3+</sup> consisted of two peaks centred at 478 and 572 nm due to the <sup>4</sup>F<sub>9/2</sub>→<sup>6</sup>H<sub>15/2</sub> magnetic dipole transition and the hypersensitive <sup>4</sup>F<sub>9/2</sub>→<sup>6</sup>H<sub>13/2</sub> electric dipole transitions of Dy<sup>3+</sup> respectively. Moreover the γ-irradiated LiMgBO<sub>3</sub>:Dy<sup>3+</sup> sample showed TL linearity in the dose range 10 Gy to 1 kGy and the C<sup>5+</sup>-irradiated samples showed TL linearity in the fluence range 2 × 10<sup>10</sup> to 1 × 10<sup>11</sup> ions/cm<sup>2</sup>. In the present study, different

methods were used to calculate and compare trapping parameters to understand the mechanism of the TL glow curve in detail. Finally, EPR spectra were recorded at different temperatures to study the role of electron–hole recombinations in the TL process.

## ACKNOWLEDGEMENTS

One of the authors, Mangesh M. Yerpude, is thankful to University Grants Commission-India for providing financial assistance to carry out this work under the UGC-NET-JRF scheme (file no. F.17-86/2008 (SA-I)). The authors also would like to thank the Director of the IUAC for providing financial assistance and the ion beam facility for carrying out this work under the IUAC projects. Authors are also thankful to Birendra Singh for support during measurements at IUAC.

## ORCID

Vibha Chopra  <https://orcid.org/0000-0003-2849-4332>

S.J. Dhoble  <https://orcid.org/0000-0002-4249-8228>

## REFERENCES

- [1] V. Chopra, L. Singh, S. P. Lochab, V. E. Aleynikov, A. S. Oinam, *Radiat. Phys. Chem.* **2014**, *102*, 5.
- [2] V. Chopra, L. Singh, S. P. Lochab, *Nucl. Instrum. Meth. Phys. Res. Section A* **2013**, *717*, 63.
- [3] N. Salah, S. Habib, S. S. Babkair, S. P. Lochab, V. Chopra, *Radiat. Phys. Chem.* **2013**, *86*, 52.
- [4] L. Singh, V. Chopra, S. P. Lochab, *JOL* **2011**, *131*, 1177.
- [5] R. Norrestam, *Zeitschrift für Kristallographie* **1989**, *187*, 103.
- [6] S. R. Anishia, M. T. Jose, O. Annalakshmi, V. Ramasamy, *JOL* **2011**, *131*, 2492.
- [7] Y. Saleh, M. Alajerami, S. Hashim, W. M. Saridan, W. Hassan, A. T. Ramli, A. Kasim, *Phys. B* **2012**, *407*, 2398.
- [8] Z. Liang, F. Mo, X. Zhang, L. Zhou, *JOL* **2014**, *151*, 47.
- [9] N. S. Bajaj, S. K. Omanwar, *Optik-Int. J. Light Elec. Optics* **2014**, *125*, 4077.
- [10] A. K. Bedyal, V. Kumar, R. Prakasha, O. M. Ntwaeaborwab, H. C. Swart, *Appl. Surf. Sci.* **2015**, *329*, 40.
- [11] W. Wesch, A. Kamarou, E. Wendler, *Nucl. Instrum. Methods B.* **2004**, *225*, 111.
- [12] M. M. Yerpude, N. S. Dhoble, S. P. Lochab, S. J. Dhoble, *Luminescence* **2016**, *31*, 1115.
- [13] G. Kraft, *Prog Part Nucl Phys.* **2000**, *45*, S473.
- [14] H. Suit, T. De Laney, S. Goldberg, H. Paganetti, B. Clasio, L. Gerweck, *Radiother. Oncol.* **2010**, *95*, 3.
- [15] M. Scholz, *Nucl Instrum Methods B* **2000**, *161*, 76.
- [16] D. Schulz-Ertner, O. Jäkel, W. Schlegel, *Semin. Radiat. Oncol.* **2006**, *16*, 249.
- [17] D. Kanjilal, S. Chopra, M. M. Narayanan, I. S. Iyer, J. J. R. vandana, S. K. Datta, *Nucl. Instrum. Methods Phys. Res. A* **1993**, *328*, 97.
- [18] N. S. Bajaj, S. K. Omanwar, *Opt. Mater.* **2013**, *35*, 1222.
- [19] A. H. Oza, N. S. Dhoble, S. P. Lochab, S. J. Dhoble, *Luminescence* **2015**, *30*, 967.
- [20] Y. S. Xin, C. Z. Jun, G. L. Xin, W. L. Liang, *Ceram. Int.* **2012**, *38*, 1065.

- [21] A. J. Dekker, *Solid State Physics*, Prentice-Hall Inc., Englewood Cliffs, New Jersey **1957**.
- [22] R. Bharthasaradhi, L. C. Nehru, V. Chopra, S. J. Dhoble, *J. Mater. Sci. Mater. Electron.* **2018**, *29*, 11229. <https://doi.org/10.1007/s10854-018-9209-7>
- [23] A. N. Yazici, *Nucl. Instrum. Methods Phys. Res., Sect. B* **2004**, *215*, 174.
- [24] W. Hoogenstraaten, *Philips Res. Rep.* **1958**, *13*, 515.
- [25] G. Kitis, S. Charalamboust, J. W. N. Tuyn, *J. Phys. D Appl. Phys.* **1993**, *26*, 2036.
- [26] B. P. Kore, N. S. Dhoble, S. J. Dhoble, *Radiat. Meas.* **2014**, *67*, 35.
- [27] S. G. Gorbics, A. E. Nash, F. H. Attix, *Int. J. Appl. Radiat. Isot.* **1969**, *20*, 829.
- [28] S. Mahajna, Y. S. Horowitz, *J. Phys. D Appl. Phys.* **1997**, *30*, 2603.
- [29] Y. S. Horowitz, O. Avila, M. Rodrigues, *Nucl. Instrum. Methods Phys. Res., Sect. B* **2001**, *184*, 85.
- [30] V. Pagonis, G. Kitis, C. Furetta, *Numerical and Practical Exercises in Thermo-luminescence*, Springer, Berlin **2006**.
- [31] G. F. J. Garlick, A. F. Gibson, *Proc. Phys. Soc.* **1948**, *60*, 574.
- [32] R. Chen, *J. Electrochem. Soc.* **1969**, *116*, 1254.
- [33] J. M. Kalita, M. L. Chithambo, *JOL* **2017**, *185*, 72.
- [34] R. Chen, S. A. A. Winer, *J. Appl. Phys.* **1970**, *41*, 5227.
- [35] C. M. Sunta, W. E. Feria Ayta, T. M. Piters, S. Watanabe, *Radiat. Meas.* **1999**, *30*, 197.
- [36] G. Kitis, R. J. M. Gomez, J. W. N. Tuyn, *J. Phys. D Appl. Phys.* **1998**, *31*, 2636.
- [37] M. Bhake, G. B. Nair, G. D. Zade, S. J. Dhoble, *Luminescence* **2016**, *31*, 1468.
- [38] J. A. Wani, N. S. Dhoble, S. P. Lochab, S. J. Dhoble, *Nucl. Instrum. Methods Phys. Res., Sect. B* **2015**, *349*, 56.
- [39] A. A. Prokhorov, E. E. Zubov, L. F. Chernysh, H. Szymczak, A. D. Prokhorov, *Low Temp. Phys.* **2014**, *40*, 939.
- [40] R. T. Weber, *WIN-EPR Simfonia Manual Ver1.2*, Bruker Instruments, Inc., Billerica, MA **1995** and references therein.
- [41] S. Tamboli, R. M. Kadam, B. Rajeswari, B. Singh, S. J. Dhoble, *JOL* **2018**, *203*, 267.
- [42] R. M. Kadam, T. K. Seshagiri, V. Natarajan, S. V. Godbole, *Nucl. Instrum. Methods Phys. Res., Sect. B* **2008**, *266*, 5137.
- [43] K. K. Gupta, R. M. Kadam, N. S. Dhoble, S. P. Lochab, S. J. Dhoble, *Chem. Phys. Lett.* **2018**, *20*, 1540.
- [44] M. Kumar, T. K. Seshagiri, R. M. Kadam, S. V. Godbole, *Mater. Res. Bull.* **2011**, *462*, 1359.
- [45] J. A. Howard, R. Sutcliffe, B. Mile, *Chem. Phys. Lett.* **1984**, *112*, 84.

**How to cite this article:** Yerpude MM, Chopra V, Dhoble NS, Kadam RM, Krupski AR, Dhoble SJ. Luminescence study of LiMgBO<sub>3</sub>:Dy for  $\gamma$ -ray and carbon ion beam exposure. *Luminescence*. 2019;1-12. <https://doi.org/10.1002/bio.3694>